# Theoretical Investigations of thermoelectric properties in nanostructured materials

Dissertation

zur Erlangung des Doktorgrades
der Naturwissenschaften
(Dr. rer. nat.)

vorgelegt von

Dipl.-Phys. Michael Bachmann

anno 2012


I. Physikalisches Institut
Justus-Liebig-Universität Giessen

Für meine Eltern

# Contents

# 1 Introduction

> "Die Energie kann als Ursache für alle Veränderungen in der Welt angesehen werden." [1]

In the year 2009 the world supply of primary energy was 509EJ (≙12150 million tons of oil equivalent (Mtoe)) [2]. The total consumption of final energy for this year was 350EJ (≙8353 Mtoe). The difference between theses numbers is due to the losses that occur during the transformation from primary energy to final energy, whereas the most losses originate in the production of electricity. The final energy consists of 17.3% electricity 79.4% fossile fuel and 3.3% of other forms. A huge part of the final energy is used in transportation. 90EJ are consumed in this sector. Even though electric mobility is a big issue these days, still 99% of the final energy used in transportation are fossil fuels. Since the requirements with respect to weight, costs, and dimensions are rather high for engines used in transportation, the efficiency of those engines is limited and therefore far away from the thermodynamic Carnot limit. In conclusion these numbers show that a huge amount of waste heat is produced. One big part arises in the conversion from primary energy to final energy and another big part arises when final energy is not used efficiently. Since there is such a large amount of waste heat, it would be worth to convert this waste heat into final energy again, even if only a small fraction could be converted. Devices which can be considered for these conversions need to fulfill specific demands. The most important demands are that the device itself should be economical and ecological. Also the devices should be scalable, maintenance free, and reliable. One class of devices that fulfill most of these demands are thermoelectric generators (TEG). In a TEG the Seebeck effect is utilized to generate electric power out of a temperature difference. The Seebeck effect was first discovered by Thomas Johann Seebeck in 1821. Seebeck showed that a temperature difference leads to a so called Seebeck voltage. The Seebeck voltage $V_S$ is proportional to the temperature difference $\Delta T$ and the Seebeck coefficient is defined as $S = \frac{V_S}{\Delta T}$. The main principle of a TEG is demonstrated in Fig. 1.1.

The first applications of TEGs arise in the 1920's, where TEGs are used for electricity generation in kerosene lamps [3]. In the 1960's TEGs become important for spacecraft applications, since they are an important component of a radioisotope thermoelectric generators(RTG). In a RTG a TEG transforms heat that is obtained from radioactive decay in electricity. During these spacecraft applications TEGs demonstrated their reliability, where TEGs operated failure free and maintenance free for over 30 years [4]. Today TEGs are employed in various fields. Besides in spacecraft applications, TEGs are used in automobiles [5], wood stoves [6], wireless remote applications [7] and Peltier coolers. In automobiles waste heat from the engine or from the exhaust is used to unload the alternator, which safes fuel. In wood stoves TEGs are used to run a fan, which regulates the air supply and therefore increases the

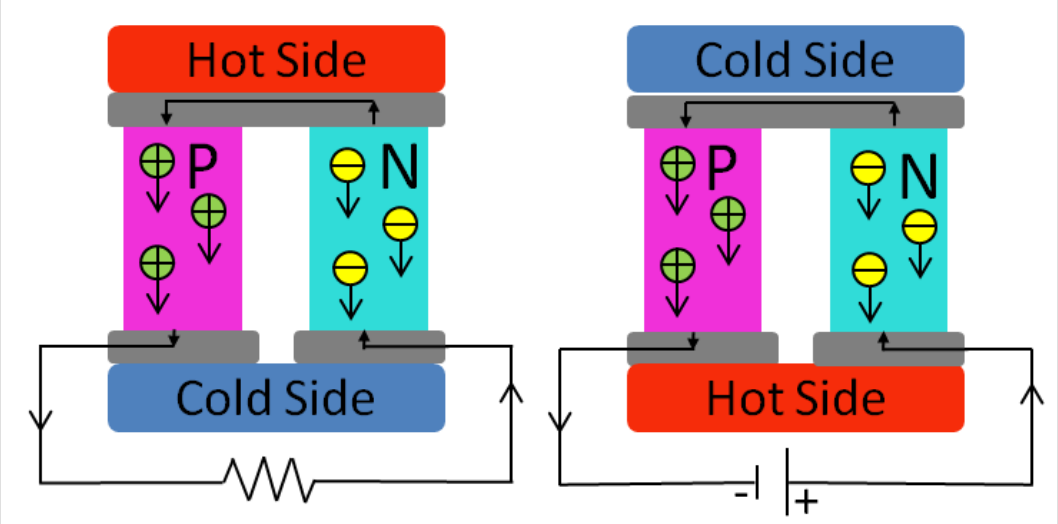


Figure 1.1: Schematic sketch of a TEG. In general a TEG consists of two different leg types n-type and p-type. The n-type leg has as negative Seebeck coefficient the p-type leg a positive Seebeck coefficient. The legs are thermally connected parallel and electrically connect in series. There are in principle two different modes in which a TEG can be used. A TEG can be used as a generator (left). In this case a temperature gradient leads to a current in the n-leg of electrons from the hot to the cold side and simultaneously in the p-leg a current of holes from the hot to the cold side. These currents lead to a voltage difference between both cold or hot ends of the different legs. This voltage can be used to perform work. Another mode of a TEG is shown right. In this case an external voltage is applied, which leads to a current in the n-leg of hot electrons from one side to another. Therefore, one side is heated and the other one is cooled. In the p-leg cold holes are traveling from one side to the other and increase this effect.

efficiency and reduced the emission of carbon monoxide. It is also possible to generate electricity from the heat of the stove. TEGs can be also very useful as a power supply for remote applications like sensors to avoid an additional wire or regular maintenance. If a voltage is imposed on a TEG the TEG can also function as a heat pump. The effect that is utilized in this case is called Peltier effect. The Peltier effect is in principle the reversed Seebeck effect, where a charge current creates a temperature gradient. A TEG that operates as a heat pump is also called Peltier element or Peltier cooler, since they are often used for cooling application like portable refrigerators. The main principle of a TEG, operated as a Peltier element, is demonstrated in Fig. 1.1. Despite the versatile applicability of the TEGs, a mass market for TEGs has not yet been established. The main reason for this is the rather low efficiency of TEGs. The ideal maximum achievable efficiency of a TEG is linked to the material parameters by the so called figure of merit zT [8]

$$zT = \frac{\sigma S^2 T}{\kappa}. \tag{1.1}$$

$\sigma$ : electric conductivity
$S$ : Seebeck coefficient
$\kappa$ : thermal conductivity
$T$ : Temperature

In this equation one can identify the most important characteristics of a good thermoelectric material. Besides a high Seebeck coefficient the material must be a good electron conductor and simultaneously a bad heat conductor. There is in principle heat conduction due to electrons and due to phonons. Hence the thermal conductivity can be divided into two parts $\kappa_e$ and $\kappa_p$. $\kappa_e$ is the electric contribution to thermal conductivity and $\kappa_p$ the phonon part of the thermal conductivity. $\kappa_p$ is sometimes also referred to as the lattice part of the thermal conductivity since phonons are the excitations of the lattice vibrations. Since electrons carry charge and heat it is difficult to alter $\kappa_e$ and $\sigma$ independently. A rough estimation of the relation between $\kappa_e$ and $\sigma$ is given by the Wiedeman-Franz-law [9], which states that $\kappa_e$ is proportional to $\sigma$. The Wiedeman-Franz-law holds for highly doped semiconductors and metals. The basic demands on a thermoelectric material can be summarized by "a good thermoelectric is a crystal for electrons and a glass for phonons".

The figure of merit zT is linked to the total efficiency by [8]

$$\eta = 100 \cdot \frac{T_h - T_c}{T_h} \cdot \frac{\sqrt{1+zT}-1}{\sqrt{1+zT}+\frac{T_c}{T_h}}. \tag{1.2}$$

$T_c$ and $T_h$ are the temperatures of the cold and hot side, respectively. In Fig.1.2 the total efficiency $\eta$ is shown for different zT and temperatures. For zT$\rightarrow \infty$ the efficiency equals the Carnot limit.

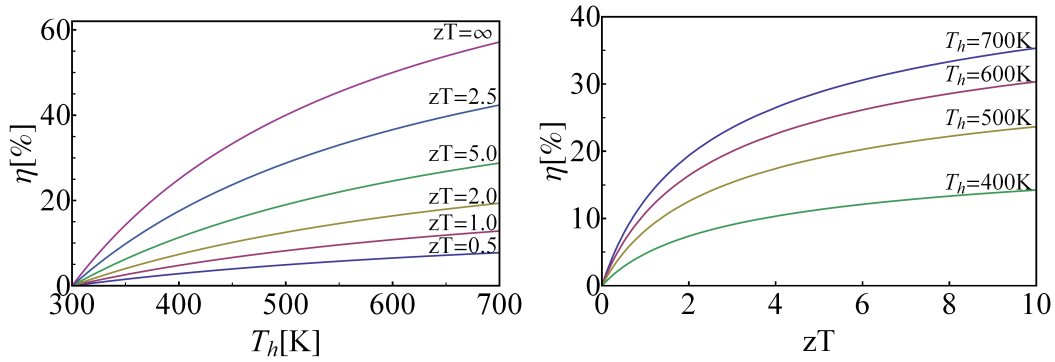


Figure 1.2: Left: Total efficiency for different values of zT against $T_h$ for $T_c = 300K$. Right: Total efficiency for different $T_h$ against zT for $T_c = 300K$.

Today there are several materials that are used for thermoelectric applications. Each material has a certain temperature at which the material exhibits a high figure of merit. Typically good thermoelectric materials are highly doped semiconductors, since metals exhibit a too small Seebeck coefficient. Fig.1.3 shows the figure of merit against the temperature for the most common thermoelectric materials. The actual efficiency of the overall TEG is in general lower because of losses at the contacts and the broad temperature range in the TEG. The best TEGS today can achieve a zT value of approximately 0.7 [10]. To be competitive with established technologies like steam engines or thermal solar engines zT has to be at least 4 [10]. Nevertheless, if a power output lower than 70W is required the established engines become quite insufficient because of their poor scaling behavior. In this case a TEG could be favorable even with a zT value of 0.7.

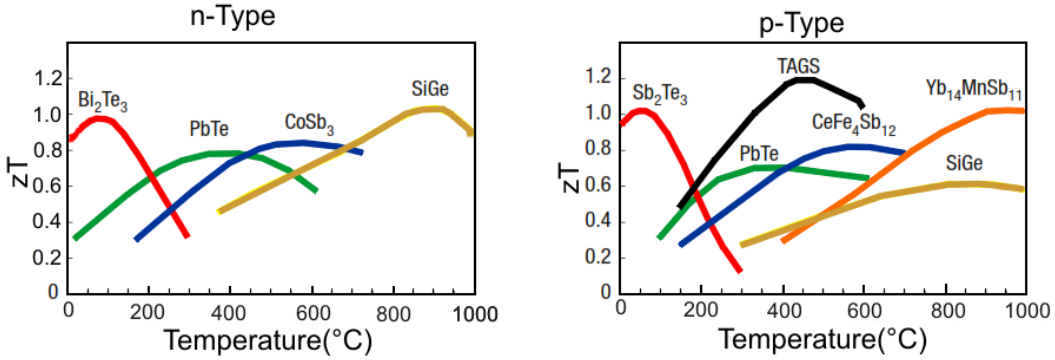


Figure 1.3: Left: Figure of merit zT for typical n-type (Left) and p-type (Right) thermoelectric materials [8].

Despite 50 years of research the materials shown in Fig.1.3 are the best thermoelectric material found so far and they fairly achieve a figure of merit of 1. In the early 1990's a new concept to increase efficiency arises in the

literature. Instead of searching for new materials the strategy is to improve the efficiency of known good thermoelectric materials due to nanostructuring. There are in principle two promising effects that are expected to rise due to nanostructuring. One effect that occurs is additional phonon scattering, which reduced the thermal conductivity. Venkatasubramanian demonstrated this effect in $Sb_2Te_3/Bi_2Te_3$ multilayers [11]. The other effect is an enhancement of the Seebeck coefficient. An enhancement of the Seebeck coefficient can be achieved by structures that lead to energy filtering [12, 13, 14, 15, 16] or by structures of low dimensions [17, 18].

A field that is neglected in thermoelectric is the research of so called Green thermoelectrics. The best thermoelectric material today are either toxic and pollute the environment (PbTe, $Bi_2Te_3$) or they are expensive and rare (SiGe) [19]. In contrast Green thermoelectrics are materials that are environmentally friendly and available in masses. One promising candidate for such a Green thermoelectric is nanostructured ZnO. ZnO has been in the focus of research for several years, since it is also a promising candidate for optoelectronic devices due to the large band gap of 3.4eV [20]. Bulk ZnO is not a good thermoelectric material because of the rather high thermal lattice conductivity of about $60\mathrm{Wm}^{-1}K^{-1}$ [21]. A decrease in the lattice conductivity compared to the bulk value is expected for polycrystalline ZnO because of the additional scattering mechanism at the grain boundaries. Also additional energy filtering effects can occur at the grain boundary. A rather high zT value of 0.65 at 1247K is reported by Ohtaki et al. [22]. In conjunction with ZnS the efficiency of ZnO could also be enhanced. The idea in ZnO/ZnS based systems is, that a high phonon scattering occurs because of the different masses of oxygen and sulfur. On the other hand the electric system should not be effected that much since oxygen and sulfur belong to the same main group in the periodic table. Some fundamental research on this field was done by Homm et al. [23, 24, 25], where they investigated the effect of ZnO/ZnS superlattices on the Seebeck coefficient, as well as the dependency of the doping concentration on the Seebeck coefficient in aluminum doped ZnO. Despite the great progress of research in this material the main principle mechanism of transport across ZnO/ZnO and ZnO/ZnS are not fully understood. Therefore in this work the main focus will be the investigation of the impact on the thermoelectric parameters of such interfaces.

# 2 Theory

In this chapter the fundamentals of thermoelectrics are derived. In the first section of this chapter the Onsager-de Groot-Callen model is briefly discussed and the well known Onsager expressions are derived. Also the connection between the kinetic coefficients and the thermoelectric coefficients are shown. From the Onsager expressions the classical laws of Ohm and Fourier are derived. At the end of the first section the connection between the three thermoelectric effects which are the Seebeck, Peltier and Thomson-effect are discussed. In the second section of this chapter two microscopic transport models are presented, which can be related to the kinetic coefficients. A frequently used model is the Boltzman transport equation (BTE)[26]. The central quantity in the BTE is the relaxation time. The BTE is often used to describe diffusive transport. The other model presented in this work is the Landauer formalism [27, 28]. The Landauer formalism is preferentially used to describe coherent transport. In the third section of the chapter the basics of solid state physics with focus on the electronic structure and the lattice vibrations are presented. Also in this section techniques are introduced to calculate such structures. These techniques are the density functional theory (DFT) [29] and the Green's function formalism. An extension of the Green's function formalism to non equilibrium Green's function formalism (NEGF) is shown [27, 28]. The NEGF is suitable in connection with the Landauer formalism to calculate electron and phonon transport[30, 31, 32]. In the fourth section a model to describe grain boundary transport is introduced. In this model the effect of grain boundaries on the transport are taken into account due to double Schottky barriers.

## 2.1 The Onsager equations

In this chapter a brief introduction of the Onsager-de Groot-Callen Model is given. A more comprehensive and detailed description can be found in reference [33].

The conservation of energy and matter as well as the first law of thermodynamics lead to the following expression for the total energy flux $J_E$ per unit area

$$J_E = J_Q + \mu J_N. \tag{2.3}$$

$J_Q$ is the heat flux per unit area and $J_N$ is the particle flux per unit area. For each of these fluxes a force can be defined that causes these fluxes. In analogy to classical mechanics a potential for each of these fluxes can be defined. The corresponding potentials for the energy flux $J_E$ and for the particle flux $J_N$ are $\frac{1}{T}$ and $-\frac{\mu}{T}$ [33]. This leads to the kinetic coefficient matrix

$$\begin{bmatrix} J_N \\ J_E \end{bmatrix} = \begin{bmatrix} L_{NN} & L_{NE} \\ L_{EN} & L_{EE} \end{bmatrix} \begin{bmatrix} -\nabla\frac{\mu}{T} \\ \nabla\frac{1}{T} \end{bmatrix}. \tag{2.4}$$

In a steady state non-equilibrium process the principle of minimal entropy conditions holds. This principle requires that the matrix in equation (2.4) is symmetric which means $L_{NE}$=$L_{EN}$. From a microscopic point of view this means that the underlying processes have time reversal symmetry. In thermoelectrics the heat and charge currents $J_Q$ and $J_C$ are the conventional quantities. The charge and particle current are linked by $J_C = eJ_N$, whereas the link between the heat current $J_Q$, particle current $J_N$ and $J_E$ is given in equation (2.3). Using $\nabla\frac{1}{T} = -\frac{1}{T^2}\nabla T$ equation (2.4) can be rewritten as

$$\begin{bmatrix} J_C \\ J_Q \end{bmatrix} = \begin{bmatrix} L_{11} & L_{12} \\ L_{21} & L_{22} \end{bmatrix} \begin{bmatrix} -\nabla\frac{\mu}{e} \\ -\nabla T \end{bmatrix} \tag{2.5}$$

with

$$L_{11} = \frac{e^2}{T} L_{NN} \tag{2.6a}$$

$$L_{12} = \frac{e}{T^2}(L_{NE} - \mu L_{NN}) \tag{2.6b}$$

$$L_{21} = \frac{e}{T}(L_{NE} - \mu L_{NN}) \tag{2.6c}$$

$$L_{22} = \frac{1}{T^2}(L_{EE} + \mu^2 L_{NN} - \mu L_{NE} - \mu L_{EN}). \tag{2.6d}$$

In equation (2.5) the fluxes are not written as a function of their corresponding thermodynamic potentials $\frac{1}{T}$ and $\frac{-\mu}{T}$. Therefore, the coefficient matrix in (2.5) does not have to be symmetric. In fact the off diagonal elements are linked by $L_{12}T = L_{21}$. From equation (2.5) the connection between the $L_{nm}$ and the

thermodynamic quantities $\sigma$, S and $\kappa$ can be extracted. The electric field $E$ and the chemical potential $\mu$ are linked by $-\frac{\nabla\mu}{e} = E$. For $\nabla T = 0$ equation (2.5) yields

$$J_C = L_{11}E \tag{2.7a}$$
$$J_Q = L_{21}E. \tag{2.7b}$$

Equation (2.7a) is Ohm's law with $L_{11} = \sigma$. Equation (2.7a) and (2.7b) can be combined to get

$$J_Q = \frac{L_{21}}{L_{11}}J_C. \tag{2.8}$$

This equation describes the Peltier effect with $\frac{L_{21}}{L_{11}} = \Pi$, where $\Pi$ is the Peltier coefficient. For $J_C = 0$ equation (2.5) becomes

$$0 = L_{11}E + L_{12}(-\nabla T) \tag{2.9a}$$
$$J_Q = \left(L_{22} - \frac{L_{12}L_{21}}{L_{11}}\right)(-\nabla T). \tag{2.9b}$$

The Seebeck coefficient is defined as $\frac{E}{\nabla T} = \frac{L_{12}}{L_{11}}$. Equation (2.9b) shows Fourier's law with $\kappa = L_{22} - \frac{L_{12}L_{21}}{L_{11}}$. The relations between the $L_{nm}$ and the thermoelectric coefficients are summarized in the following:

$$\sigma = L_{11}, \tag{2.10a}$$
$$S = \frac{L_{12}}{L_{11}}, \tag{2.10b}$$
$$\Pi = \frac{L_{21}}{L_{11}}, \tag{2.10c}$$
$$\kappa = L_{22} - \frac{L_{12}L_{21}}{L_{11}}, \tag{2.10d}$$
$$\kappa_0 = L_{22}. \tag{2.10e}$$

Thereby, the convention is used to rename $L_{22}$ to $\kappa_0$. Using these relations equation (2.5) becomes

$$\begin{bmatrix} J_C \\ J_Q \end{bmatrix} = \begin{bmatrix} \sigma & \sigma S \\ \sigma\Pi & \kappa_0 \end{bmatrix} \begin{bmatrix} E \\ -\nabla T \end{bmatrix}. \tag{2.11}$$

Since $L_{12}T = L_{21}$, there is a direct relation between the Seebeck coefficient and the Peltier coefficient

$$S \cdot T = \Pi, \tag{2.12}$$

which is known as the Kelvin relation. An interpretation of these effects can be obtained by looking at equation (2.12) and (2.8). Obviously, the Peltier coefficient is the average heat per charge carrier, whereas the Seebeck coefficient is the average entropy per charge, since entropy is heat divided by temperature.

In equation (2.11) only the different currents are defined, but no statement is made about the sources and sinks of these currents. For the charge current the law of charge conservation holds, which means $\nabla J_C = 0$. For the heat current the law of energy conservation together with equation (2.3) yields

$$\nabla J_E = 0, \tag{2.13a}$$
$$\nabla J_Q = E J_C, \tag{2.13b}$$
$$\nabla J_Q = \frac{J_C^2}{\sigma} + J_C S \nabla T. \tag{2.13c}$$

Besides the Seebeck effect and the Peltier effect the Thomson effect is the third thermoelectric effect. The Thomson effect describes the heat produced in a homogeneous conductor which has a current density $J_C$. The heat production per volume $q$ is the heat emitted to the surroundings. In this case the energy conservation yields

$$q = E J_C - \nabla J_Q. \tag{2.14}$$

Using equation (2.11) $q$ can be rewritten to

$$q = E J_C - \nabla J_Q, \tag{2.15a}$$
$$= E J_C - \nabla(\sigma \Pi E - \kappa_0 \nabla T), \tag{2.15b}$$
$$= \frac{J_C^2}{\sigma} + J_C S \nabla T - \nabla(J_C \Pi) + \nabla((\kappa_0 - \sigma \Pi S)\nabla T). \tag{2.15c}$$

From the relations in (2.10) the equation $\kappa_0 - \sigma S \Pi = \kappa$ can be directly derived. Therefore equation (2.15c) becomes

$$q = \frac{J_C^2}{\sigma} + J_C S \nabla T - \nabla(J_C \Pi) + \nabla(\kappa \nabla T). \tag{2.16}$$

For a homogeneous material the spatial dependency of S is only due to the temperature dependency of S. Hence equation 2.16 yields

$$q = \frac{J_C^2}{\sigma} - J_C T \frac{dS}{dT} \nabla T + \nabla(\kappa \nabla T). \tag{2.17}$$

Further, equation (2.17) can then be rewritten to

$$q = \frac{J_C^2}{\sigma} - J_C \mu_T \nabla T + \nabla(\kappa \nabla T). \tag{2.18}$$

with

$$\mu_T = T\frac{dS}{dT}. \tag{2.19}$$

$\mu_T$ is called the Thomson coefficient. Neglecting the term with higher order derivatives equation (2.19) yields

$$q = \frac{J_C^2}{\sigma} - J_C\mu_T\nabla T. \tag{2.20}$$

The first term in equation (2.20) is the Joule heating, which is always positive. The second term is the Thomson heating. The Thomson heating can be positive or negative and describes the reversibly released heat.

Equations (2.11) together with equations (2.13) build the basic relations for classical thermoelectric transport. To illustrate the connection between these equations and applications, $Bi_2Te_3$ as a typical thermoelectric material is considered. P-type $Bi_2Te_3$ has the following thermoelectric parameters [34]: $\sigma = 6.5 \cdot 10^4\Omega^{-1}m^{-1}$, $S = 210\mu V/K$, and $\kappa = 1.35W/mK$. For simplification the n-type values are chosen to be the same as the p-type values except for the Seebeck coefficient which is chosen to be $S = -210\mu V/K$. The length of the legs is chosen to be $L = 0.5cm$ and the temperature of one side is fixed to $300K$. In Fig.2.4 the considered system and the spatial distribution of the Seebeck coefficient is shown. The spatial distribution is chosen such, that the Seebeck coefficient smoothly changes between the bulk value and zero. The Seebeck coefficient is zero at the point, where the N-leg and P-leg are connected by a metallic contact. In the following considerations the sign convention is defined in Fig.2.4. In Fig.2.5 the $J_C - U$ characteristics for different $T2$ can be seen. $U$ is the voltage between the leg and $J_C$ is the current density. For $T2 = 300K$ the $J_C - U$ characteristics are in principle the one of a normal resistor that follows Ohm's law. If $T2 \neq 300K$ the TEG can be used as a generator. For $T2 > 300K$ the TEG produced power if $J_C < 0$ and $U > 0$. For $T2 < 300K$ the TEG produced power if $J_C > 0$ and $U < 0$. The absolute maximum voltage that can be achieved is given by $\Delta T \cdot 2 \cdot 210\mu V/K$. The TEG has the maximum power output at the point where the value $U \cdot J_C$ has its maximum. If $U$ and $J_C$ have the same sign the TEG is used as a heat pump. For $J_C > 0$ heat is pumped to increase the temperature $T2$, if $J_C < 0$ $T2$ is decreased. In Fig.2.5 the spatial temperature distribution for different $J_C$ is shown. Decreasing $J_C$ leads to a decreasing temperature at $x = 0.5cm$ till $J_C = -0.6A/mm^2$. Decreasing $J_C$ furthermore increases the temperature at $x = 0.5cm$. The reason for this behavior is, that the heat transport of the current is proportional to $J_C$, but the heat produced due to the joule term is proportional to the square of $J_C$. Therefore, an optimum value for $J_C$ exists at which the temperature at $x = 0.5cm$ has its minimum. This value for the current is in general not the value for the current at which the cooling is most efficient.

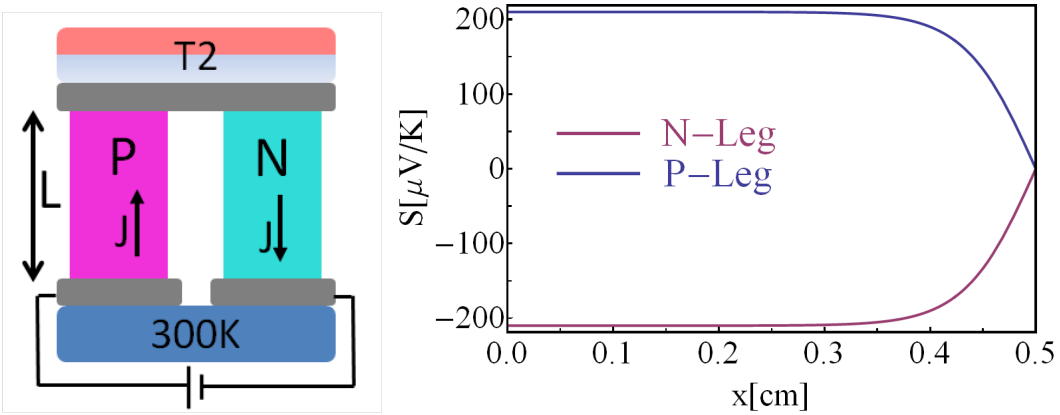


Figure 2.4: Left: Sketch of a TEG with N- and P- leg. Right: Spatial distribution of the Seebeck coefficient.

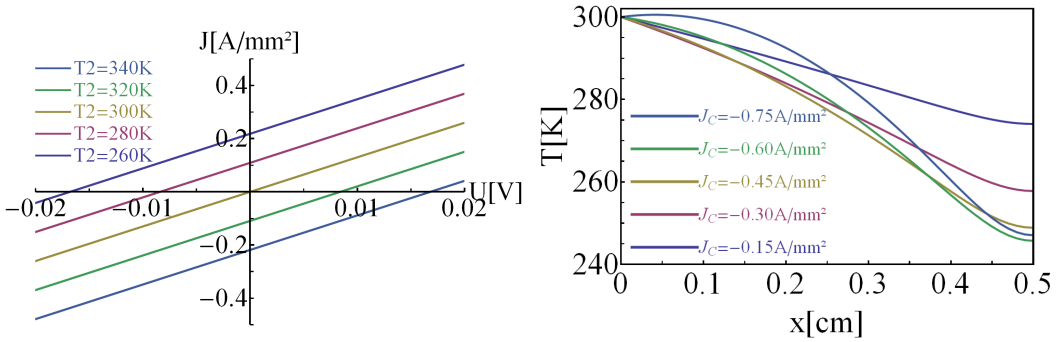


Figure 2.5: Left: $J_C - U$ characteristics for different values of $T2$. Right: Temperature profile for different current densities $J_C$.

## 2.2 Microscopic transport models

### 2.2.1 The Landauer formalism

The Landauer formalism is often used to calculate ballistic heat or charge current of a system that is out of equilibrium. Despite the Landauer formalism is usually used to consider ballistic transport, it can also be used to calculate diffusive transport. In the Landauer formalism we consider two contacts which are connected via a conduction channel. Each contact is in equilibrium with a different reservoir. The two reservoirs can differ in their thermodynamic parameters such as temperature or chemical potential. The channel is characterized by a transmission function. The transmission function depends on the energy and the quantum numbers of the particles that carry the current. The contacts are reflection free, this means particles can enter the contacts from the channel without being backscattered. In the following the quantum states of these systems are labeled by $k_x$, $k_y$ and $k_z$. The particle current density per energy can be deduced from $j_N(E) = n(E)v(E)$, where $n(E)$ is the particle density and $v(E)$ is the velocity in transport direction. The particle density $n(E)$ can be related to the density of states in the channel. Therefore

$$n(E) = \frac{1}{(L_x L_y L_z)} \sum_k \delta(E - E(k)) \cdot f(E), \tag{2.21}$$

where $f(E)$ is the occupation function. A corresponding expression can be found for $v(E)$,

$$v(E) = \frac{\sum_k vz_k \delta(E - E(k))}{\sum_k \delta(E - E(k))}. \tag{2.22}$$

$vz_k$ is the velocity of state k in z direction and can be expressed as a derivative of the energy $vz_k = \frac{1}{\hbar}\frac{\partial E}{\partial k_z}|_k$. $j_N(E)$ can then be expressed as follows

$$j_N(E) = \frac{1}{(L_x L_y L_z)} \sum_k \frac{1}{\hbar}\frac{\partial E}{\partial k_z}|_k \delta(E - E(k)) f(E). \tag{2.23}$$

The sum over $k_z$ can be converted into an integral $k_z \longrightarrow \frac{L_z}{2\pi} \int dk_z$. Then (2.23) can be rewritten to obtain

$$j_N(E) = \frac{1}{(L_x L_y h)} \sum_{k_x,k_y} \int dk_z \frac{\partial E}{\partial k_z}|_k \delta(E - E(k)) f(E). \tag{2.24}$$

It is useful to divide the particle current into a part that is moving in positive z direction $j_+$ and a part that is moving in negative z direction $j_-$. Considering in equation (2.24) the particles with positive velocity in z direction and using the properties of the Dirac function leads to

$$j_+(E) = \frac{1}{(L_x L_y h)} f_+ \sum_{k_p} \sum_{k_z + (k_p, E)} . \tag{2.25}$$

Here $k_x$ and $k_y$ are summarized to $k_p$. $f_+$ is the occupation function for the particles that are moving in positive z direction. $\sum_{k_z+(k_p,E)}$ is the number of positive solutions of $E(k_p, k_z) - E = 0$. This quantity is called the number of modes or the number of bands $M(k_p, E)$.

Considering again the system which consists of the two contacts and the channel, but now with a scatterer within the channel, which is shown in Fig.2.6. The left contact injects particles into the channel that are moving in z direction $j_+$, whereas the right contact injects particles into the channel that are moving in negative z direction $j_-$. The channel is described through a transmission function $t(E, k_p)$. The transmission function depends on $k_p$ and $E$ and gives the fraction of the current per mode that passes the channel. Hence, the transmission function can take values between 0 and 1. Therefore, the current from left to right $j_{l\to r}(E)$ is given by

$$j_{l\to r}(E) = \frac{1}{(L_x L_y h)} f_l(E) \sum_{k_p} M(k_p, E) t_{l\to r}(E, k_p). \tag{2.26}$$

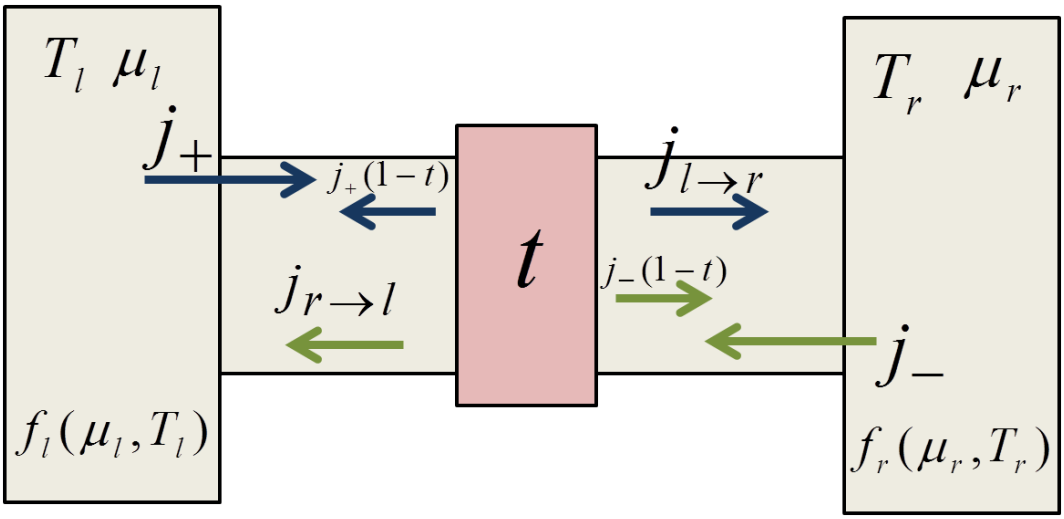


Figure 2.6: Sketch of the particle fluxes in the Landauer picture. The left contact injects a particle flux $j_+$ into the channel. A fraction of this current $j_+(1-t)$ is reflected, whereas the rest $j_+ t = j_{l\to r}$ is transmitted. The same holds for the current which is injected from the right contacts. The net current from contact left to contact right is given by the difference between $j_{r\to l}$ and $j_{l\to r}$

.

Since the particles that are moving in positive z direction are injected from the left contact, the occupation function $f_+$ is given by the occupation function of the left contact $f_l$. Therefore $f_+$ can be replaced by $f_l$. The time reversal symmetry requires $t_{l\to r}(E, k_p) = t_{r\to l}(E, k_p)$. With these relations the particle current density $j_N = j_{l\to r} - j_{r\to l}$ is given by

$$j_N(E) = \frac{1}{(L_x L_y h)}(f_l(E) - f_r(E))\overline{t(E)}, \tag{2.27}$$

with

$$\overline{t(E)} = \sum_{k_p} M(k_p, E) t_{l\to r}(k_p, E). \tag{2.28}$$

$\overline{t(E)}$ is the total transmission function of the system. The total transmission function is written as

$$\overline{t(E)} = M(E) \cdot t(E), \tag{2.29}$$

where

$$M(E) = \sum_{k_p} M(k_p, E), \tag{2.30}$$

are the total number of modes per energy and

$$t(E) = \frac{\sum_{k_p} M(k_p, E) t_{l\to r}(k_p, E)}{M(E)}, \tag{2.31}$$

is the average transmission probability at energy $E$.
The total particle current $J_N$ is the integral of equation (2.27)

$$J_N = \int \frac{1}{(L_x L_y h)} \overline{t(E)}(f_l(E) - f_r(E))dE. \tag{2.32}$$

Equation (2.32) is a generalized form of the well know Landauer formula which states that one mode with spin degeneracy can carry a current of $\frac{2e}{h}$. The quantity $\frac{2e}{h}$ is called quantum conductance. The Landauer formula itself is formulated for the charge current $J_C$ of one mode

$$J_C = \int \frac{2e}{(h)} t(E)(f_l(E) - f_r(E))dE. \tag{2.33}$$

Now the expressions for $\sigma$, S, and $\kappa_e$ are derived from equation (2.32). The particle and charge currents are connected by $j_C = e \cdot j_N$, whereas the particle and heat currents $j_h$ are connected by $j_h = j_n(E - \mu)$.

Since in thermoelectrics the gradients that arise are rather small the Landauer formalism in thermoelectrics is often used in the linear response regime. However it is worth to notice that the Landauer formalism is not restricted to small gradients. In the linear response regime the Fermi function $f$ can be expanded around an equilibrium $\mu$ and T

$$f_i(E, \mu_i, T_i) = f(E, \mu, T) - \partial_E f(E, \mu, T)(\mu - \mu_i) - (E - \mu)\partial_E f(E, \mu, T)\frac{T - T_i}{T}, \tag{2.34}$$

with i ∈ l,r. Inserting equation (2.34) in equation (2.32) leads to the following expression for the charge current

$$\begin{aligned} J_C =& \frac{L_z}{L_x L_y}\frac{2e^2}{h}\int \overline{t(E)}(-\partial_E f(E,\mu,T))dE\frac{(\mu_r-\mu_l)}{eL_z}+ \\ & \frac{L_z}{L_x L_y}\frac{2e}{hT}\int \overline{t(E)}(E-\mu)(-\partial_E f(E,\mu,T))dE\frac{(T_r-T_l)}{L_z} \end{aligned} \tag{2.35}$$

and heat current

$$\begin{aligned} J_H =& \frac{L_z}{L_x L_y}\frac{2e}{h}\int \overline{t(E)}(E-\mu)(-\partial_E f(E,\mu,T))dE\frac{(\mu_r-\mu_l)}{eL_z}+ \\ & \frac{L_z}{L_x L_y}\frac{2}{hT}\int \overline{t(E)}(E-\mu)^2(-\partial_E f(E,\mu,T))dE\frac{(T_r-T_l)}{L_z}. \end{aligned} \tag{2.36}$$

Comparing equations (2.35) and (2.36) with equation (2.5) one can obtain the coefficients $L_{nm}$ in the Landauer formalism

$$L_{11} = e^2 L_0, \tag{2.37a}$$

$$L_{12} = L_{21}\frac{1}{T} = \frac{e}{T}L_1, \tag{2.37b}$$

$$L_{22} = \frac{1}{T}L_2, \tag{2.37c}$$

with

$$L_n = \frac{L_z}{L_x L_y}\frac{2}{h}\int \overline{t(E)}(E-\mu)^n(-\partial_E f(E,\mu,T))dE. \tag{2.38}$$

Using the link between the $L_{nm}$ and the thermoelectric parameters (2.10) one can obtain the expression of the thermoelectric coefficients in the Landauer formalism

$$\sigma = e^2 L_0, \tag{2.39a}$$

$$S = -\frac{1}{eT}\frac{L_1}{L_0}, \tag{2.39b}$$

$$\kappa_e = \frac{1}{T}\left(L_2 - \frac{L_1^2}{L_0}\right). \tag{2.39c}$$

Besides $\sigma$, S, and $\kappa_E$ there is one other important thermoelectric parameter $\kappa_p$. $\kappa_p$ is the phonon contribution to the heat conductance. $\kappa_p$ can be derived in the Landauer formalism in a similar way to $\kappa_e$. Since phonons are bosons

there is no chemical potential, therefore the expansion of the Bose-Einstein distribution is only carried out around an equilibrium T

$$f_i(E,T_i) = f(E,T) - \partial_T f(E,T)(T-T_i). \tag{2.40}$$

The energy of a phonon is $\hbar\omega$. Using equation (2.27) the phonon heat current density is given by

$$J_{hp} = \frac{L_z}{L_x L_y}\frac{1}{2\pi}\int \hbar\omega\overline{T(\hbar\omega)}(-\partial_\omega f(\hbar\omega,T))d\omega\frac{(T_r-T_l)}{L_z}. \tag{2.41}$$

Since $\kappa_p$ is defined as $\frac{J_{hp}}{\frac{\Delta T}{L_z}}$, $\kappa_p$ is given by

$$\kappa_p = \frac{L_z}{L_x L_y}\frac{1}{2\pi}\int \hbar\omega\overline{T(\hbar\omega)}(-\partial_\omega f(\hbar\omega,T))d\omega. \tag{2.42}$$

### 2.2.2 The Boltzman transport equation (BTE)

Another common approach to calculate the thermoelectric parameters is the Boltzman transport equation (BTE). In the BTE particles are treated semi classically. This means on the one hand the particles have sharp coordinates in space and momentum and show no interference effects, but on the other hand the particles obey the Pauli's principle and their transition probabilities are calculated using quantum mechanics. The central quantity in the BTE is the distribution function $f(x,p)$, where $x$ and $p$ are the position in real space and momentum space. $f(x,p)$ is the probability that a state at position $x$ and momentum $p$ is occupied. The total derivative of $f(x,p)$ with respect to time is

$$\frac{df}{dt} = v\nabla f + F\nabla_p f + \partial_t f, \tag{2.43}$$

where $v$ is the velocity and $F = \partial_t p$ is the force. $\frac{df}{dt}$ is the total derivative and can be only unequal zero if scattering mechanism are present. A common approach to describe scattering is the Stoßzahl ansatz. In this approach only two particle interactions on the same place are taken into account. The total derivative in this approach is given by

$$\frac{df}{dt} = \int \left[dp' S(p',p)f(x,p',t)(1-f(x,p,t)) - S(p,p')f(x,p,t)(1-f(x,p',t))\right]. \tag{2.44}$$

$S(p,p')$ is the transition matrix element between state $p$ and $p'$. The first term of the integrand in equation (2.44) counts all in-scattering particles in state $p$, while the second term of the integrand counts all out-scattering particles from state $p$. The whole integral is called the collision integral. One common approach for the collision integral is the relaxation time approximation(RTA).

In this appoach $f$ is divided into an part that is symmetric in momentum space $f_s$ and part that is asymmetric in momentum space $f_a$. The system is assumed to be near equilibrium, therefore $f_s \approx f_0$ and $f_s >> f_a$, where $f_0$ is the equilibrium distribution function. Furthermore, it is assumed that $(1 - f(x, p, t)) \approx 1$. The collision integral can then be written as

$$\frac{df}{dt} = \int dp^{'} S(p^{'}, p) f(x, p^{'}, t) - f(x, p, t) \int dp^{'} S(p, p^{'}). \tag{2.45}$$

For the next simplification one assumes that the in-scattering is only governed by the equilibrium part of the distribution function and can be written as

$$\int dp^{'} S(p^{'}, p) f(x, p^{'}, t) = \frac{f_0}{\tau}, \tag{2.46}$$

whereras $\frac{1}{\tau} = \int dp^{'} S(p, p^{'})$ is the scattering rate. With this simplifications the BTE in the RTA reads

$$\frac{df}{dt} = \frac{f_0(x, p, t)}{\tau} - \frac{f(x, p, t)}{\tau} = -\frac{f_a}{\tau}. \tag{2.47}$$

To get the thermoelectric coefficients in the BTE again the BTE in the RTA is considered

$$\frac{df}{dt} = v\nabla f + F\nabla_p f = -\frac{f_a}{\tau}. \tag{2.48}$$

Since no external forces are considered $F = 0$ holds. An electronic system is considered, which means that for the distribution function $f$ the Fermi function is used. If the spatial dependence of $f$ is only due to the chemical potential and temperature $f_a$ can be written as

$$f_a = \tau(\partial_E f(E(p), \mu(r), T(r)))v \left( (-\nabla\mu) - (E - \mu)\frac{1}{T}\nabla_T \right). \tag{2.49}$$

From now on instead of $p$ the particles are labeled with $k$, where $k$ is the quantum mechanical wave number. The relation between $k$ and $p$ is $p = \hbar k$. The net particle current in z direction can be calculated by adding up all particles and weight them with the velocity in z direction $vz_k$, which leads to

$$J_N = \frac{2}{L_x L_y L_z} \sum_k v z_k f_a(k). \tag{2.50}$$

Here only the asymmetric part is considered since $\sum_k v z_k f_s(k) = 0$. The factor

2 occurs because of the spin. The charge and heat currents are then given by

$$J_C = \frac{2}{L_x L_y L_z} \sum_k e v z_k f_a(k) \tag{2.51a}$$

$$J_H = \frac{2}{L_x L_y L_z} \sum_k (E(k) - \mu) v z_k f_a(k). \tag{2.51b}$$

Inserting $f_a$ from equation (2.49) in equation (2.51) yields

$$J_C = \frac{2}{L_x L_y L_z} \left( \sum_k e^2 (-\partial_E f) \tau_k v z_k^2 \frac{\nabla \mu}{e} + \sum_k \frac{e}{T} (-\partial_E f) \tau_k v z_k^2 (E(k) - \mu) \nabla T \right) \tag{2.52a}$$

$$J_H = \frac{2}{L_x L_y L_z} (\sum_k e(E(k) - \mu)(-\partial_E f) \tau_k v z_k^2 \frac{\nabla \mu}{e} + \sum_k \frac{1}{T} (-\partial_E f) \tau_k v z_k^2 (E(k) - \mu)^2 \nabla T). \tag{2.52b}$$

Comparing equations (2.52) with equation (2.5) one can obtain the coefficients $L_{nm}$ in the BTE.

$$L_{11} = e^2 h_0 \tag{2.53a}$$

$$L_{12} = L_{21} \frac{1}{T} = \frac{e}{T} h_1 \tag{2.53b}$$

$$L_{22} = \frac{1}{T} h_2 \tag{2.53c}$$

with

$$h_n = \frac{2}{L_x L_y L_z} \sum_k \tau_k v z_k^2 (E(k) - \mu)^n (-\partial_E f(k, \mu, T)). \tag{2.54}$$

It is often convenient to replace the summation over the $k$ states with an integral over energy, using the definition of the density of states, $h_n$ can be written as

$$h_n = \frac{2}{L_x L_y L_z} \int \sum_k \tau_k v z_k^2 (E - \mu)^n (-\partial_E f(E, \mu, T)) \delta(E - E(k)) dE. \tag{2.55}$$

Introducing the transport distribution function $\Sigma(E) = \frac{h}{L_z^2} \sum_k v z_k^2 \tau_k \delta(E - E(k))$ equation (2.55) reads

$$h_n = \frac{2 L_z}{h L_x L_y} \int \Sigma(E) (E - \mu)^n (-\partial_E f(E, \mu, T)) dE. \tag{2.56}$$

### 2.2.3 Landauer vs BTE

Equation (2.38) and equation (2.56) have the same formal structure. The only difference are the quantities $\Sigma$ and $\bar{t}$. $\Sigma$ can be rewritten to

$$\Sigma = \frac{h}{L_z^2} \frac{\langle vz^2 \tau_k \rangle}{\langle |vz| \rangle} \sum_k |vz_k| \delta(E - E(k)) \tag{2.57}$$

with

$$\langle |vz| \rangle = \frac{\sum_k |vz_k| \delta(E - E(k))}{\sum_k \delta(E - E(k))} \tag{2.58}$$

and

$$\left\langle vz^2 \tau \right\rangle = \frac{\sum_k vz_k^2 \tau_k \delta(E - E(k))}{\sum_k \delta(E - E(k))}. \tag{2.59}$$

Since $\Sigma$ corresponds to $\bar{t} = M(E)t(E)$ the following expression for the numbers of modes can be found [35]

$$M(E) = \frac{h}{2L_z} \sum_k |vz_k| \delta(E - E(k)). \tag{2.60}$$

The transmission function $t(E)$ can be related to

$$t(E) = 2 \frac{\langle vz^2 \tau \rangle}{\langle |vz| \rangle L_z}. \tag{2.61}$$

In the diffusive limit the transmission function and the mean free path for backscattering are linked by [28]

$$t(E) = \frac{\lambda}{L_z}. \tag{2.62}$$

If the following definition for the mean free path for backscattering is choosen

$$\lambda(E) = 2 \frac{\langle vz^2 \tau \rangle}{\langle |vz| \rangle}, \tag{2.63}$$

the results from Landauer formalism agree with the results obtained from the BTE [35].

## 2.3 Electronic structure and lattice vibrations

Starting point is the Hamilton operator of a solid [36]

$$H = T_K + T_e + V_{K-K} + V_{e-e} + V_{e_K} \tag{2.64}$$

where

- $T_K$ is the kinetic energy of the ions,
- $T_e$ is the kinetic energy of the electrons,
- $V_{e-e}$ is the electron-electron interaction,
- $V_{K-K}$ is the ion-ion interaction, and
- $V_{e-K}$ is the electron-ion interaction .

The kinetic energy term of the ions $T_K$ scales with the factor of $m_e/M_k$ compared to the kinetic energy term $T_e$ for the electrons, in which $m_e$ is the electron mass and $M_K$ is the mass of the ions. In a solid the factor $m_e/M_k$ is approximately $10^{-4} - 10^{-5}$. Therefore it is reasonable to perform a calculation of perturbation, where the kinetic energy of the ions are treated as a perturbation of the electronic system. The overall Hamilton operator is then decomposed in

$$H = H_0 + T_K. \tag{2.65}$$

$H_0$ is Hamilton operator of the electronic system. $H_0$ has the form

$$H_0 = T_e + V_{K-K}(\vec{R}) + V_{e-e}(\vec{r}) + V_{e-K}(\vec{r}, \vec{R}), \tag{2.66}$$

where $\vec{r}$ are the coordinates of the electrons and $\vec{R}$ are the coordinates for the ions. For the pure electronic system $\phi_\alpha(\vec{r}, \vec{R})$ and $\epsilon_\alpha(\vec{R})$ are the wave functions and eigenenergies, respectively. The Schrödinger equation for the electronic system is given by

$$H_0\phi_\alpha(\vec{r}, \vec{R}) = \epsilon_\alpha(\vec{R})\phi_\alpha(\vec{r}, \vec{R}). \tag{2.67}$$

The coordinates of the ions enter this equation only as a parameter, because in $H_0$ the term for the kinetic energy of the ions is missing. Since the $\phi_\alpha(\vec{r}, \vec{R})$ are a complete set of eigenfunctions, the solution of the overall Hamiltonian can be expanded in terms of the $\phi_\alpha(\vec{r}, \vec{R})$. The overall wave function can then be written as

$$\psi(\vec{r}, \vec{R}) = \sum_\alpha \chi_\alpha(\vec{R})\phi_\alpha(\vec{r}, \vec{R}). \tag{2.68}$$

Inserting this in the Schrödinger equation of the solid

$$H\psi(\vec{r},\vec{R}) = E\psi(\vec{r},\vec{R}) \tag{2.69}$$

yields

$$\sum_{\alpha}\left(\epsilon_\alpha(\vec{R}) + T_K - E\right)\chi_\alpha(\vec{R})\phi_\alpha(\vec{r},\vec{R}) = 0. \tag{2.70}$$

Multiplying with $\phi^*_\alpha$ and integration over $r$ yields

$$\left(T_K + \epsilon_\beta(\vec{R})\right)\chi_\beta(\vec{R}) + \sum_{\alpha} A_{\beta,\alpha}(\vec{R})\chi_\alpha(R) = E\chi_\beta(\vec{R}) \tag{2.71}$$

with

$$A_{\beta,\alpha}(\vec{R}) = \\ -\sum_l \frac{\hbar^2}{2M_l}\int d\vec{r}\left[\phi^*_\beta(\vec{r},\vec{R})\frac{\partial^2}{\partial\vec{R_l}^2}\phi_\alpha(\vec{r},\vec{R}) + 2\phi^*_\beta(\vec{r},\vec{R})\left(\frac{\partial}{\partial\vec{R_l}}\phi_\alpha(\vec{r},\vec{R})\right)\frac{\partial}{\partial\vec{R_l}}\right]. \tag{2.72}$$

The $A_{\beta,\alpha}(\vec{R})$ describing transitions between different electronic states. Neglecting these terms yields a Schrödinger-equation for the phonons

$$\left(T_K + \epsilon_\beta(\vec{R})\right)\chi_\beta(\vec{R}) = E\chi_\beta(\vec{R}). \tag{2.73}$$

The equation (2.71) has no approximations. Neglecting the $A_{\beta,\alpha}(\vec{R})$ is called the Born-Oppenheimer approximation. It can be shown, that the error made by these approximation scales with $\left(\frac{m_e}{M_k}\right)^{1/4}$ [36]. The Born-Oppenheimer approximation decouples the electron and phonon interaction. There are several methods to reintroduced the electron-phonon-interaction.

Considering equation (2.73) we can identify the $\epsilon_\beta$ as the potential of the phonons. In principle there is a potential for the phonons for each electronic state $\epsilon_\beta$. In this work only the potential of the phonons for the electronic ground state $\epsilon_0$ is considered. From now on the phonon potential of the electronic ground state will be denoted as $V$.

### 2.3.1 The phonon structure

The potential of the phonons $V$ depends on all ionic coordinates, which are labeled with $\vec{R} = R_1, ..., R_N$. Expanding $V(R_1, ..., R_N)$ around the equilibrium positions $\vec{R_0} = (R^0_1, ..., R^0_N)$, which are also the positions at which the potential has a minimum, yields

$$V(R_1, ..., R_N) = V(\vec{R_0}) + \sum_{k\alpha}\frac{\partial V}{\partial R_{k\alpha}}|_{\vec{R_0}}\cdot u_{k\alpha} + \frac{1}{2}\sum_{k\alpha l\beta}\frac{\partial^2 V}{\partial R_{k\alpha}\partial R_{l\beta}}|_{\vec{R_0}}\cdot u_{k\alpha}u_{l\beta} + ... \tag{2.74}$$

Here $k$ and $l$ are labeling the different ions and $\alpha$ and $\beta$ are labeling the Cartesian coordinates x,y and z. In (2.74) the first term on the right side is a constant and therefore has no influence on the dynamics of the system. The second term on the right side is zero since $V$ is expanded around a minimum. Truncating the series in (2.74) after the quadratic term is called the harmonic crystal approximation. The quantities

$$\frac{\partial^2 V}{\partial R_{k\alpha} \partial R_{l\beta}} = \Phi_{k\alpha l\beta} \tag{2.75}$$

are called inter atomic force constants (ifcs). In the harmonic crystal approximation the ifcs are enough to describe completely the lattice dynamics. There are several models and procedures to describe the interatomic potential $V$ ranging from purely empirical to *ab initio* methods. A famous example for an empirical model is the Lennard-Jones-Potential

$$V(R_1, ..., R_N) = 4\epsilon \sum_{i<j} \left( \frac{\sigma^{12}}{R_{ij}} - \frac{\sigma^6}{R_{ij}} \right). \tag{2.76}$$

$R_{ij}$ is the Vector $R_i - R_j$. $\epsilon$ and $\sigma$ are usually fitted to experiments. The Lennard-Jones-Potential is used to describe van-der-Waals-interactions.

For ion bondings with binding length $a$, a potential based on the coulomb interaction is often used

$$V(R_1, ..., R_N) = \left( \lambda e^{Z \frac{-R_{12}}{\sigma}} - \alpha \frac{Q^2}{a} \right). \tag{2.77}$$

$\alpha = \sum_{j \neq i} \frac{sign(Q_i Q_j)}{R_{ij}/a}$ is the Madelung constant and Z is the number of next neighbours. The first term in equation (2.77) describes the repulsive part of the bonding, which in this model only appears between next neighbours. The last term in equation (2.77) describes the coulomb interaction of the ions.

Also a common model for the atomic bonding is the spring model. In this model one describes the bonds between the atoms as springs

$$V(R_1, ..., R_N) = \sum_{i \neq j} \frac{1}{2} K_{ij} R_{ij}^2. \tag{2.78}$$

$K_{ij}$ is the spring constant between atom $i$ and atom $j$. In a one dimensional treatment the spring model coincidence with the harmonic crystal approximation of the spring model. If more dimensions are considered the harmonic crystal approximation of the spring model is an approximation of the spring model.

Up to now the presented models require experimental data since all of them rely on fit parameters. A method to calculate the interatomic potential $V$ from *ab inito* is based on the density functional theory (DFT). The main idea to calculate the interatomic potential is to compute the total energy under

variation of the atomic positions. There are some more or less sophisticated techniques to obtain the ifcs, which are explained in section 2.3.2.

Once the potential is obtained there are in principle two ways to handle to lattice vibrations. One can use a classic approach, in which the equations of motion for the ions are solved using Newtons laws. The second approach is a quantum mechanical approach, where the Schroedinger equation for the phonons (2.73) is solved. In both approaches one can obtain the correct dispersion relation, but only in the quantum mechanical approach the quantization of the lattice vibration arise. Since the quantum mechanical treatment is more complicated and computational more demanding, a common way to handle the lattice vibrations is to calculate the dispersion relation in the classical approach and introduce the quantization by definition. In this work the classical approach is employed, but for the sake of completeness the quantum mechanical approach is presented for the example of a linear chain.

#### 2.3.1.1 Quantum mechanical treatment of lattice vibrations

In the quantum mechanical treatment of the lattice vibrations the Schroedinger equation for the phonons (2.73) is solved. A linear chain with $N$ particles of mass $M$ and periodic boundary conditions is considered. For the potential a simple spring model is used. Consequently, the Hamiltonian of the system becomes

$$H = \sum_{s=1}^{n} \left( \frac{1}{2M} p_s^2 + \frac{1}{2} K (q_{s+1} - q_s)^2 \right). \tag{2.79}$$

$K$ is the spring constant, $p_s$ is the momentum of particle $s$, and $q_s$ is the displacement of particle $s$ out of equilibrium. The coordinates can be decoupled using the Fourier transformations

$$q_s = \frac{1}{\sqrt{N}} \sum_k Q_k e^{iksa} \tag{2.80}$$

and

$$p_s = \frac{1}{\sqrt{N}} \sum_k P_k e^{-iksa}. \tag{2.81}$$

$k$ can take the values $k = \frac{2\pi n}{Na}$, $n = 0, \pm 1, \pm 2, .... \frac{1}{2}N$. $a$ is the spacing of the particles in equilibrium positions. With these transformations equation (2.79) reads

$$H = \sum_k \left( \frac{1}{2M} P_k P_{-k} + \frac{1}{2} M \omega_k^2 Q_k Q_{-k} \right) \tag{2.82}$$

with

$$\omega_k = \sqrt{\frac{2K}{M}} \left(1 - \cos ka\right)^{\frac{1}{2}} . \tag{2.83}$$

From the commutation relation of $q_s$ and $p_s$ $[q_r, q_s] = i\hbar\delta(r, s)$ the commutation relation for $Q_k$ and $P_{k'}$ follows

$$[Q_k, P_{k'}] = i\hbar\delta(k, k'). \tag{2.84}$$

The Hamilton operator in equation (2.82) describes $n$ independent oscillators.

In analogy to a the quantum mechanical treatment of a single oscillator the Hamiltonian (2.82) can be expressed in terms of creation $a_k^\dagger$ and annihilation $a_k$ operators

$$a_k^\dagger = \sqrt{\frac{1}{2\hbar}} \left[(M\omega_k)^{\frac{1}{2}} Q_{-k} - i(M\omega_k)^{-\frac{1}{2}} P_k\right] \tag{2.85}$$

$$a_k = \sqrt{\frac{1}{2\hbar}} \left[(M\omega_k)^{\frac{1}{2}} Q_k + i(M\omega_k)^{-\frac{1}{2}} P_{-k}\right] . \tag{2.86}$$

Using these transformations the Hamiltonian (2.82) becomes

$$H = \sum_k \hbar\omega_k \left(a_k^\dagger a_k + \frac{1}{2}\right) . \tag{2.87}$$

Using the commutation relation (2.84) one can obtain the commutation relation for $a_k^\dagger$ and $a_{k'}$

$$[a_{k'}, a_k^\dagger] = \delta(k, k'). \tag{2.88}$$

Equation (2.87) describes a set of harmonic oscillator with different frequencies $\omega_k$. Therefore, the interpretation of a single harmonic oscillator can be used to describe the quantum mechanical system. The operator $a_k^\dagger a_k$ is the particle number operator $n_k$ and counts the number of particles with quantum number $k$. The possible energies for each $k$ state are therefore quantized and obey

$$E_k = \left(n_k + \frac{1}{2}\right) \hbar\omega_k. \tag{2.89}$$

One can see, that the dispersion relation $\omega_k$ from equation (2.83) coincidence with the dispersion relation of a linear chain in a classical treatment. For almost all quantities which are related to lattice vibration like heat capacity or thermal conductance the most important function is the dispersion relation. The dispersion relation together with the relation (2.89) and the correct occupation function is therefore enough to calculate all the relevant quantities. Thus, it is convenient to calculate the dispersion relation with classical physics and use equation (2.89) to get the link between the frequency $\omega$ and energy $E$.

### 2.3.1.2 Classical treatment of lattice vibrations

In this section the dispersion relation for lattice vibrations are derived from classical mechanics. A lattice is considered with lattice vectors $R_{n0}$ and with $r$ atoms in the basis. The position of the $\mu$'s atom in unit cell $n$ can be designated with $R_{n\mu}$. The position vector $R_{n\mu}$ can be decomposed in

$$R_{n\mu} = R_{n0} + R_\mu + u_{n\mu}, \tag{2.90}$$

where $R_{n0}$ is the vector to the origin of cell $n$, see Fig. 2.7. $R_\mu$ is the equilibrium position vector of atom $\mu$ in the cell and $u_{n\mu}$ is the displacement vector of atom $\mu$ in cell $n$. A potential in the harmonic crystal approximation (2.74) is considered. Then the equations of motion are

$$M_\mu \ddot{u}_{n\mu\alpha} = -\frac{\partial V}{\partial u_{n\mu\alpha}} = -\sum_{n'\mu'\alpha'} \Phi_{n\mu\alpha,n'\mu'\alpha'} u_{n'\mu'\alpha'}. \tag{2.91}$$

$\Phi_{n\mu\alpha n'\mu'\alpha'}$ is the interatomic force constant between atom $\mu$ in cell $n$ and atom $\mu'$ in cell $n'$. The index $\alpha$ and $\alpha'$ labeling the three different Cartesian coordinates x,y and z. Thus the force constant between two atoms is in general a 3x3 matrix. The physical interpretation of the force constant can be derived from equation (2.91). $\Phi_{n\mu\alpha n'\mu'\alpha'}$ is the force in $\alpha$-direction on the $\mu$th atom in cell n, when the $\mu'$th atom in cell $n'$ is displaced in $\alpha'$-direction. Because of the translation invariance of the lattice, $\Phi_{n\mu\alpha n'\mu'\alpha'}$ can only depend on the relative distance vector $R_{n0} - R_{n'0}$. Thus $\Phi_{n\mu\alpha n'\mu'\alpha'}$ can be written as

$$\Phi_{n\mu\alpha n'\mu'\alpha'} = \Phi_{\mu\alpha\mu'\alpha'}(R_{n0} - R_{n'0}). \tag{2.92}$$

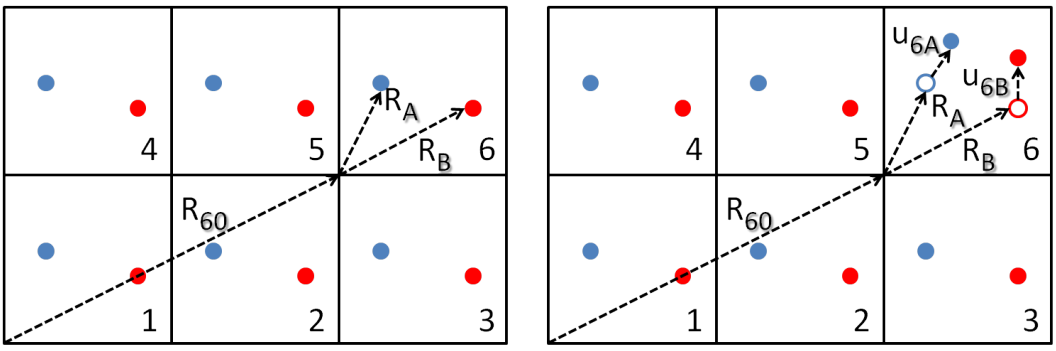


Figure 2.7: Sketch of a two atomic lattice with lattice vector $R_{60}$, equilibrium positions of the atoms $R_A$, $R_B$ and displacement vectors of the atoms $u_{6A}$, $u_{6B}$.

Then equation (2.91) reads

$$M_\mu \ddot{u}_{n\mu\alpha} = -\sum_{n'\mu'\alpha'} \Phi_{\mu\alpha\mu'\alpha'}(R_{n0} - R_{n'0}) u_{n'\mu'\alpha'}. \tag{2.93}$$

To solve this equation the following ansatz is used

$$u_{n\mu\alpha}(t) = \frac{1}{\sqrt{M_\mu}}\nu_{n\mu\alpha}e^{i(qR_{n0}-\omega t)}. \tag{2.94}$$

Then equation (2.93) becomes

$$\omega^2\nu_{\mu\alpha} = \sum_{n'}\sum_{\mu'\alpha'} D_{\mu\alpha,\mu'\alpha'}(R_{n0} - R_{n'0})e^{iq(R_{n'0}-R_{n0})}\nu_{\mu'\alpha'} \tag{2.95}$$

with

$$D(R) = \frac{1}{\sqrt{M_\mu M_{\mu'}}}\Phi(R). \tag{2.96}$$

Because of the translation invariance of the system equation (2.95) can not depend on $n$ since the dynamics of the system can not depend on the actual cell. Thus equation (2.95) can be simplified to

$$\omega^2\nu_{\mu\alpha} = \sum_{R}\sum_{\mu'\alpha'} D_{\mu\alpha,\mu'\alpha'}(R)e^{-iqR}\nu_{\mu'\alpha'}, \tag{2.97}$$

where $R = R_{n0} - R_{n'0}$.

The Fourier transform of the $D_{\mu\alpha,\mu'\alpha'}$ is called the dynamical matrix

$$D(q) = \sum_{\mu'\alpha'} D_{\mu\alpha,\mu'\alpha'}(R)e^{-i(qR)}. \tag{2.98}$$

Using the dynamical matrix, equation (2.98) becomes an eigenvalue equation

$$\omega^2\nu_{\mu\alpha} = \sum_{\mu'\alpha'} D_{\mu\alpha,\mu'\alpha'}(q)\nu_{\mu'\alpha'}. \tag{2.99}$$

The benefit of the transformation from equation (2.91) to equation (2.99) is a reduction in complexity. Equation (2.91) describes the coupling between $n \cdot r \cdot 3$ equations. In equation (2.97) there are only $r \cdot 3$ equations, which depend on $q$. Since the number of degrees of freedom must be fixed there must be $n$ different $q$ values. The $q$ values depend on the boundary conditions. A common approach to model the boundary conditions is the use of periodic boundary conditions, which will be discussed in the next paragraph.

#### 2.3.1.3 Periodic boundary conditions

From the periodic boundary conditions the equation

$$f(r) = f(r + N_\alpha a_\alpha) \tag{2.100}$$

must be fulfilled for all physical quantities. $a_\alpha$ is the primitive translation of the system and $N_\alpha$ is the number of cells both in $\alpha$-direction. From equation (2.98) the dynamical matrix in real space $D(R)$ can be expressed as

$$D(R) = \frac{1}{N} \sum_{\mu'\alpha'} D_{\mu\alpha,\mu'\alpha'}(q) e^{i(qR)}. \tag{2.101}$$

From equation (2.100) and (2.101) the conditions for the $q$ vectors is

$$N_\alpha a_\alpha \cdot q = 2\pi q_\alpha N_\alpha = 2\pi l_\alpha, \tag{2.102}$$

where $l_\alpha$ is an integer number and $q = \sum_{\alpha=1}^{3} q_\alpha b_\alpha$. The $b_\alpha$ are the reciprocal lattice vectors. Therefore the $q_\alpha$ can take only the discrete values

$$q_\alpha = \frac{l_\alpha}{N_\alpha}. \tag{2.103}$$

In principle, there are infinite allowed $q$ vectors, but it is enough to take only q-values in the first Brillouin zone into account

$$l_\alpha \in \left\{ -\frac{N_\alpha}{2}, ..., \frac{N_\alpha}{2} - 1 \right\}. \tag{2.104}$$

the reason is that if a reciprocal lattice vector is added to $q$ the physics do not change. This is illustrated in Fig.2.8.

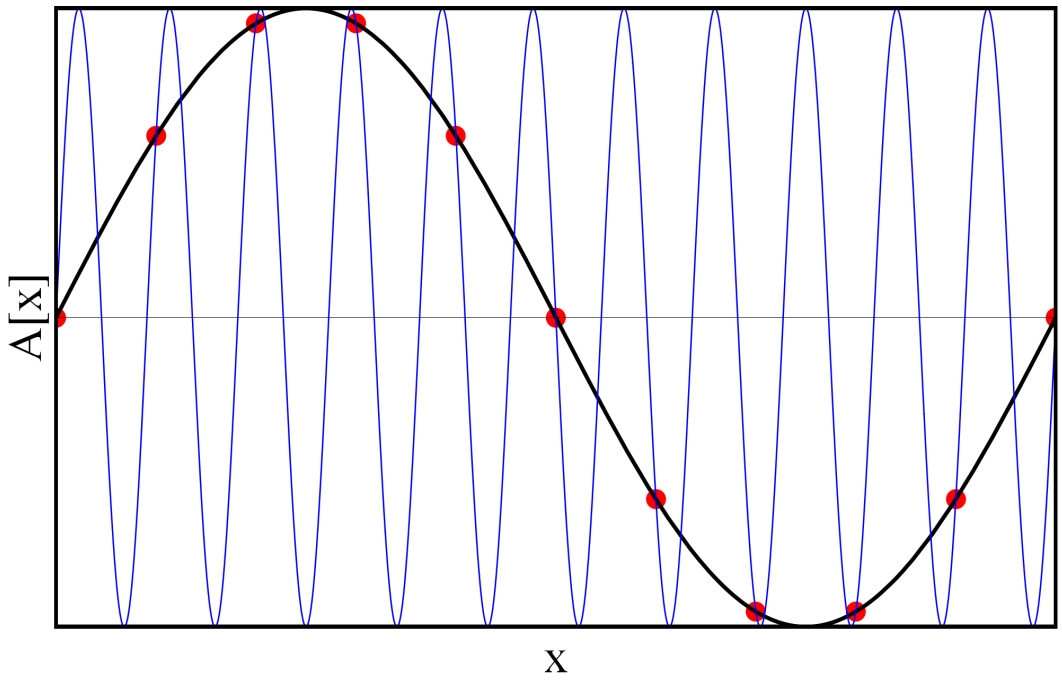


Figure 2.8: The same crystal vibration described by two different q. The red dots indicated the displacement A of the atoms.

Many calculations involve a summation over the Brillouin zone. Since in real systems the number of unit cells $N$ is very large and therefore the $q$ points

in the first Brillouin zone dense, the summation can be substituted by the integral

$$\sum_{q\in 1.Bz} = \frac{V}{(2\pi)^3}\int d^3q. \tag{2.105}$$

The dispersion relation can be obtained by calculating the eigenvalues of $D_{\mu\alpha,\mu'\alpha'}(q)$ for different $q$. The dimension of the matrix $D_{\mu\alpha,\mu'\alpha'}(q)$ is $r\cdot 3$. Thus there are $r\cdot 3$ eigenvalues for each $q$ point. The number $r\cdot 3$ is called number of modes $M$. The modes are split in 3 acoustic modes and $(r-1)3$ optical modes. For $q\to 0$ the acoustic modes are zero. From the dispersion relation the phonon density of states can be obtained, which is defined by

$$n_{ph}(\omega) = \sum_j \sum_{q\in 1.Bz} \delta(\omega - \omega_j(q)), \tag{2.106}$$

where $j$ labels the different modes.

As an example in Fig.2.9 the dispersion relation and phonon density of states of silicon is shown. There are 6 modes since Silicon has two atoms in the unit cell. One feature of the acoustic modes can be seen; for small $q$ die dispersion relation is linear. The acoustic modes are named that way, because the slope of the acoustic modes for low $q$ is the velocity of sound in the corresponding solid. Since for low $q$ the dispersion relation is linear, the density of states for low $q$ has always a quadratic $\omega$ dependence, which is derived in the following:

$$\begin{aligned} n_{ph}(\omega) = \sum_j \sum_{q\in 1.Bz} \delta(\omega-\omega_j(q)) &= 3\frac{V}{8\pi^3}\int sin(\theta)d\theta\int d\phi\int dqq^2\delta(\omega-\omega(q)) \\ &= 3\frac{V}{8\pi^3}\cdot 2\pi\cdot 2\int dqq^2\delta(q-\frac{\omega}{v})\frac{1}{v} \\ &= \frac{3V}{2\pi^3}\frac{\omega^2}{v^3} \end{aligned} \tag{2.107}$$

Here the same linear dispersion relation was assumed for all directions $\omega(q) = v\cdot q$, where $v$ is the speed of sound. The same calculation in 2 dimensions leads to a linear behavior and for 1 dimension to a constant behavior of the phonon density of states for small $w$.

### 2.3.2 Ab initio determination of the interatomic force constants

The interatomic force constants (ifcs) are the second derivative of $V(R)$

$$\frac{\partial^2 V}{\partial R_{k\alpha}\partial R_{l\beta}} = \Phi_{k\alpha l\beta}, \tag{2.108}$$

where $V(R)$ is the energy of the electronic system, which is the potential landscape of the atoms. The ifcs are linked to the force acting on the atoms by

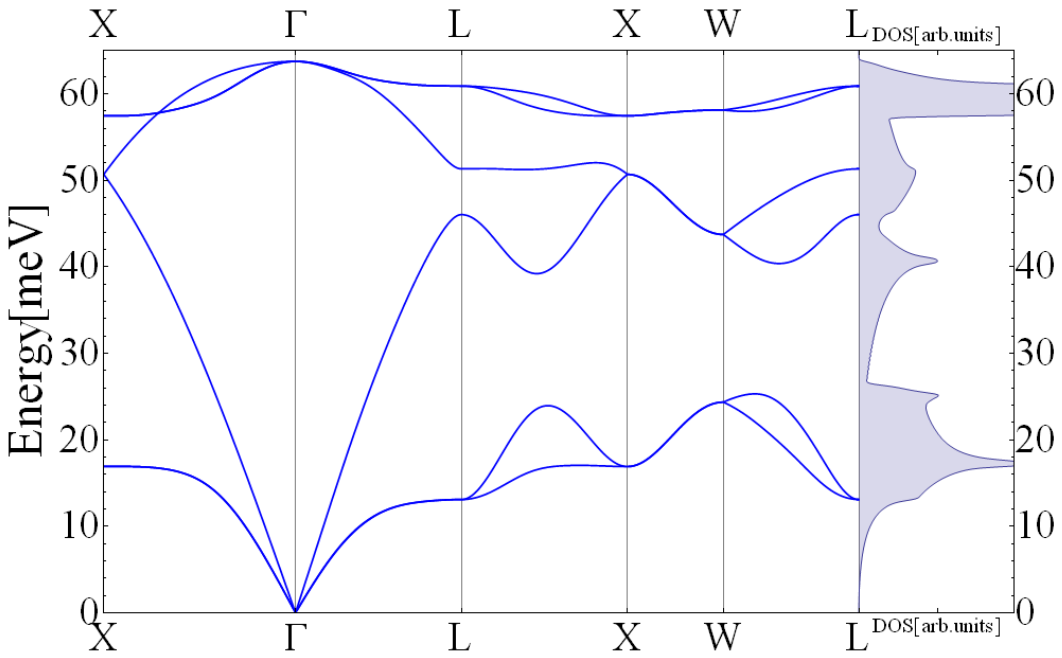


Figure 2.9: Dispersion relation and phonon density of states of Silicon

$$\Phi_{k\alpha l\beta} = -\frac{\partial F_{k\alpha}}{\partial R_{l\beta}}, \tag{2.109}$$

where $F_{k\alpha}$ is the force of atom $k$ in direction $\alpha$. Based on a DFT calculation there are in principle several methods to calculate the ifcs. The most intuitive approach is the small displacement method, which involves supercell calculations that leads to periodic boundary conditions for the phonons [37, 38]. In this method atom $l$ is displaced in direction $\beta$ from the equilibrium position. The force on atom $k$ in direction $\alpha$ is calculated. For small displacements of atom $l$ the force acting on atom $k$ is linear with the magnitude of the displacement. The ifcs are then obtained by using equation (2.109) and replacing the derivatives by finite differences to obtain

$$\Phi_{k\alpha l\beta} = -\frac{F_{k\alpha}}{\Delta R_{l\beta}}, \tag{2.110}$$

where $\Delta R_{l\beta}$ is the magnitude of the displacement. The ifcs obtained with this method are not exact because of periodic boundary effects. The error made with this technique increases with decreases with the size of the supercell. Therefore, this method requires large supercell calculations. In principle, the supercell has to be large enough that the impact on atom $k$ from atoms $l'$ can be neglected. The atoms $l'$ are the atoms that correspond to the atom $l$ in the other supercells. Hence, this method is not suitable for long range ifcs.

A method to avoid periodic boundary conditions and therefore also supercell calculations is the density-functional perturbation theory (DFPT) [39, 40].

The DFPT is based on the Hellmann-Feynman theorem that links the forces to the electron-ion interaction $U_R(r)$ and the energy that originates from the ion-ion interaction $E_N(\{R\}) = -\sum_{i \neq j} = \frac{1}{2\pi\epsilon_0} \frac{Z_I Z_J}{|R_I - R_J|}$:

$$F_{k\alpha} = -\int dr\ n_{\{R\}}(r) \frac{\partial U_{\{R\}}(r)}{\partial R_{k\alpha}} - \frac{\partial E_N(\{R\})}{\partial R_{k\alpha}}. \tag{2.111}$$

Using equation (2.109) an expression for the ifcs can be obtained

$$\Phi_{k\alpha l\beta} = \int dr \frac{\partial n_{\{R\}}(r)}{\partial R_{k\alpha}} \frac{\partial U_{\{R\}}(r)}{\partial R_{l\beta}} + \int dr\ n_R(r) \frac{\partial^2 U_{\{R\}}(r)}{\partial R_{k\alpha} \partial R_{l\beta}} + \frac{\partial^2 E_N(\{R\})}{\partial R_{k\alpha} \partial R_{l\beta}}. \tag{2.112}$$

The derivative of the density can be translated to a derivative of the wave function [40]. Hence, the second order derivative of the energy can be related to the first order derivative of the wave function. In fact it is possible to get also the third order derivative of the total energy from the first order derivative of the wave function. This is stated in the 2n+1 theorem [41]. The derivative of the wave function can be obtained by first-order perturbation theory [42]. The implementation of the DFPT in the ABINIT code package is explained in references [42, 39].

## 2.4 Non equilibrium Green's function formalism (NEGF)

### 2.4.1 Basics

One purpose of the introduction of Green's functions in solid state physics is to solve the physical problem, which is defined by the time independent Schrödinger equation

$$H\psi = E\psi. \tag{2.113}$$

The Green's function G' belonging to the Hamiltonian H is defined by

$$(E - H)G' = \mathrm{I}. \tag{2.114}$$

where I is the identity operator. Since $H$ is hermitian there is a completeness set of eigenfunction $\phi_n$ with corresponding real eigenvalues $\lambda_n$. With this the Green's function in the spectral representation can be obtained by

$$G' = \frac{1}{E-H}\mathrm{I} = \sum_n \frac{1}{E-\lambda_n}|\phi_n><\phi_n| = \sum_n \frac{|\phi_n><\phi_n|}{E-\lambda_n}. \tag{2.115}$$

In real space representation $G'$ can be written by

$$G'(r, r', E) = \sum_n \frac{\phi_n(r)\phi_n^*(r')}{E-\lambda_n}. \tag{2.116}$$

$G'(E, r, r')$ is an analytic function for $E \neq \lambda_n$. For $E = \lambda_n$ $G'(E, r, r')$ has poles, which means the poles of $G'(E, r, r')$ are the eigenvalues of $H$. To evaluate expression (2.116) further, two new Green's function are defined by

$$G^+(r, r', E) \;=\; lim_{\epsilon\to 0^+} G'(r, r', E + i\epsilon) \tag{2.117}$$

and

$$G^-(r, r', E) \;=\; lim_{\epsilon\to 0^+} G'(r, r', E - i\epsilon). \tag{2.118}$$

Using the Dirac identity

$$lim_{\epsilon\to 0^+} = P\frac{1}{x} \pm i\pi\delta(y), \tag{2.119}$$

the Green's functions $G^\pm$ can be rewritten to

$$G^\pm(r, r', E) = P\sum_n \frac{\phi(r)\phi^*(r')}{E-\lambda_n} \mp \pi \sum_n \delta(E-\lambda_n)\phi_n(r)\phi_n^*(r'). \tag{2.120}$$

The integration over $r$ yields for the diagonal elements

$$\int dr G^{\pm}(r,r,E) \equiv \mathrm{Tr}(G^{\pm}(E)) = P\sum_n \frac{1}{E-\lambda_n} \mp i\pi \sum_n \delta(E-\lambda_n). \quad (2.121)$$

The density of states is defined by $n_{el} = \sum_n \delta(E-\lambda_n)$. Thus, the density of states and the Green's function are linked by

$$n_{el} = \mp \frac{1}{\pi} \mathrm{Im}[\mathrm{Tr}(G^{\pm})]. \quad (2.122)$$

### 2.4.2 Finite difference method

A common method to solve differential equations like (2.113) is the finite difference method (FDM). The FDM translates a differential equation in a set of linear equations, which can be solved numerically. The basic idea of the FDM is that the differential equation is solved on a discretized net. In the FDM representation operators become matrices and wave functions become vectors. Here we will introduce the FDM for the example of equation (2.113). The Hamilton operator for a one particle system with a potential $V$ has in real space representation the following form

$$(-\frac{\hbar^2}{2m}\frac{d^2}{dx} + V(x))\phi(x) = E\phi(x). \quad (2.123)$$

To translate this equation in FDM a FDM representation for the squared momentum operator $P^2 = -\frac{\hbar^2}{2m}\frac{d^2}{dx}$ and the potential operator $V$ has to be derived. First the variable for the real space $x$ is discretized, which means the continuous variable $x$ is replaced by an index $i \in \mathbb{N}$. Therefore, the function $\phi(x)$ becomes a vector $\phi(i)$. The operator $V(x)$ becomes a diagonal matrix $V(i,i)$. The representation of $P^2$ is not ambiguous. In this work we use a common representation that can be used if the first derivative does not appear the differential equation. Even though the index $i$ can only take integer values, interstitial points are considered for the derivation of the representation of $P^2$ as sketch in Fig. 2.10. The first derivative at point $i$ is then

$$\phi'(i) = \frac{\phi(i+\frac{1}{2}) - \phi(i-\frac{1}{2})}{a}. \quad (2.124)$$

The second derivative at point $i$

$$\phi''(i) = \frac{\phi'(i+\frac{1}{2}) - \phi'(i-\frac{1}{2})}{a} \quad (2.125)$$

can be expressed using equation (2.124) as

$$\phi''(i) = \frac{\phi(i+1) + \phi(i-1) - 2\phi(i)}{a^2}. \quad (2.126)$$

Hence, $P^2$ in matrix representation has the following form

$$P^2 = \begin{pmatrix} ... & -t & 0 & 0 \\ -t & 2t & -t & 0 \\ 0 & -t & 2t & -t \\ 0 & 0 & -t & ... \end{pmatrix} \tag{2.127}$$

with $t = \frac{\hbar^2}{2ma^2}$. There are two simple ways to include boundary conditions. If the matrix $P^2$ is finite and is cut off at point 1 and point $n$, the wave function at the boundaries is zero $\phi(0) = \phi(n+1) = 0$. If the matrix $P^2$ is finite and is cut off at point 1 and point $n$ and additionally the $P^2(1, N)$ and $P^2(N, 1)$ are set to $-t$ the wave function has periodic boundary conditions $\phi(1) = \phi(n)$. There are also other boundary conditions possible. The slope of $\phi$ at the boundaries can be specified as well as the values of $\phi$ at the boundaries.

In Fig. 2.11 solutions of the one dimensional infinite deep potential well obtained with FDM are shown. The width of the well is $L = 10$nm and the number of points is 20. Hence $a = 0.5nm$. The eigenfunctions that belong to the low energy eigenvalues map the analytic solutions well. With increasing the energy the oscillations of the analytic solutions increase and the numeric solution can not image the analytic solutions anymore. Also the eigenenergies and the analytic eigenvalues agree well for low energy and start to deviate with increasing the energy as shown in Fig. 2.11. The accuracy of the numeric solutions can be estimated by comparing the energy $E$ with the coupling parameter $t$. As a rule of thumb one can say, that the numerical solution obtained with the FDM is accurate as long as $E - V << t$. Nevertheless, for all calculations convergence tests have to be done with respect to the parameter $a$.

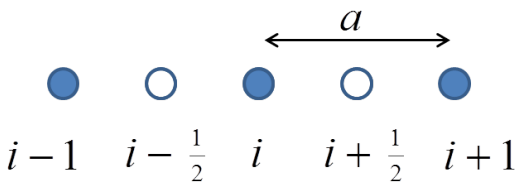


Figure 2.10: Sketch to illustrate the second derivative at point $i$

### 2.4.3 Open boundaries/infinite leads

In the last section it was shown that there are three different possible boundary conditions. The slope of $\phi$ can be given at the boundaries, the value of $\phi$ can be given at the boundary or periodic boundary conditions can be chosen. Since in this work open systems that are not necessarily periodic are considered, additional boundary conditions are needed. The systems under consideration have all a similar form, which is shown in Fig. 2.12. The system consists of two semi infinite leads that are connected to the system described

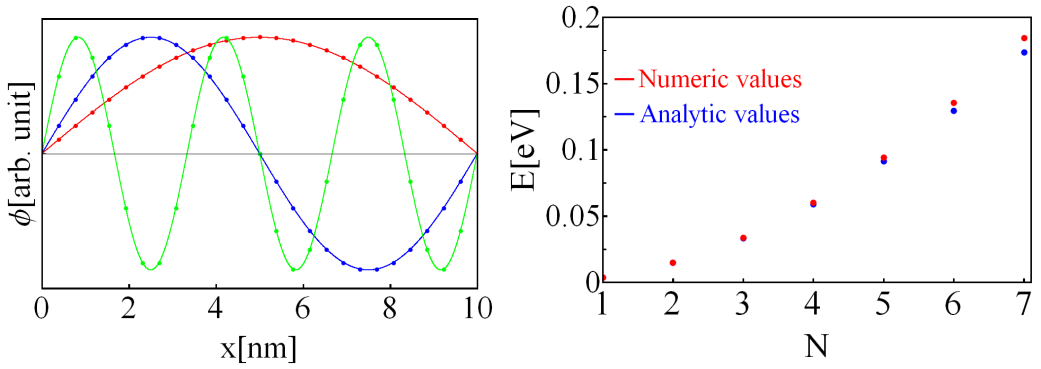


Figure 2.11: Left: Numerical eigensolutions of the infinite high potential well (blue: ground state, red: first exited state, yellow: fifth exited state). Right: Analytic and numerical eigenvalues of the infinite high potential well.

by the Hamiltonian $H$. Since an infinite lead requires in the FDM infinite matrices, which are numerically not manageable, the concept of the so called self energies are introduced. Roughly speaking these self energies simulate these semi infinite leads by injecting or absorbing particles in or from the system in the same way an infinite lead would inject or absorb particles. The advantage is, that the self energies in FDM representation are finite quantities.

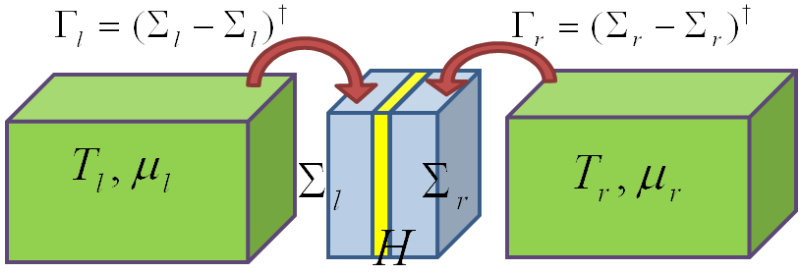


Figure 2.12: Sketch of systems under consideration. Two semi infinite leads (green) are connected to the main region (blue). For each lead a different temperature $T$ and chemical potential $\mu$ can be defined. The effect of the leads on the main region are simulated through self energies $\Sigma$. The $\Gamma$'s are deduced from the $\Sigma$'s and are used in transport calculations.

The self energies for the left and right lead are indicated with $\Sigma_l$ and $\Sigma_r$ respectively. To derive an expression for $\Sigma_{l,r}$ a system that consist of one lead connected to the main region described by $H$ is considered. The overall Green's function can be partitioned in

$$G = \begin{pmatrix} G_l & G_{lH} \\ G_{Hl} & G_H \end{pmatrix} \equiv \begin{pmatrix} E - H_l & \tau_l \\ \tau_l^\dagger & E - H \end{pmatrix}^{-1}, \tag{2.128}$$

where $\tau_l$ is the coupling matrix between the lead and the main region and $H_l$ is the Hamilton operator of the lead. Using

$$\begin{pmatrix} G_l & G_{lH} \\ G_{Hl} & G_H \end{pmatrix} \begin{pmatrix} E - H_l & \tau_l \\ \tau_l^\dagger & E - H \end{pmatrix} = \begin{pmatrix} 1 & 0 \\ 0 & 1 \end{pmatrix} \tag{2.129}$$

leads to four equations from which the following two are used:

$$(E - H)G_{lH} + \tau_l G_H = 0 \tag{2.130}$$

and

$$(E - H_l) + \tau_l^\dagger G_H = 1. \tag{2.131}$$

To obtain the Green's function of the main region connected to a lead

$$G_H = (E - H - \tau_l^\dagger G_l \tau_l)^{-1}, \tag{2.132}$$

where $G_l = (E - H_l)^{-1}$ is the Green's function of the lead. Hence, for the self energy of the lead one obtains

$$\Sigma = \tau_l^\dagger G_l \tau_l. \tag{2.133}$$

One might think that the problem of the infinite matrix representation has not change since the quantity $g_l$ also involves an infinite matrix $H_l$. $H_l$ however should describe an constant infinite lead, which means $H_l$ has a translation symmetry. The Green's function of a infinite or semi infinite system with translation symmetry can be calculated using the decimation technique [43]. The details of the decimation technique will be not described in this work but can be found in the literature [43].

### 2.4.4 Calculation of the transmission function

The purpose of this section is to derive an expression for the transmission function of a system that is connected to two infinite leads, which is described by the Green's function $G$

$$G = (E - H - \Sigma_r + \Sigma_l). \tag{2.134}$$

Before the transmission function is derived a few new quantities are introduced. With these quantities the equation of the current per lead can be

motivated. From the equation of the current per lead the transmission function is deduced. The first quantity that is introduced is a generalized density of states $A$, which is motivated from equation (2.122)

$$A \equiv i(G - G^\dagger). \tag{2.135}$$

By noticing that

$$\begin{aligned} (G^\dagger)^{-1} - G^{-1} &= \Sigma - \Sigma^\dagger, & (2.136)\\ G(G^\dagger)^{-1}G^\dagger - GG^{-1}G^\dagger &= G(\Sigma - \Sigma^\dagger)G^\dagger, & (2.137)\\ i(G - G^\dagger) &= Gi(\Sigma - \Sigma^\dagger)G^\dagger, & (2.138) \end{aligned}$$

the generalized density of states $A$ can be written as

$$A = G\Gamma G^\dagger, \tag{2.139}$$

with $\Sigma = \Sigma_l + \Sigma_r$ and $\Gamma = i(\Sigma - \Sigma^\dagger)$. An interpretation of $\Gamma$ can be found by looking at equation (2.133) and equation (2.135). $\Gamma$ can be expressed as

$$\Gamma_{l,r} = \tau_{l,r}^\dagger A_{l,r} \tau_{l,r}. \tag{2.140}$$

Hence, $\Gamma_{l,r}$ describes the coupling of the density of states in the leads, $A_{l,r}$, to the rest of the system. Besides $A$ and $\Gamma$ a generalized particle density $G^n$ and hole density $G^p$ are introduced, which are defined by

$$G^n = A \cdot f, \tag{2.141}$$

and

$$G^p = A \cdot (1 - f), \tag{2.142}$$

where $f$ is the occupation function of the leads. equation (2.139) can only be used in equilibrium when the occupation functions of both leads are identical. For non equilibrium problems one can use the feature of $A$ that $A$ can be decomposed into $A_l + A_r$ with $A_{l,r} = G\Gamma_{l,r}G^\dagger$. With this also $G^n$ can be decoupled into

$$G^n = A_l f_l + A_r f_r \tag{2.143}$$

which can be rewritten to

$$G^n = G\Sigma^{in}G^\dagger, \tag{2.144}$$

where $\Sigma^{in} = \Sigma_l^{in} + \Sigma_r^{in} = \Gamma_l f_l + \Gamma_r f_r$. $\Sigma^{in}$ is called the inscattering matrix. The inscattering matrix describes the available particles in the lead, which can scatter into the main region. With this a phenomenological explanation for the inscattering can be presented. The inscattering current $j_i^{in}$ from lead $i$ into the main region is proportional to the particles that are available in the lead times the number of states available in the main region. Hence,

$$j_{l,r}^{in} = \frac{1}{h} Tr[\Sigma_{l,r}^{in} A]. \tag{2.145}$$

The explanation of the outscattering current $j^{out}$ is similar. The number of particles that are leaving the main region are proportional to the number of particles available in the main region times the number of states in the lead. Hence,

$$j_{l,r}^{out} = \frac{1}{h} Tr[\Gamma_{l,r} G^n]. \tag{2.146}$$

Therefore, the total current is

$$j_{l,r} = \frac{1}{h}(Tr[\Sigma_{l,r}^{in} A] - Tr[\Gamma_{l,r} G^n]). \tag{2.147}$$

This formula is valid even if scattering is implemented, which is explained in the next section. If no scattering is implemented and the current from one lead to another lead through the main region should be calculated, equation (2.147) can be simplified to

$$\begin{aligned} j_l &= \frac{1}{h} Tr[\Sigma_l^{in} A] - Tr[\Gamma_l G^n] \\ &= \frac{1}{h} Tr[f_l \Gamma_l (A_l + A_r) - \Gamma_l (f_l A_l + f_r A_r)] \\ &= \frac{1}{h} Tr[f_l \Gamma_l A_r - \Gamma_l f_r A_r] \\ &= \frac{1}{h}(f_l - f_r) Tr[\Gamma_l A_r] \\ &= \frac{1}{h}(f_l - f_r) Tr[\Gamma_l G \Gamma_r G^\dagger]. \end{aligned} \tag{2.148}$$

In the same way one can show that

$$j_r = \frac{1}{h}(f_r - f_l)Tr[\Gamma_r G \Gamma_l G^\dagger]. \tag{2.149}$$

Since

$$Tr[\Gamma_r G \Gamma_l G^\dagger] = Tr[\Gamma_r G \Gamma_l G^\dagger], \tag{2.150}$$

the current from the left to the right lead $j_{l\to r}$ and the current from the right to the left lead $j_{r\to l}$ are linked by

$$j_{l\to r} = -j_{r\to l} = \frac{1}{h} t \cdot (f_l - f_r) \tag{2.151}$$

where

$$t = Tr[\Gamma_r G \Gamma_l G^\dagger] \tag{2.152}$$

is the transmission function. Equation (2.151) shows that particle conservation is fulfilled.

### 2.4.5 Incorporation of scattering

In the last section transport from one lead to another lead through the main region was described. In the main region the particles could only be scattered coherently on a static potential. This model will be extended to include incoherent scattering. Although incoherent scattering is mostly inelastic, it can be useful to model incoherent scattering with elastic processes. Therefore, there are two different ways to describe incoherent scattering, elastic and inelastic. In both ways the scattering is described by the so called Büttiker probes. A Büttiker probe is conceptual the same as a lead (see last section). A Büttiker probe simulates the injection or absorption of particles in or from the main region. Büttiker probes are determined by their self energies $\Sigma_s$, inscattering matrices $\Sigma_s^{in}$ and coupling matrices $\Gamma_s$. According to equation (2.145) the total current of the Büttiker probe $i$ can be calculated by

$$j_i = Tr[\Sigma_i^{in} A] - Tr[\Gamma_i G^n]. \tag{2.153}$$

A direct physical meaning of $\Sigma_s$ is given by [28]

$$\Sigma_s = -\frac{i\hbar}{2\tau_s}, \tag{2.154}$$

where $\tau_s$ is the life time of the electrons. In this equation the real part of $\Sigma_s$ is neglected. Equation 2.153 can be used to define the physics of a system by choosing the corresponding $\Sigma_s$ to reproduce the desired scattering rates. $\Sigma_s$ can be energy and space dependent. Another approach to define scattering is to model the scattering process directly. For example the equation for $\Sigma_s^{in}$ and $\Gamma_s$ for a general inelastic process can be written by [28]

$$\Sigma_s^{in} = \int \frac{d(\hbar\omega)}{2\pi} \left( D^{em}(\hbar\omega) \cdot G^n(E + \hbar\omega) + D^{ab}(\hbar\omega) \cdot G^n(E - \hbar\omega) \right) \quad (2.155)$$

and

$$\begin{aligned} \Gamma_s = \int \frac{d(\hbar\omega)}{2\pi} (D^{em}(\hbar\omega)[G^p(E - \hbar\omega) + G^n(E + \hbar\omega)] + \\ D^{ab}(\hbar\omega)[G^n(E - \hbar\omega) + G^p(E + \hbar\omega)]). \end{aligned} \quad (2.156)$$

$D^{em}(\hbar\omega)$ and $D^{ab}(\hbar\omega)$ characterizes the emission and absorption of electrons caused by the scattering process. The imaginary part of $\Sigma_s$ is given through $\Gamma_s$, whereas the real part of $\Sigma_s$ can by calculated by a Hilbert transformation of $\Gamma_s$ [28].

In this work only the model of elastic scattering is used. Elastic scattering means, that the total current for each Büttiker probe has to be zero for all energies. Hence,

$$Tr[\Sigma_i^{in}(E)A(E)] = Tr[\Gamma_i(E)G^n(E)]. \quad (2.157)$$

This condition is stronger than the normal particle conservation. In general if inelastic scattering is present the condition for particle conservation is

$$\int dE\ Tr[\Sigma(E)_i^{in} A(E)] = \int dE\ Tr[\Gamma_i(E)G^n(E)]. \quad (2.158)$$

There are two interpretations of condition (2.157). The first one is that a particle enters a Büttiker probe with energy $E$ and leaves the Büttiker probe at energy $E$ with a different phase and/or direction. This interpretation seldom describes the physics since in most scatter mechanisms a change in phase and/or momentum also involves a change in energy. The second interpretation avoids this problem. The second interpretation is that for each particle that enters a Büttiker probe at energy $E$ another particle from another energy $E'$ is scattered into energy $E$.

As already mentioned, there are two different ways to define the physics of the scattering. If the scattering time is given then the self energies given by equation (2.154). If the concrete scattering mechanism should be modeled

then equations (2.155) and (2.156) are used. Independently which approach is used there are two common ways to calculate the transmission function for the elastic model. In the first approach the condition (2.157) is incorporated in the quantities $\Sigma_s^{in}$ and $\Gamma_s$. In the second approach the condition (2.157) is directly imposed into the calculation of the transmission function. Since the first approach involves nearly all introduced quantities, these quantities are summarized here and already simplified within the elastic model ($D^{em} = D^{ab} = D$) [28]:

$$
\begin{aligned}
G &= (E - H - \Sigma)^{-1} && (2.159)\\
A &= i(G - G^\dagger) && (2.160)\\
\Gamma &= i(\Sigma - \Sigma^\dagger) && (2.161)\\
\Sigma &= \Sigma_l + \Sigma_r + \Sigma_s && (2.162)\\
\Sigma^{in} &= \Sigma_l^{in} + \Sigma_r^{in} + \Sigma_s^{in} && (2.163)\\
\Sigma_{l,r}^{in} &= \Gamma_{l,r} \cdot f_{l,r} && (2.164)\\
\Sigma_s^{in} &= DG^n && (2.165)\\
\Gamma_s &= DA && (2.166)\\
\Sigma_s &= DG && (2.167)\\
G^n &= G\Sigma^{in}G^\dagger. && (2.168)
\end{aligned}
$$

In this model the calculation of the Green's function is determined by

$$G = (E - H - \Sigma_l - \Sigma_r - DG)^{-1}, \tag{2.169}$$

which can be solved within a self consistent calculation. Once the Green's function is determined $G^n$ can be calculated using

$$G^n = G(\Sigma_l^{in} + \Sigma_r^{in} + DG^n)G^\dagger. \tag{2.170}$$

In general this equation has to be solved by using a self consistent calculation. $D$ is for physical problems a diagonal matrix. If furthermore the scattering process is constant in space, which means that $D$ is a constant times the identity matrix, equation (2.170) can be solved analytically for the diagonal elements

$$
\begin{aligned}
G^n &= G(\Sigma_l^{in} + \Sigma_r^{in} + DG^n)G^\dagger, && (2.171)\\
diag[G^n] &= (1 - DGG^*)^{-1} diag[G(\Sigma_l^{in} + \Sigma_r^{in})G^\dagger]. && (2.172)
\end{aligned}
$$

$diag[x]$ is a vector consisting of the diagonal elements of $x$. Since $D$ is diagonal only the diagonal elements of $G^n$ are needed. The definition of the transmission

function $t$ in the elastic scattering model is motivated by equation (2.148). Hence, the transmission function in the elastic model is

$$t = j_l/(f_l - f_r) = j_r/(f_r - f_l). \tag{2.173}$$

For inelastic scattering the definition of a transmission function makes no sense. Using equation (2.147) equation (2.173) can be rewritten to

$$t = tr[\Gamma_l G \Gamma_r G^\dagger] + \frac{1}{f_r - f_l} tr[\Gamma_l^{in} A_s - \Gamma_l G_s^n] \tag{2.174}$$

with

$$A_s = G\Gamma_s G^\dagger \tag{2.175}$$
$$G_s^n = G\Sigma_s^{in} G^\dagger. \tag{2.176}$$

If the scattering process is constant in space equation (2.172) can be used to simplify equation (2.174) to

$$t = tr[\Gamma_l G \Gamma_r G^\dagger] + tr[\Gamma_l G \Gamma_{s_r} G^\dagger] \tag{2.177}$$

with

$$\Gamma_{s_{l,r}} = DdiagM[(1 - DGG^*)^{-1} diag[G\Gamma_{l,r} G^\dagger]]. \tag{2.178}$$

$diagM[x]$ is a diagonal matrix, where the diagonal elements consisting of the elements of vector $x$.

The second approach to calculate the transmission function is the elastic scattering model which is presented now. In this approach the condition of current conservation at each Büttiker probe for each energy is directly imposed on the calculation of the transmission function. Since the Büttiker probes do not conceptually differ from the leads equation (2.151) can be generalized to

$$j_{\alpha\to\beta} = -j_{\beta\to\alpha} = \frac{1}{h} t \cdot (f_\alpha - f_\beta), \tag{2.179}$$

where $j_{\alpha\to\beta}$ is the current from Büttiker probe $\alpha$ to Büttiker probe $\beta$ and $f_{\alpha,\beta}$ are the distribution functions of the Büttiker probes. The total current in Büttiker probe $\alpha$ is therefore

$$j_\alpha = \frac{1}{h} \sum_{k\neq\alpha} t_{\alpha k}(f_\alpha - f_k). \tag{2.180}$$

The index $k$ inhibits all Büttiker probes as well as the two leads. Since in the elastic model $j_\alpha = 0$, an equation for $f_a$ can be derived

$$f_\alpha = \sum_{k \neq \alpha} \frac{t_{\alpha k} f_k}{S_\alpha} \tag{2.181}$$

with

$$S_\alpha = \sum_{k \neq \alpha} t_{\alpha k}. \tag{2.182}$$

Using equations (2.179) and (2.180) the total currents at the leads are

$$j_{(l,r)} = \sum_{k \neq (l,r)} t_{(l,r)k}(f_{(l,r)} - f_k), \tag{2.183}$$

$$j_{(l,r)} = t(f_{(l,r)} - f_{(r,l)}) \tag{2.184}$$

with

$$\begin{aligned} t = \; & t_{lr} + \textstyle\sum_{k \neq (lr)} \frac{t_{lk} t_{kr}}{S_k} + \sum_{k \neq (lr)} \sum_{j \neq (lrk)} \frac{t_{lk} t_{kj} t_{jr}}{S_k S_j} + \\ & \textstyle\sum_{k \neq (lr)} \sum_{j \neq (lrk)} \sum_{i \neq (jlrk)} \frac{t_{lk} t_{kj} t_{ji} t_{ir}}{S_k S_j S_i} + \ldots . \end{aligned} \tag{2.185}$$

The transmission functions $t_{ij}$ can be obtained by applying equation (2.152) to the Büttiker probes to obtain

$$t_{ij} = Tr[\Gamma_i G \Gamma_j G^\dagger]. \tag{2.186}$$

Equation 2.185 divides the transmission function $t$ in orders of scattering events. The first term $t_{lr}$ can be seen as the transmission probability that a particle passes the main region without being scattered, which must not be mistaken with the coherent case when scattering is absent. The second term $\sum_{k \neq (lr)} \frac{t_{lk} t_{kr}}{S_k}$ then is the probability that a particle is scattered once and so on. Fig. 2.13 shows the transmission function of a 1 dimensional electronic system with a length of $10nm$. The scattering strength $D$ is constant in space and proportional to the square root of the energy $D(E) \propto \sqrt{E}$, which leads to a nearly constant $\Sigma_s$ and therefore to a nearly constant scattering time $\tau$. The proportional factor in $D(E)$ is $0.02eV^{\frac{3}{2}}$ and the mass of the electron is $m_e = m_0$. Fig. 2.13 left shows the transmission function obtained with equation (2.177) (blue) and the transmission functions obtained with equation (2.185), at which the sum is taken to the order $n$ with $n = 0$ (violet), $n \leq 4$ (yellow) and $n \leq 10$ (green). For $n \leq \infty$ the transmission function obtained with equation

(2.186) converges against the transmission function obtained with equation 2.177. How fast the sum in equation 2.186 converges depends mainly on the length of the system, the scattering strength, and the energy. In Fig. 2.13 right the transmission probability against the scattering order for two different energies are shown. At $60meV$ the probability that an electron is scattered three times before it passes the main region is the most likely case. With increasing the number of scattering events the probability decreases rapidly. For lower energies the probability is shifted towards higher scattering orders. The physical interpretation of this behavior is simple. Since the scattering strength is chosen such that a constant scattering time is achieved, the electrons with high energies have a higher velocity and hence a higher mean free path, which leads to less scattering events per unit length compared to the low energy electrons.

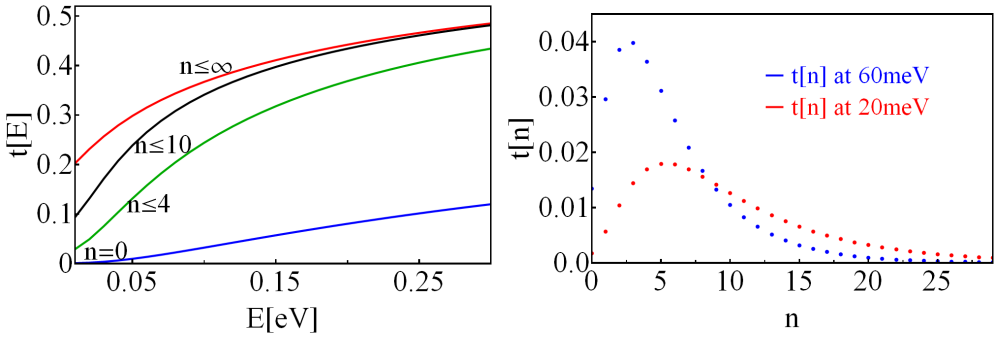


Figure 2.13: Left: Transmission function with several scattering orders $n$ included. Right: transmission probability vs scattering order for two different energies.

### 2.4.6 Combining different scattering mechanisms

Considering a system which is determined by different scattering mechanisms $i \in 1, 2, 3....$ Therefore, for each scattering mechanism a transmission function can be defined $t_1, t_2, t_3....$ If there is no fixed phased relationship between the scatters, the transmission function can be combined classically. The classical combination of two scatterers can be obtained by summing up over all paths a particle can travel to pass both scatterers.

$$\begin{aligned} t &= t_1 t_2 + t_1 t_2 (1-t_1)(1-t_2) + t_1 t_2 (1-t_1)(1-t_2)^2 + \dots \\ &= \frac{t_1 t_2}{t_1 + t_2 - t_1 t_2} \qquad (2.187) \\ \frac{1}{t} &= \frac{1}{t_1} + \frac{1}{t_2} - 1 \qquad (2.188) \end{aligned}$$

The transmission function for $n$ scatters can be obtained by using (2.188) recursively to obtain

$$\frac{1}{t} = \frac{1}{t_1} + \frac{1}{t_2} + \frac{1}{t_3} + \ldots - (n-1). \tag{2.189}$$

Fig. 2.14 left shows the transmission function of a single barrier $t_b$ and the transmission function of elastic scatterers $t_s$. Fig. 2.14 right shows the transmission function of elastic scatters in series with a single barrier $t_{bs}$ and the combined transmission function using equation (2.189). Fig. 2.14 shows that equation (2.189) is a good approximation to combine different scattering mechanisms if phase braking scattering in the system is strong enough.

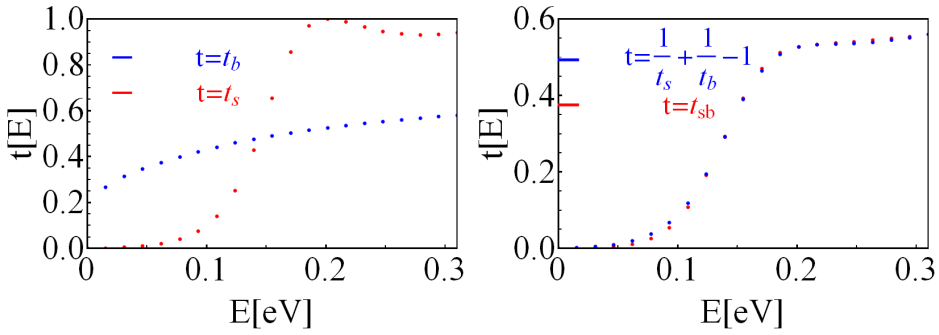


Figure 2.14: Left: Transmission function of a single barrier $t_b$ and the transmission function of elastic scatterers $t_s$. Right: Transmission function of elastic scatters in series with a single barrier $t_{bs}$ and the combined transmission function using equation (2.189)

.

### 2.4.7 Atomistic Green's function method

The atomistic Green's function method (AGF) is in principle the same method as the NEGF. Therefore, the equations obtained for the NEGF in the chapters 2.4.1-2.4.6 also hold for the AGF with the exception of some minor differences, which will be discussed later in this section. There is just one conceptual difference between both methods. In the NEGF the underlying physics are described by differential equation like the Schrödinger equation (2.113). The differential equation is then transformed to a system of linear equations using the FDM. However in the AGF the underlying physics are directly described by a system of linear equations, which means that there is no need for an additional transformation. The NEGF is usually employed to calculate electronic properties, whereas the AGF is used to calculate phononic properties from a classical approach. The equations derived in the chapters 2.4.1-2.4.6 describe the physics of an electronic system, but if a variable transformation from $E$ in the electronic system to the variable $\omega^2$ is used, these equations can also

be used for a phononic system. This leads to a change in the equation for the density of states. To get the correct density of states for the phononic system equation (2.121) is considered and $E$ is substituted by $\omega^2$

$$\mathrm{Tr}(G(E)^{\pm}) = P\sum_n \frac{1}{E-\lambda_n} \mp \pi \sum_n \delta(\omega^2 - \lambda_n). \tag{2.190}$$

For $\lambda_n > 0$ and $\omega > 0$ this can be rewritten to

$$\mathrm{Tr}(G(E)) = P\sum_n \frac{1}{E-\lambda_n} \mp i\pi \sum_n \frac{1}{2\omega}\delta(\omega - \sqrt{\lambda_n}), \tag{2.191}$$

which leads to a phonon density of states $n_{ph}$ of

$$n_{ph}(\omega) = \pm\frac{2\omega}{\pi}\mathrm{Im}[\mathrm{Tr}G^{\mp}]. \tag{2.192}$$

Also the equation that links the self energy with the life time (2.154) changes for the phonon calculation to [44]

$$\Sigma_{s_{ph}} = -\frac{i2\omega}{\tau_s}. \tag{2.193}$$

### 2.4.8 AGF method with periodic boundary conditions in two dimensions

In this section a detailed description of the AGF method with periodic boundary conditions in the two directions perpendicular to the transport direction is given. In the following the system shown in Fig.2.12 is considered. It is assumed that the system is periodic perpendicular to the transport direction. The system can be divided into layers of atoms that are perpendicular to the transport directions. Hence, it is possible to distinguish between interlayer and intralayer interactions. Since the system is periodic perpendicular to the transport direction the single layers inhibits also the same periodicity. Consequently, a Fourier transformation of the interlayer and intralayer interactions perpendicular to the transport direction can be performed. The periodicity in-plane is described by a 2-dimensional lattice with the lattice vectors $\vec{R}^p$. The Fourier transform of the interlayer and intralayer interactions are given by

$$H_g(\vec{q_p}) = \sum_{\vec{R}_p} \widetilde{H_g}(\vec{R}_p)e^{-i\vec{q}_p\vec{R}_p} \text{ (intralayer)}, \tag{2.194}$$

$$T_{g\bar{g}}(\vec{q_p}) = \sum_{\vec{R}_o} \widetilde{H_{g\bar{g}}}(\vec{R}_o)e^{-i\vec{q}_p\vec{R}_o} \text{ (interlayer)}. \tag{2.195}$$

$\vec{R}_o$ are the vectors that connect cells of layers $g$ and $\bar{g}$. $\vec{q}_p$ is a 2-dimensional vector that belongs to the 2-dimensional Brillouin zone of the lattice $\vec{R}^p$. $\widetilde{H_g}$ is the Hamiltonian of layer $g$ and consists of the ifcs that describe the interactions between atoms in the layer. $\widetilde{H_{g\bar{g}}}$ consists of the ifcs that describe the interactions between the atoms of layer $g$ and $\bar{g}$.

The overall matrix describing the system has then the form

$$H(\vec{q}_p) = \begin{pmatrix} ... & T_{g-1,g} & 0 & 0 \\ T_{g,g-1} & H_g & T_{g,g+1} & 0 \\ 0 & T_{g+1,g} & H_{g+1} & T_{g+1,g+2} \\ 0 & 0 & T_{g+2,g+1} & ... \end{pmatrix}. \tag{2.196}$$

$H_g$ is the Fourier transformed intralayer interaction of layer g. $T_{g,g+1}$ is the Fourier transformed interlayer interaction of layer g with g+1. Of course it is also possible to take more than one layer interactions into account. The matrix in equation (2.196) is infinite, but can be reduced to a finite matrix by using the concept of self energies $\Sigma_{R,L}(\vec{q}_p)$, which is explained in section (2.4.3). The Green's function of the system is then

$$G(\omega, \vec{q}_p) = (\omega^2 I - H(\vec{q}_p) - \Sigma_L(\vec{q}_p) - \Sigma_R(\vec{q}_p))^{-1}. \tag{2.197}$$

By using equation (2.152) the transmission function at $\vec{q}_p$ is given by

$$t(\omega, q_p) = \mathrm{Tr}[\Gamma_L(\vec{q}_p) G(\vec{q}_p) \Gamma_R(\vec{q}_p) G^\dagger(\vec{q}_p)]. \tag{2.198}$$

The average transmission function per unit cell is given by an integral over the 2-dimensional Brillouin zone

$$t(\omega) = \frac{1}{(2\pi)^2} \int_{BZ} t(\omega, q_p) d\vec{q}_p, \tag{2.199}$$

$$t(\omega) = \frac{1}{A} \frac{1}{\sum_{\vec{q}_p}} \sum_{\vec{q}_p} t(\omega, q_p), \tag{2.200}$$

where $A$ is the cross area of the unit cell.

## 2.5 Grain boundary model for electronic transport

In this chapter a model is developed that can describe electronic transport in nanograined materials. The model is based on the Landauer theory, which means that all scattering mechanisms are described in terms of transmission functions. To describe the electronic structure only one band with parabolic dispersion relation is considered. The scattering between the grains is described either by a step like transmission function or by a transmission function of a double Schottky barrier. The scattering in the grains are taken into account by a phenomenological power law.

### 2.5.1 Modeling of electrostatic barriers

The model of the grain boundary in this work is based on the model established by Seto [45]. A schematic sketch of the band structure in real space is shown in Fig. 2.15. The grains are characterized by their length $l_g$, the length of the interface region $l_i$, the density of the surface states $N_T$, the energy levels of the trapping states $E_T$, donor concentration $N_D$, and the energy levels of the donors $E_D$.

The basic idea of the model is, that the electrons in the donor states pass over into the deep surface states, which arise in the grain boundary. This leads to a negative charge accumulation in the grain boundaries and a positive charge accumulation adjacent to the grain boundaries. The resulting space charge distribution then creates a so called double Schottky barrier. In the following the steps are described to get a quantitative description of the double Schottky barrier.

First $l_g$ , $l_i$, $N_T$ and $N_D$ have to be chosen. Then two cases can occur. In the first case, $l_g \cdot N_D \leq l_i \cdot N_T$, all donor states in the grains are empty and all electrons are trapped in the grain boundary. The total negative space charge density in the boundary region $n_i$ is then $\frac{N_D \cdot l_g}{l_i}$. The positive space charge density in the rest of the grain in this case is $N_D$. In the second case, $l_g \cdot N_D > l_i \cdot N_T$, the negative space charge density in the boundary region is $N_T$. The positive space charge density is $N_D$ and the length of the positive space charge region, which is called screening length $l_{scr}$, is chosen in such a way, that the total charge in the grain is zero: $l_{scr} = \frac{l_i \cdot N_T}{N_D}$. Once the space charge density $n(x)$ is obtained, the Poisson equation can be used to get the potential profile $V(x)$

$$\nabla(\epsilon_r(x)\nabla V(x)) = \frac{e \cdot n(x)}{\epsilon_0}. \tag{2.201}$$

$\epsilon_r(x)$ is the dielectric constant, which is assumed to be constant throughout the whole grain. In Fig. 2.16 the space charge distribution and the resulting double Schottky barrier is shown. The length of the interface is 0.5 nm. The density of the surface states is $1 \cdot 10^{20}\text{cm}^{-3}$. The donor concentration is $1 \cdot 10^{19}\text{cm}^{-3}$. Double Schottky barriers for different donor concentrations are shown in Fig.

2.16. The height and the width of the barriers decrease strongly with increasing the donor concentration. Fig. 2.17 shows the barrier height for different doping concentrations. For low doping concentrations all electrons are trapped in the grain interface and with increasing the doping concentration the barrier height increases linearly until all trapping states are full. Increasing the doping concentration further the barrier height decreases, because the screening of the potential increases with higher doping concentrations.

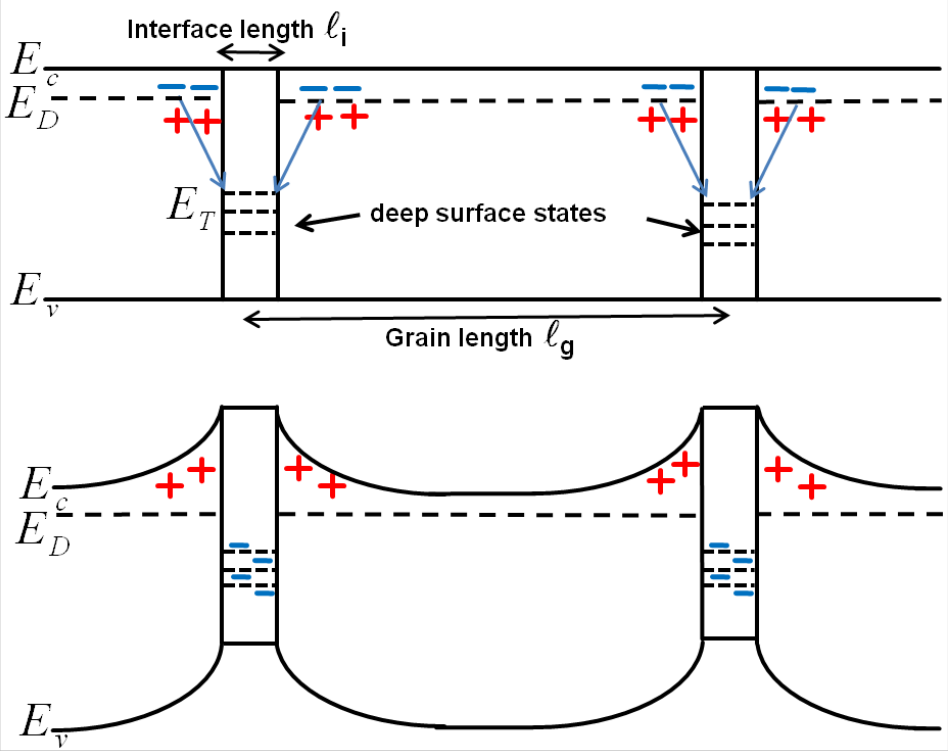


Figure 2.15: Schematic band diagram in real space before (top) and after (bottom) the generation of the double Schottky barrier. $E_c$ is the energy at the bottom of the conduction band, $E_D$ is the donor level, $E_T$ is the energy of the trapping states and $E_v$ is the top of the valence band. (reference E3)

### 2.5.2 Determination of the chemical potential

A common way to link the chemical potential to a given doping concentration $n$ and temperature $T$ in a parabolic one band model is given by [46, 15, 14]

$$n = \frac{4}{\sqrt{\pi}} \left( \frac{2\pi m k_b}{h^2} \right)^{(3/2)} \int_0^\infty \sqrt{E} f(E, T, \mu). \tag{2.202}$$

In this equation only the doping concentration $n$ appears, but for the grain boundary model a link between the donor concentration $N_D$ and the chemical

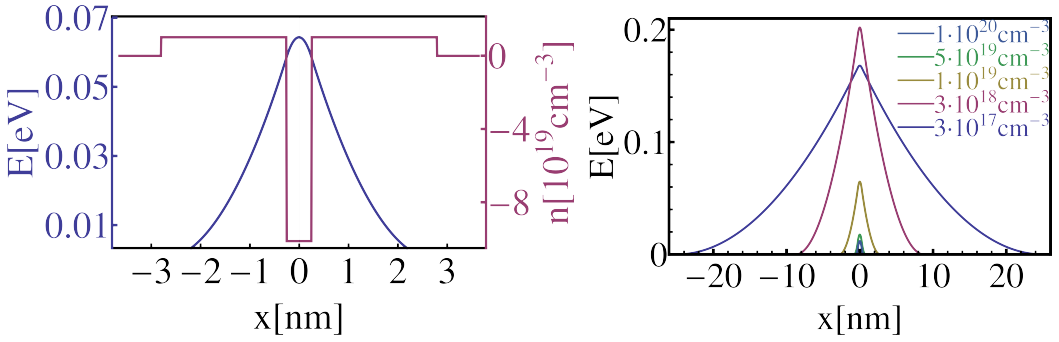


Figure 2.16: Left: Space charge distribution (red) and the corresponding potential profile (blue) around the interface. Right: double Schottky barrier for different donor concentrations. (reference E3)

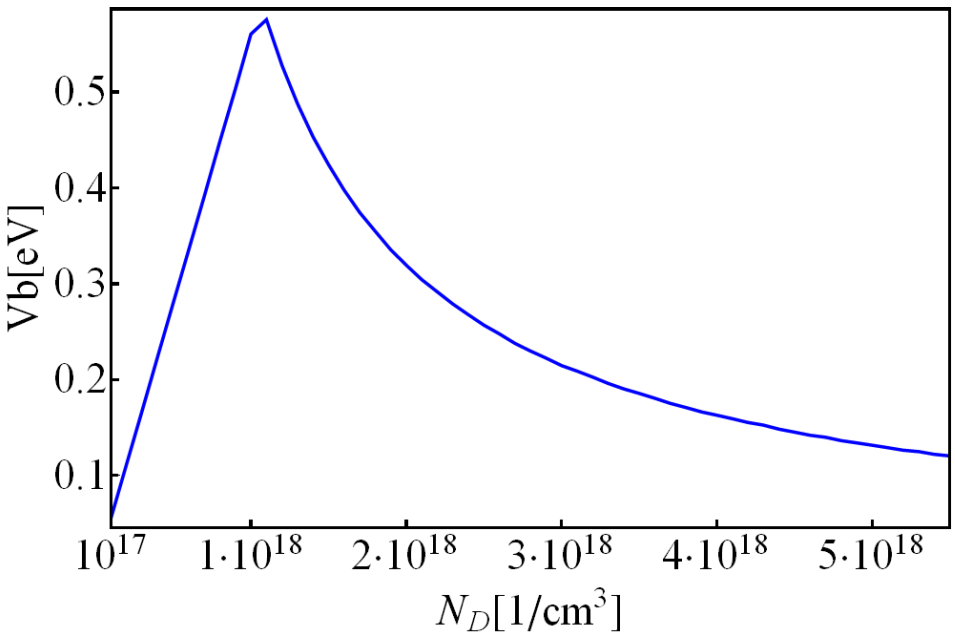


Figure 2.17: Barrier height vs doping concentration for a double Schottky barrier.

potential $\mu$ is needed. Thus a more sophisticated model is employed, which is presented in the following.

For the determination of the chemical potential three kinds of states are considered. The deepest states are in the boundary. There are $N_T \cdot l_i$ total states per grain of this kind at energy $E_T$. The energetic next higher states are the donor states. There are $N_D \cdot l_g$ total donor states per grain at energy $E_D$. For the remaining states the density of states of a single band with a parabolic dispersion is chosen. The energy scale is chosen such, that the bottom of the band is at energy 0. The value of the chemical potential is determined at a given temperature T by imposing charge neutrality. So the chemical potential ensures that the number of ionized donors equals the numbers of electrons trapped in the boundary region plus the number of electrons in the conduction band. Thus, the chemical potential can be obtained by solving

$$\int \frac{(2 \cdot m_{eff})^{3/2}}{2 \cdot \pi^2 \cdot \hbar^3} \sqrt{E} \cdot f(E, \mu, T) dE + l_i \cdot N_T \cdot f(E_T, \mu, T) = N_D \cdot l_g \cdot (1 - f(E_D, \mu, T)). \tag{2.203}$$

Fig. 2.18 left shows the dependence of the chemical potential on the donor concentration for three different temperatures. For low donor concentrations all electrons are trapped. Therefore, the chemical potential is located around the energy of the trapping states $E_T = -0.5$ eV. When the donor concentration reaches a value where all trapping states are filled the chemical potential jumps to the binding energy of the donors $E_D = -0.02$ eV. Further increase of the donor concentration leads to a moderate increase of the chemical potential. For higher temperatures this behavior is smoother. Fig. 2.18 right shows the dependence of the chemical potential on the temperature for two different doping concentrations. For high doping concentrations the chemical potential increases with increasing temperature, whereas for low doping concentrations the chemical potential decreases with increasing the temperature.

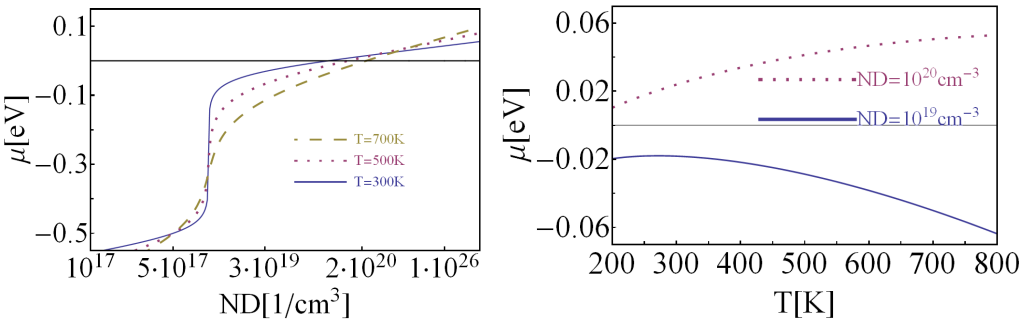


Figure 2.18: Left: Chemical potential $\mu$ vs doping concentration $N_D$ for different temperatures $T$. Right: Chemical potential $\mu$ vs temperature $T$ for different doping concentrations $N_D$.

### 2.5.3 Modeling the transport from grain to sample

In this section the modeling of the electron transport is described. There are several transmission functions in this section. Each transmission function describes a different scattering mechanism and/or a different length scale of transport. Fig. 2.19 shows the evolution of the different transmission functions from functions that describe scattering on the nanoscale $t_{bar}/t_{Bulk}$ to the overall macroscopic transmission function $t_{Solid}$.

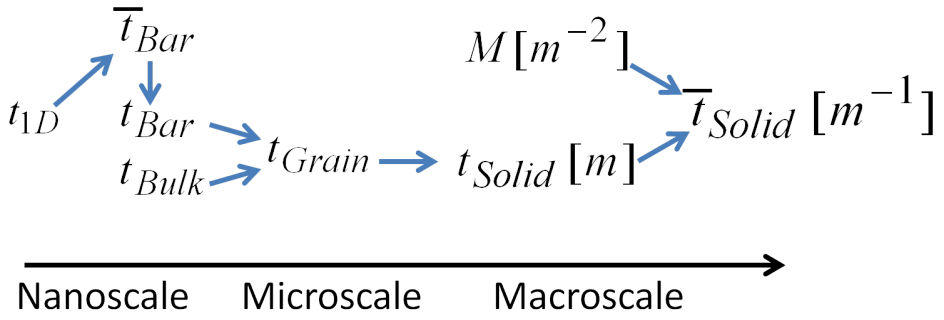


Figure 2.19: Flowchart of the evolution and composition of the different transmission functions. $t_{1D}(k_z)$ is the average transmission probability across the barrier as a function of the momentum in transport direction. $t_{Bar}(E)$ is the average transmission probability across the barrier as a function of the energy. $t_{Bulk}(E)$ is the average transmission probability through a bulk system. $t_{Grain}(E)$ is the average transmission probability through one grain. $t_{Solid}(E)$ is the average transmission probability through a macroscopic sample.

The number of modes $M(E)$ can be obtained from equation (2.30). Since only one band is considered the number of modes per $k_p$ is 1. Hence,

$$M(E) = \sum_{k_p} = \frac{L_x L_y}{(2\pi)^2} \int_0^{k_p = \sqrt{\frac{2m_{eff}E}{\hbar^2}}} 2\pi k_p dk_p = \frac{L_x L_y}{2\pi\hbar^2} m_{eff} E. \tag{2.204}$$

In this model it is assumed that the transmission probability through the barrier depends only on the energy that is related to the momentum in transport direction $k_z$, which in this case is the z direction. Therefore, the total transmission function of the barrier $\overline{t_{Bar}}$ can be obtained by using equation (2.28)

$$\overline{t_{Bar}} = \sum_{k_p} t_{1D}(E - \frac{\hbar^2 k_p^2}{2m_{eff}}) \tag{2.205}$$

$$= \frac{L_x L_y}{(2\pi)^2} \int_0^{k_p=\sqrt{\frac{2m_{eff}E}{\hbar^2}}} 2\pi k_p \cdot t_{1D}(E - \frac{\hbar^2 k_p^2}{2m_{eff}}) dk_p. \tag{2.206}$$

where $t_{1D}(\frac{\hbar^2 k_z^2}{2m_{eff}}))$ is the probability that an electron with momentum $k_z$ passes the barrier. Making the substitution $x = \sqrt{1 - \frac{k^2}{2mE}}$ equation (2.206) can be simplified to

$$\overline{t_{Bar}} = \frac{L_x L_y}{2\pi\hbar^2} m_{eff} E \frac{1}{2} \int_0^1 t_{1D}(E \cdot x^2) dx. \tag{2.207}$$

Comparing equation (2.207) with (2.204) and using equation (2.29) the average transmission function of the barrier $t_{Bar}$ is given by

$$t_{Bar} = \frac{1}{2} \int_0^1 t_{1D}(E \cdot x^2) dx. \tag{2.208}$$

At this point it is worth to stress the differences between the functions $t_{Bar}$ and $t_{1D}$. $t_{Bar}$ is the average transmission probability of an electron as a function of the total energy of the electron, whereas $t_{1D}$ is the transmission probability as a function of $k_z$. According to references [28, 35] different scattering mechanism of electrons in a bulk material can be described by transmission functions of the form

$$t_{Bulk} = \frac{\lambda}{l_z + \lambda}, \tag{2.209}$$

where $l_z$ is the length in transport direction and

$$\lambda = \lambda_0 (\frac{E}{k_b T})^r. \tag{2.210}$$

$r$ specifies the kind of scattering mechanism. To overcome a grain an electron has to travel through the whole grain, which is assumed to be bulk like, and has to overcome the barrier between two grains. Hence, the transmission function for one grain $t_{Grain}$ can be obtained by combining the transmission function of one barrier and the transmission of the bulk. The length $l_z$ in equation 2.208 is then the length of the grain $l_g$. The combination of several scattering

mechanisms can be done by employing equation (2.189). The transmission function for one grain $t_{Grain}$ is then

$$t_{Grain} = \frac{1}{\frac{1}{t_{Bar}} + \frac{1}{t_{Bulk}} - 1}. \tag{2.211}$$

If the solid consist of $n$ grains in transport direction the transmission function for the solid $t_{solid}$ can be obtained, by using again equation (2.189)

$$t_{Solid} = \frac{1}{n} \frac{t_{Grain}}{1 - t_{Grain} + \frac{t_{Grain}}{n}}. \tag{2.212}$$

If $L_z$ is the length of the solid in transport direction and $l_g$ is the length of the grains then the number of grains is $n = \frac{L_z}{l_g}$. Therefore, equation (2.213) can be rewritten to

$$t_{Solid} = \frac{lg}{L_z} \frac{t_{Grain}}{1 - t_{Grain} + \frac{t_{Grain} l_g}{L_z}}. \tag{2.213}$$

In this equation the term $\frac{t_{Grain} l_g}{L}$ describes the contact resistance. For $t_{Grain} < 1$ and $l_g << L_z$ this term can be neglected. The total transmission function $\overline{t_{Solid}}$ can be obtained by

$$\overline{t_{Solid}} = t_{Solid} \cdot M. \tag{2.214}$$

The overall electric parameters can be obtained by using the total transmission function $\overline{t_{Solid}}$ in equations (2.38) and (2.39).

# 3 Material Systems

In this chapter the epitaxial structures of the materials investigated in this work are discussed. These materials are zinc oxide (ZnO), zinc sulfide (ZnS), and silicon (Si). A comprehensive review of ZnO can be found in reference [20].

## 3.1 Zinc Oxide (ZnO)

ZnO is a II-VI semiconductor. The main interest in ZnO results from its prospects in optoelectronic devices due to a direct band gap of 3.3 eV at room temperature. In principle ZnO can occur in three different structures, which are wurtzite-, zincblende- and rocksalt structure. Under normal conditions ZnO has wurtzite structure. Zincblende structure can be observed, if ZnO is grown on cubic substrates[47], whereas the rocksalt structure occurs only at high pressure above 8GPa [48]. A scheme of the three different structures is shown in Fig. 3.20.

The lattice constants and structural parameters of these different structures are presented in table 3.1. The results obtained in this work agree with the results obtain in reference [49], which is not surprising since the authors in reference [49] use the same method and similar numerical parameters.

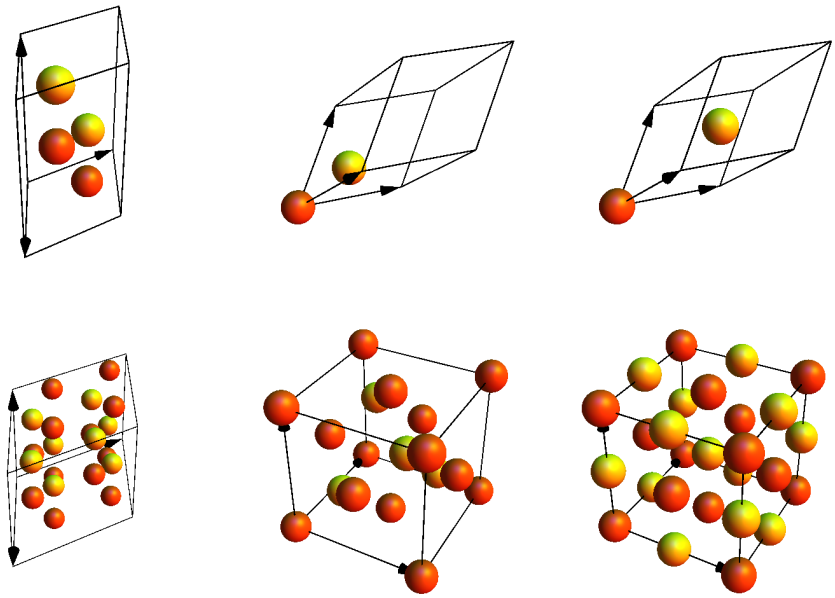

Figure 3.20: Top row: Primitive unit cell. Bottom row: Supercell structure. Left: Wurtzite structure for ZnO and ZnS. Middle: Zincblende structure ZnO and ZnS. Right: Rocksalt structure ZnO and ZnS.

| | a(Å) | c(Å) | c/a | u | V(Å$^3$) |
|---|---|---|---|---|---|
| ZnO Wurtzite | | | | | |
| Theo.* | 3.198 | 5.167 | 1.615 | 0.379 | 22.882 |
| Theo.[49] | 3.198 | 5.167 | 1.615 | 0.379 | 22.882 |
| Theo.[50] | 3.290 | 5.241 | 1.593 | 0.3856 | 24.570 |
| Theo.[51] | 3.199 | 5.163 | 1.6138 | 0.381 | 22.874 |
| Exp.[48] | 3.2496(6) | 5.2042(20) | 1.6018(7) | 0.3819(1) | 23.796(11) |
| Exp.[52] | 3.2498(3) | 5.2066(3) | 1.6021(3) | 0.3832(2) | 23.810(6) |
| ZnO Zincblende | | | | | |
| Theo.[49] | 4.504 | - | - | - | 22.841 |
| Theo.[50] | 4.614 | - | - | - | 24.551 |
| Theo.[51] | 4.508 | - | - | - | 22.914 |
| Exp.[53] | 4.62 | - | - | - | 24.65 |
| ZnO Rock Salt | | | | | |
| Theo.[49] | 4.225 | - | - | - | 18.856 |
| Theo.[50] | 4.294 | - | - | - | 19.799 |
| Theo.[51] | 4.229 | - | - | - | 18.904 |
| Exp.[48] | 4.271(2) | - | - | - | 19.484(11) |
| Exp.[52] | 4.283(1) | - | - | - | 19.60(6) |

Table 3.1: Lattice constants of ZnO: experimental and theoretical values. $*$ indicates own results.

In wurtzite structure ZnO has 4 atoms in the primitive unit cell. This means the phonon dispersion consists of 12 modes. At the Brillouin-zone center these 12 split up into $2A_1+2B_1+2E_1+2E_2$ modes. The $E_1$ and $E_2$ modes are double degenerated. The three acoustic modes are one of the $E_1$(double degenerated) modes and one of the $A_1$ modes. Since the 2 $B_1$ modes are Raman inactive, there are only 7 Raman modes left. These modes are $A_1+E_1+2E_2$. Without LO-TO splitting there would be 4 different frequencies in the Raman spectra of wurtzite ZnO, but since the $A_1$ and the $E_1$ splits at the $\Gamma$ point, there are 6 frequencies in a Raman spectra of ZnO wurtzite. The phonon frequencies at the $\Gamma$ point are shown in table 3.2.

## 3.2 Zinc Sulfide (ZnS)

Besides ZnO, ZnS is also an interesting semiconductor that belongs to II-VI group. ZnS has a direct band gap of 3.8eV and is a promising material for applications in electroluminescent devices, infrared windows, optoelectronic device sensors, and lasers [54, 55]. Like ZnO, ZnS can in principle occur in

| Mode | $\omega_{Theo}(cm^{-1})$ | $\omega_{Exp}(cm^{-1})$ |
|---|---|---|
| $E_2^{low}$ | 91 | 100 |
| $B_1^{low}$ | 261 | - |
| $A_1^{TO}$ | 391 | 380 |
| $E_1^{TO}$ | 409 | 410 |
| $E_2^{high}$ | 440 | 438 |
| $B_1^{high}$ | 552 | - |
| $A_1^{LO}$ | 560 | 584 |
| $E_1^{LO}$ | 556 | 595 |

Table 3.2: Phonon frequencies of wurtzite ZnO at the Γ point. Values are taken from reference [49].

| | a(Å) | c(Å) | c/a | u | V(Å$^3$) |
|---|---|---|---|---|---|
| | | | ZnS Wurtzite | | |
| Theo.* | 3.755 | 6.168 | 1.64 | 0.374 | 37.598 |
| Theo.[57] | 3.81 | 6.2484 | 1.64 | - | 39.2753 |
| Exp.[58] | 3.8227 | 6.2607 | 1.6378 | 0.3748 | 39.6154 |
| | | | ZnS Zincblende | | |
| Theo.* | 5.32 | | | | 37.642 |
| Theo.[57] | 5.4 | | | | 39.366 |
| Exp.[59] | 5.4109 | | | | 39.6049 |

Table 3.3: Lattice constants of ZnS: experimental and theoretical values. $*$ indicates own results.

three different structures, which are the wurtzite structure, the zincblende structure, and the rocksalt structure. In nature ZnS has mostly zincblende structure, but can also be found in wurtzite structure, whereas the rocksalt structure only occur at a pressure above 15 GPa [56]. A scheme of the three different structures is shown in Fig. 3.20.

The lattice constants and structural parameters of ZnS in wurtzite and zincblende structure are presented in table 3.3. The lattice constants obtained in this work are slightly smaller than the values reported by other groups, which is a consequence of the LDA approximation used to derive the results presented in this work.

The Raman active modes for ZnS in wurtzite and zincblende structure are shown in table 3.4.

## 3.3 Si

Silicon is a common material. It is widely used in industry for electronics and solar cells [60]. Silicon is also used together with germanium in silicon

| Mode | $\omega_{Theo}(cm^{-1})$ | $\omega_{Calc}(cm^{-1})$ |
|---|---|---|
| Wurtzite structure | | |
| $E_2^{low}$ | 72 | 76 |
| $A_1^{TO}$ | 275 | 287 |
| $E_1^{TO}$ | 279 | 288 |
| $E_2^{high}$ | 285 | 296 |
| $A_1^{LO}$ | 353 | 347 |
| $E_1^{LO}$ | 353 | 350 |
| Zincblende structure | | |
| $T_2^{TO}$ | 278 | 277 |
| $T_2^{LO}$ | 351 | 340 |

Table 3.4: Raman active modes of wurtzite ZnS and zincblende ZnS. Values are taken from [57].

germanium based thermoelectric generators [61]. Despite silicon exhibits good electric properties for thermoelectric, the figure of merit for pure silicon devices is rather low, because of the high lattice conductivity of silicon, which is approximately $156 W/mK$ at 300K [62]. To avoid the expensive and rare germanium there are different approaches under investigation. One approach is to go from bulk silicon to nanostructures like silicon nanowires [63]. Another approach is to create superlattices of different silicon isotopes. There are three stable isotopes of silicon $^{28}$Si, $^{29}$Si and $^{30}$Si. Silicon crystallizes in diamond structure with a lattice constant of 5.429Å[64, 65]. The Raman mode of silicon is $520 cm^{-1}$[66]. Since there is only one type of atom, no LO-TO splitting can be observed. Fig. 3.21 shows the structure of Si in a primitive cell (left) and in the common crystallographic cell (right).

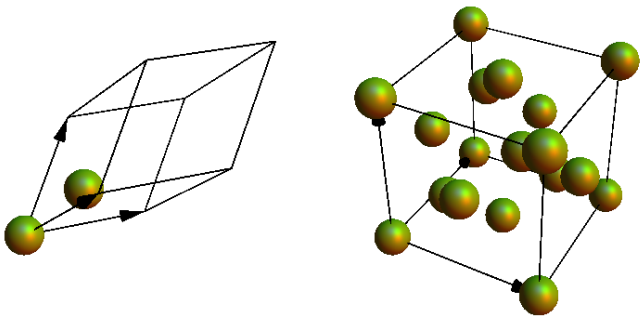

Figure 3.21: Left: primitive cell of Si. Right: Si in the common crystallographic cell.

# 4 Results and Discussion

In this chapter three different problems are investigated. In the first section of this chapter the atomistic Green's function (AGF) method is employed to calculate coherent phonon scattering in ZnO/ZnS based systems. The focus in this section is set on ZnO/ZnS interfaces and how these interfaces affects the thermal conductance. Furthermore, coherent phonon scattering in $ZnO_xS_{1-x}$ alloys is investigated by calculating coherent phonon scattering in ZnO on sulfur impurities and in ZnS on oxygen impurities.

In the second section of this chapter the electronic properties of nanograined semiconductors are investigated. Especially the effect of energy filtering on the thermoelectric efficiency is considered and under which conditions the energy filtering can enhance the thermoelectric efficiency.

In the third section the AGF method is used to calculate the conductance of Si isotope superlattices.

## 4.1 Phonon scattering on ZnO/ZnS interfaces

In this section the phonon structures of ZnO and ZnS are investigated as well as the phonon transport properties of these structures. The thermal lattice conductance is obtained by using equation (2.42). The transmission function is calculated within the AGF method as described in section 2.4.8. The interface resistance is calculated using the so-called diffuse mismatch model (DMM)[67]. In principle, the AGF method is capable of calculating the correct interface conductance, but to do so the interatomic force constants of the correct interface has to be known. Since the lattice parameters of ZnO and ZnS show a huge mismatch, see table 3.1 and table. 3.3, the corresponding DFT calculations would require a huge supercell with hundreds of atoms. The calculation of the ifcs of such big supercells takes several months on hundreds of cores, which is much higher than the available computation power for this project . Hence, the DMM is employed to estimate the interface resistance. In the DMM phonons that hit the interface between material $a$ and material $b$ undergo a scattering event. During this scattering event the phonons lose memory of their original state and are either scattered in material $a$ or material $b$. The corresponding probability is proportional to the transmission function of the bulk materials. The transmission function is normalized such that for an interface between the same material the overall transmission is 1/2 of the bulk transmission. The corresponding interface transmission $t_{ab}$ is given by

$$t_{ab}(\omega) = \frac{t_a(\omega)t_b(\omega)}{t_a(\omega) + t_b(\omega)}. \tag{4.215}$$

$t_a(\omega)$ and $t_b(\omega)$ are the bulk transmission functions. A derivative of equation (4.215) is given in Appendix B. The ifcs are obtained for the corresponding bulk systems by using the technique described in section 2.3.2.

Before the corresponding materials are considered the impact of the temperature on the lattice conductance is investigated. Since the transmission function is based on *ab initio* calculations, which are performed at 0K and since anharmonic effects are neglected, the transmission function does not depend on the temperature. The only temperature dependency arises due to the occupation function. To estimate the effect of the temperature, the integrand of equation (2.42) is plotted in Fig. 4.22 for different temperatures for the transmission function of ZnO in c-direction. The area under the curves are proportional to the conductance. For low temperatures of 100K only the low energy phonons contribute. Increasing the temperature to 300K leads to a moderate increase of the low energy phonons and to a strong increase in the high energy phonons. Increasing the temperature further keeps the contribution of the low energy phonons nearly constant and leads to a small increase of the contribution of the high energy phonons.

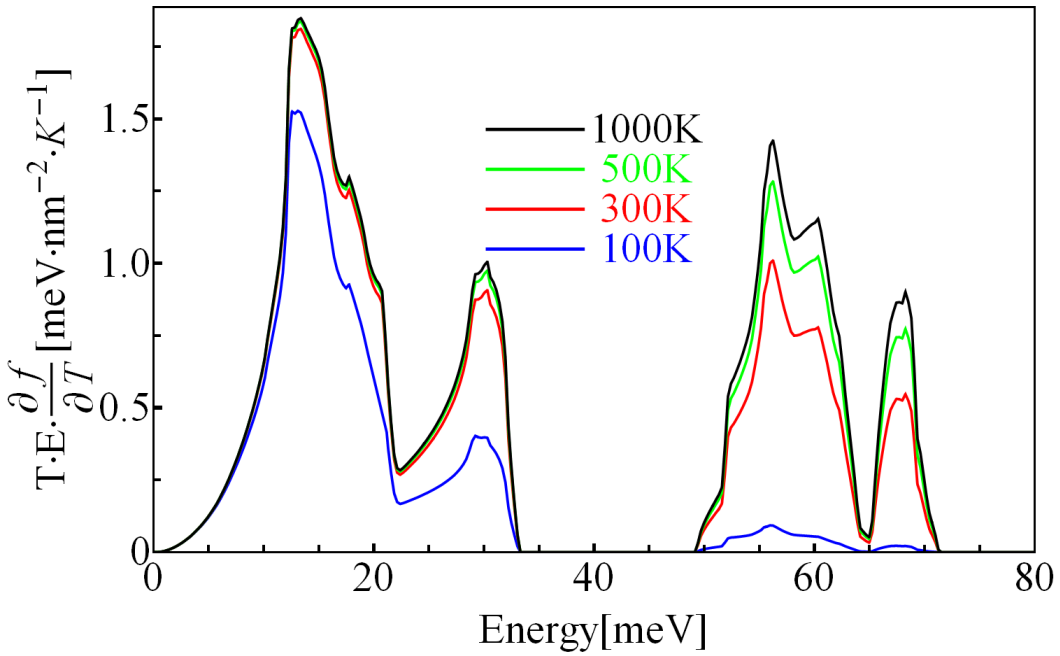


Figure 4.22: Transmission times phonon energy times derivative of the occupation function for different temperatures. Note that corresponding to equation (2.42) the areas of the curves give the thermal phonon conductance $\kappa_{ph}$.

### 4.1.1 ZnO phonon bulk properties

All ZnO bulk calculations are performed with an cutoff radius of 60 Hartree and a kpoint mesh of 6x6x3. This parameter set is sufficient to converge the results based on these calculations within 1%. First the ZnO cell is relaxed. The relaxed lattice constants are 3.198Å for the a-parameter, 5.167Å for the c-parameter and 0.379 for the u parameter. The lattice constants for ZnO wurtzite are about 1.6% smaller than the measured ones (see table 3.1). The volume is about 3.9% too small. The overestimation of the binding is a well known feature of LDA approximation.

Fig. (4.23) shows the density of states and the dispersion relation of ZnO. ZnO has 4 atoms in the unit cell, hence there are 12 phonon modes. The first six modes are separated by an energy gap of 17meV from the last six modes. The maximum energy of the ZnO phonon density of state is at 70meV. The highest energy is also called the cutoff energy or if the frequency is considered cutoff frequency.

Fig. 4.24 (left) shows the transmission function of ZnO in different transport directions. A small anisotropy between the transport in c-direction and a- and m-direction can be observed. From the transmission function of the bulk system the maximum thermal conductance can be obtained using equation (2.42). The bulk conductance is shown in Fig. 4.24 (right).

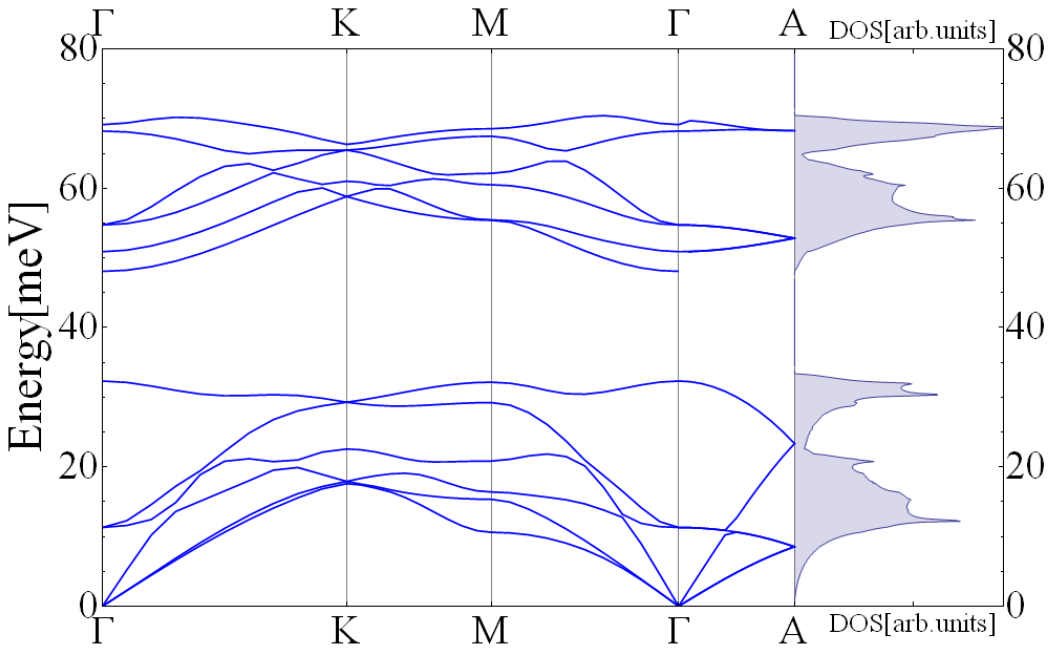


Figure 4.23: Dispersion relation and phonon density of states of ZnO in wurtzite structure. (reference [E1])

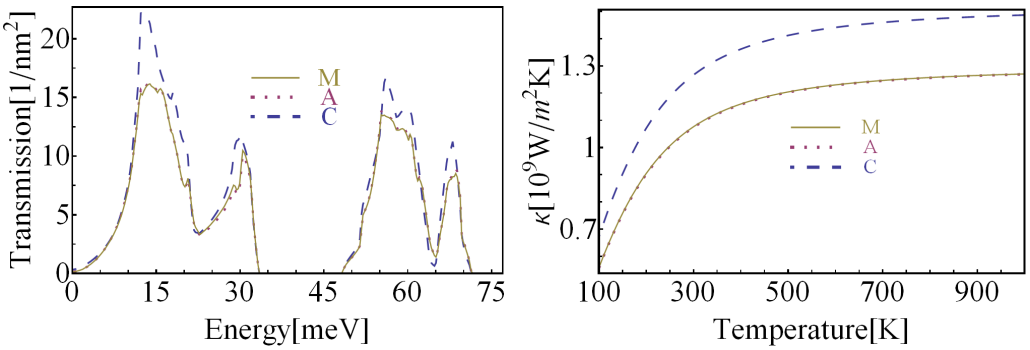


Figure 4.24: Transmission function of ZnO in different transport directions (left) and corresponding thermal conductivities (right). (reference [E1])

The thermal conductance shows also an anisotropy between the c-direction and a- and m-direction. The thermal conductance in c-direction is about 20% higher than the conductance in the other two directions. Experimentally an anisotropy in the thermal conductivity can be also observed, but here the thermal conductivity in a-direction is 20% higher than the conductivity in c-direction [68].

The temperature dependence of the conductance for all directions is similar. The conductance shows a strong increase with temperature for lower temperatures of 300K. Above 300K the increase with temperature flattens. This behavior can be explained as follows. At low temperatures with increasing the temperature more and more modes get occupied and can contribute to the conductance. For higher temperatures all modes are already occupied and an increase in the temperature leads only to a slightly higher occupation number which results in a minor increase of the conductance.

Since scattering is neglected the contact conductance shown here is the highest possible lattice conductance that can be achieved for the corresponding material. Experimentally these conductances can only be measured at low temperatures or at very short length scales. Experimental values for ZnO from 30K to 300K are shown in Fig. 4.25. To compare the experimental values with the theoretical ones, one has to keep in mind that the theoretical conductance is independent of the length of the sample and has therefore the unit of an interface conductance. To get an idea at which length scales the theoretical conductance shown in Fig. 4.24 is comparable to the conductivity shown in Fig. 4.25 a sample with a length of 300nm at 100K is considered. Using the experimental bulk conductivity one obtain a bulk conductance for this sample of $0.7 \cdot 10^9 \frac{W}{m^2 K}$, which is in the same order of magnitude of the theoretical contact conductance in Fig. 4.25. At 300K the bulk conductance became comparable to the contact conductance at 27nm.

### 4.1.2 ZnS phonon bulk properties

The bulk calculations for ZnS in wurtzite structure are performed with a cutoff radius of 60 Hartree and a kpoint mesh of 6x6x3. The bulk calculations for ZnS in zincblende structure are performed with a cutoff radius of 60 Hartree and a kpoint mesh of 4x4x4. These parameter sets are sufficient to converge the results based on these calculations within 1%. The relaxed lattice parameters for ZnS in wurtzite structure are 3.755Å for the a-parameter, 6.168 Å for the c-parameter and 0.374 for the u-parameter. In zincblende structure the lattice parameter is 5.32Å(see table 3.3). Fig. 4.26 shows the phonon density of states and dispersion relation for ZnS in wurtzite structure (left) and zincblende structure (right). In wurtzite structure there are 12 modes, whereas the lower six modes are seperated by the upper six modes by an energy gap of 11.5meV. Since in the zincblende structure the unit cell has only two atoms there are only 6 modes. The lower three modes are seperated by the upper three modes by

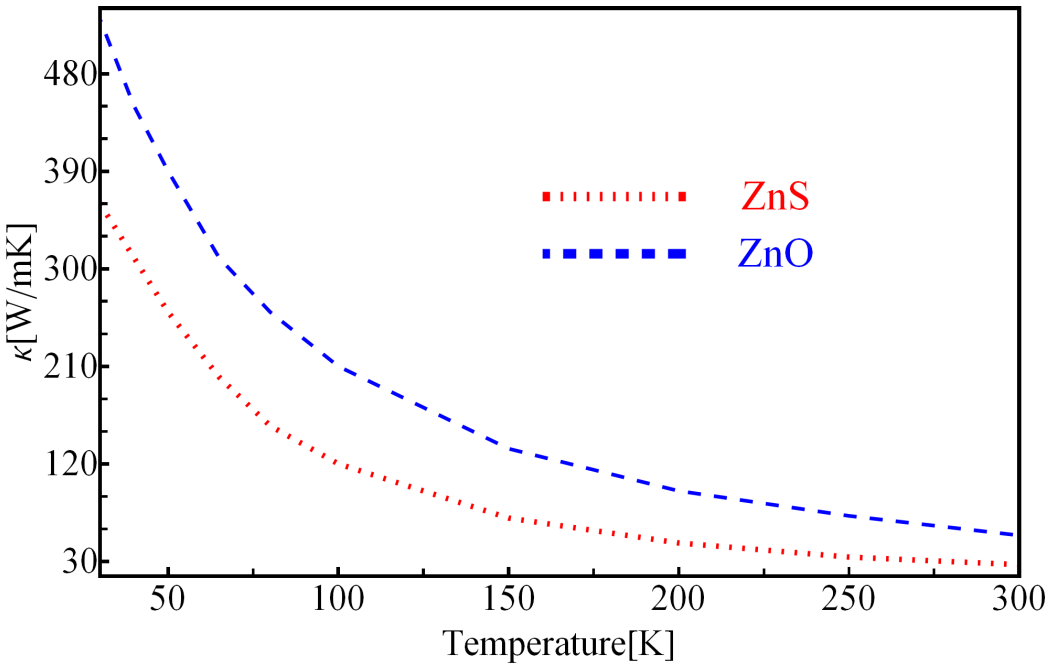


Figure 4.25: Experimental values for the thermal conductivity of wurtzite ZnO and zincblende ZnS. Values are taken from reference [68].

an energy gap of 9meV. Although the phonon densisty of states of zincblende structure and wurtzite structure are different, the maximum energy as well as the gap occur at nearly the same energies.

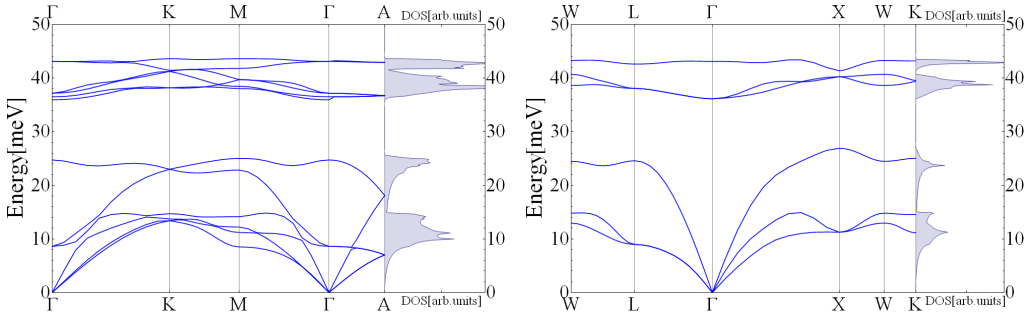


Figure 4.26: Dispersion relation and phonon density of states of ZnS in wurtzite structure (left) and zincblende structure (right) for different directions. (reference [E1])

Fig. 4.27 shows the transmission functions of ZnS in wurtzite structure (left) and zincblende structure (right). The transmission functions in zincblende structure show nearly no anisotropy. In wurtzite structure there is a small anisotropy. The transmission function in c-direction is slightly higher at low energies and slightly lower for high energies than in the a- and m-direction. The corresponding conductances for ZnS are shown in Fig. 4.28. For wurtzite

structure the small anisotropy observed in the transmission functions does not lead to a significant anisotropy in the conductance since the area under the different transmission functions are nearly the same for all temperatures. The conductance in zincblende structure shows a very small anisotropy. The conductance in 111-direction is 2.5% higher than the in the other two directions. Since the transmission functions in zinblende structure have a very similar form this small anisotropy can be hardly seen just from the transmission functions. The temperature dependence in both cases is similar to the ZnO case. For low temperatures between 100K and 300K the conductance increases. At low temperatures only a small number of modes are occupied, by increasing the temperature more and more modes can contribute to the transport. When all modes are occupied an increase in temperature results only in a small increase in the conductance. The slopes at low temperatures are slightly stronger than in the ZnO case. This is because in ZnS the energy states are lower and narrower in energy. Nevertheless, it is remarkable that the conductance in ZnO is approximately a factor of two higher than in ZnS. The experimental conductivities show a similar ratio [68].

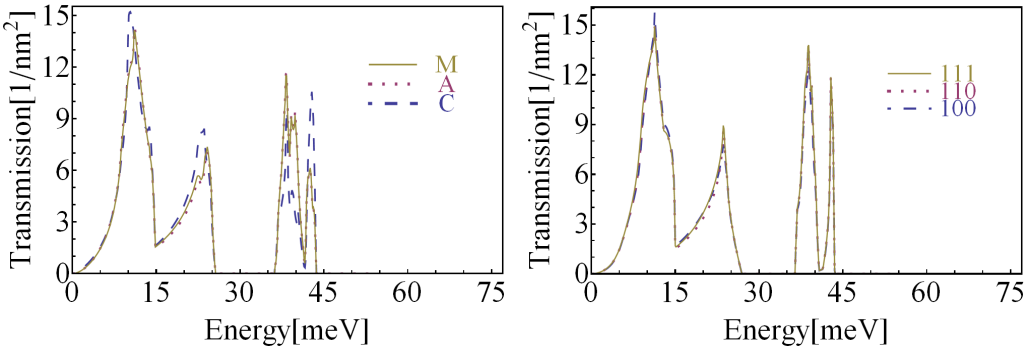


Figure 4.27: Transmission function of ZnS in wurtzite structure (left) and zincblende structure (right) for different directions. (reference [E1])

### 4.1.3 Interface conductance using the diffusive mismatch model

To estimate the interface conductance between ZnO and ZnS the DMM is used. Before the focus is set to the specific interfaces, again the density of states of ZnO and ZnS are considered. In Fig. 4.29 the density of states of ZnO and ZnS are shown. It can be seen that there is no overlap between the phonon states in ZnO and ZnS above 28meV regardless of the structure of ZnS. This is a promising result since it shows that all phonons with energies higher than 28meV are blocked at ZnO/ZnS interfaces. To get a quantitative estimation of the interface conductance the interface conductance is calculated for several interfaces within the DMM.

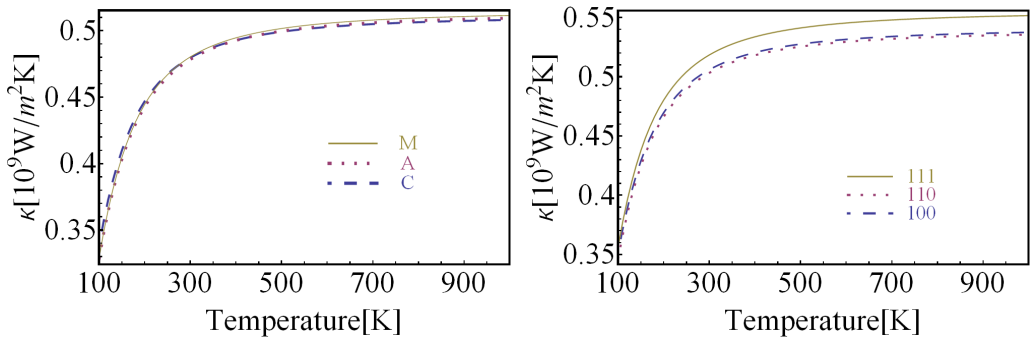


Figure 4.28: Thermal conductance for ZnS wurtzite structure (left) and zincblende structure (right). (reference [E1])

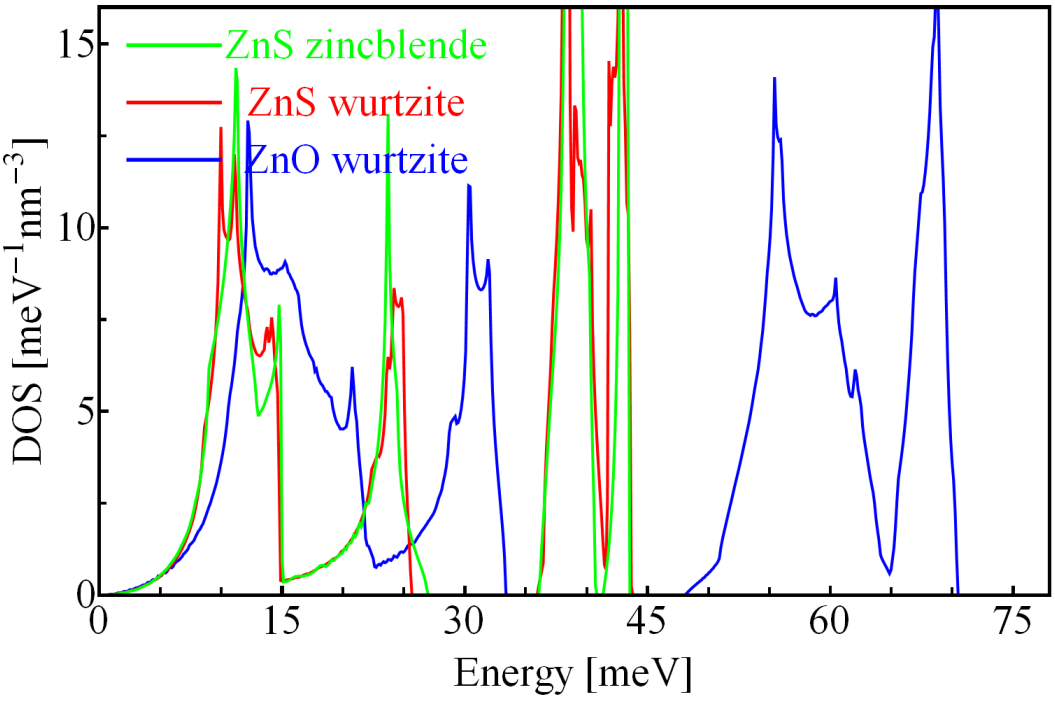


Figure 4.29: Phonon density of states of ZnO and ZnS.

In this work six different interfaces are considered. Three interfaces are between ZnO wurtzite and ZnS wurtzite structure, where both structures are oriented in the same direction. These interfaces are marked with ZnOC/ZnSC, ZnOA/ZnSA and ZnOM/ZnSM. The other three interfaces under consideration are between ZnO in wurtzite structure and ZnS in zincblende structure. Since the transmission functions in the zincblende structure show only a very small anisotropy between the different directions it is enough to consider only one direction. The three interfaces between these structures are therefore indicated with ZnOC/ZnS100, ZnOA/ZnS100 and ZnOM/ZnS100. Fig. 4.30 shows the corresponding transmission function in the DMM between ZnO wurtzite structure and ZnS wurtzite structure (left) and ZnO wurtzite structure and ZnS zincblende structure (right). It can be seen, that for all interface transmission functions the transmission function is zero for all energies above 28meV. The reason for the cutting of the transmission function above 28meV is discussed in the last paragraph. The corresponding interface conductances are shown in Fig. 4.31. These interface conductances are approximately one order of magnitude higher than typical interfaces conductances reported in the literature [69, 70], which can be explained by the rough assumptions that enter the DMM.

The impact of such interfaces on the figure of merit can be estimated by computing the total conductance per $m^2$ of a sample with ZnO/ZnS interfaces. The total conductance per $m^2$ is calculated using

$$G = \left[ (\frac{\kappa_{ZnO}}{L/2})^{-1} + (\frac{\kappa_{ZnS}}{L/2})^{-1} + n \cdot (\kappa_{Int})^{-1} \right]^{-1}. \tag{4.216}$$

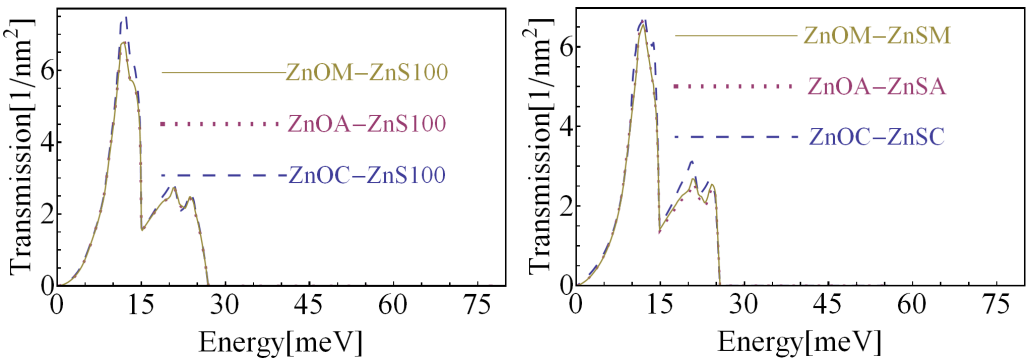


Figure 4.30: Left: Interface conductance between ZnO wurtzite and ZnS zincblende interfaces. Right: Interface conductance between ZnO wurtzite and ZnS wurtzite interfaces. (reference [E1])

L is the length of the structure and n is the number of interfaces. $\kappa_{ZnO}$ and $\kappa_{ZnS}$ are the bulk conductivities and $\kappa_{Int}$ is the interface conductance. Using this formula implies that the interfaces are independent, which means that the scattering of the phonons between two interfaces is strong enough to lose

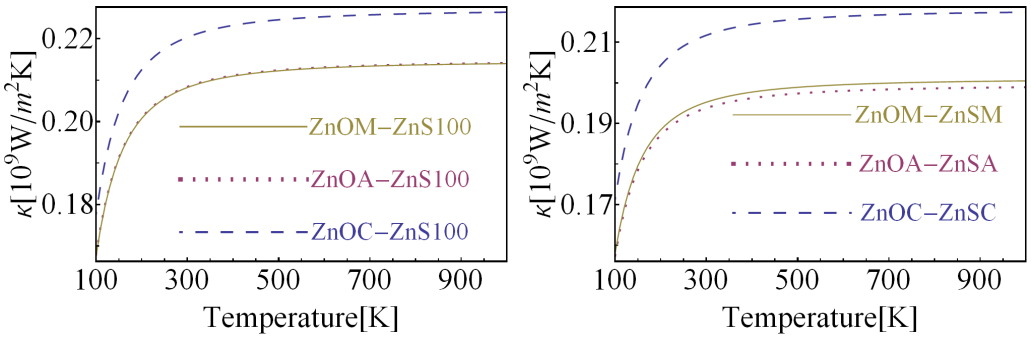


Figure 4.31: Left: Interface conductance between ZnO wurtzite and ZnS zincblende interfaces. Right: Interface conductance between ZnO wurtzite and ZnS wurtzite interfaces. (reference [E1])

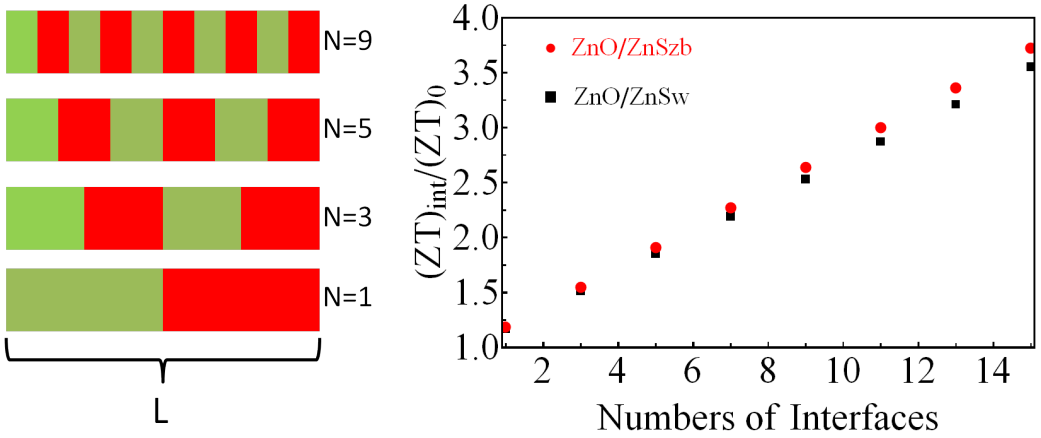


Figure 4.32: Left: Sketch of some samples under consideration. Right: Figure of merit ZT as a function of the number of interfaces normalized to the ZT value without an interface. (reference [E1])

| Parameter | Value |
|---|---|
| $\kappa_{ZnO}$[68] | 54W/mK |
| $\kappa_{ZnS}$[68] | 27W/mK |
| $\kappa_{ZnO/ZnSw}$ | $0.21{\cdot}10^9$ W/m$^2$K |
| $\kappa_{ZnO/ZnSzb}$ | $0.19{\cdot}10^9$ W/m$^2$K |
| L | $1.0 \cdot 10^{-6}$m |

Table 4.5: Parameters and references used for Fig. 4.32. The interface conductance $\kappa_{ZnO/ZnSw}$ and $\kappa_{ZnO/ZnSzb}$ are the average values of the different interfaces shown in Fig. 4.31. The values are taken at a temperature of 300K. $\kappa_{ZnO}$ is the ZnO bulk thermal conductivity at 300K averaged over the different directions [68]. $\kappa_{ZnS}$ is the ZnS zincblende bulk thermal conductivity at 300K averaged over the different directions [68].

the phase information. Fig. 4.32 shows the figure of merit with different interfaces divided by the figure of merit without interfaces. In this calculation only the impact on the phonon thermal conductance is taken into account. Thus, the ratio of $(ZT)_{int}$ with interfaces and by ZT without interfaces is given by $\kappa_{ZT}/\kappa_{ZT_{int}}$. For $\sigma_{Int}$ an average value of the interface conductance of ZnO/ZnS/wurtzite and ZnO/ZnS/zincblende is used. The bulk conductivities were taken from [68]. All parameters used for this plot are listed in Table 4.5. It can be seen that the figure of merit increases linearly with the number of interfaces. The slope of this curve is given by the inverse of the interface conductance. Consequently, superlattice structures of ZnO/ZnS could be promising for a substantial increase of the figure of merit in thermoelectric devices. However, one should keep in mind that only thermal contribution were taken into account.

### 4.1.4 $ZnO_xS_{1-x}$ alloys

Besides the approach of using ZnO/ZnS interfaces to increase the figure of merit, another idea is to incorporate sulfur atoms in ZnO and oxygen atoms in ZnS. In such $ZnO_xS_{1-x}$ alloys it is also expected that the phonon scattering is reduced due to the disordering of the atoms. To confirm this assumption the AGF method is used to calculate coherent phonon scattering in wurtzite ZnO on sulfur impurities and in wurtzite ZnS on oxygen impurities. Here, two different geometries and transport directions are considered. Since not only the bulk ifcs are needed, additional supercell calculations have to be performed to get the ifcs of the impurities and its surroundings. In Fig. 4.33 the geometry of the transport calculation and the connection to the ifcs is sketched. The ifcs of the impurity layer (yellow) and the ifcs of the neighboring layers (blue) are obtained within a supercell calculation. The ifcs for the bulks layers (dark green) and the ifcs used in the semi infinite leads (green) are obtained from a

bulk calculation. For the coupling between the atoms in the adjacent region of the impurity layer (blue region) and the bulk layers (dark green) also the bulk ifcs are used. This is of course an approximation, but for large enough supercells the error due to this approximation tends to zero.

Fig. 4.34 shows a sketch of the corresponding geometries and supercells. In the first geometry (Fig. 4.34 left), the crystal in c-direction is considered with one oxygen/sulfur monolayer replaced by a sulfur/oxygen monolayer respectively. This supercell consists of 16 atoms. In the second geometry (Fig. 4.34 right), transport in a-direction is considered. Here the supercell consists of 4 monolayers, where each monolayer has two oxygen/sulfur atoms and two zinc atoms. In one of those layers one oxygen/sulfur atom is replaced by a sulfur/oxygen atom. As mentioned earlier an error is introduced by using the bulk ifcs to connect the region adjacent to the impurity layer with the bulk layers. This error decreases with the size of the supercell in transport direction. The presented geometries consists of 16 monolayers for transport in c-direction and 4 monolayers for transport in a-direction. Especially the transport results in a-direction will therefore be only a rough estimation.

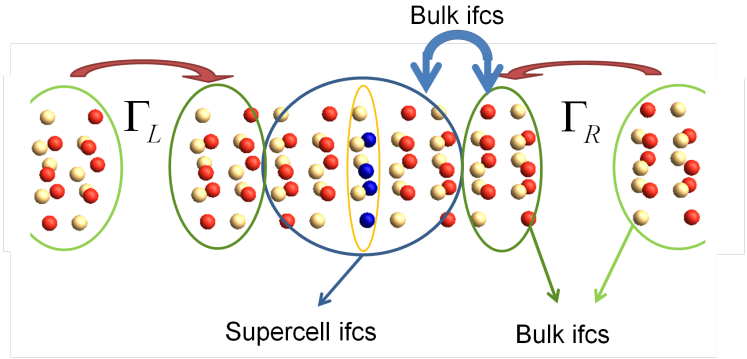


Figure 4.33: Atomistic picture of the system and the corresponding ifcs. (reference [E2])

**4.1.4.1 Transport in c-direction with an impurity layer** Fig. 4.35 shows the phonon density of states of the supercell shown in Fig. 4.34 left for ZnO with a sulfur monolayer (left panel) and ZnS with an oxygen monolayer (right panel) in comparison to the corresponding bulk material. Due to the introduction of the impurity monolayer new phonon states arise in the gaps of ZnO and ZnS. In addition, in ZnS new states exists at higher energies that are connected to a local oxygen mode.

The transmission functions for the transport geometry given in the left panel of Fig. 4.35 are shown in Fig. 4.36, left for ZnO and right for ZnS. To distinguish between the effect of the change in the mass and the effect of the change in the ifcs, the transmission functions, where only the mass is changed, are also calculated (Fig. 4.36 red plots). Just the change in the mass causes

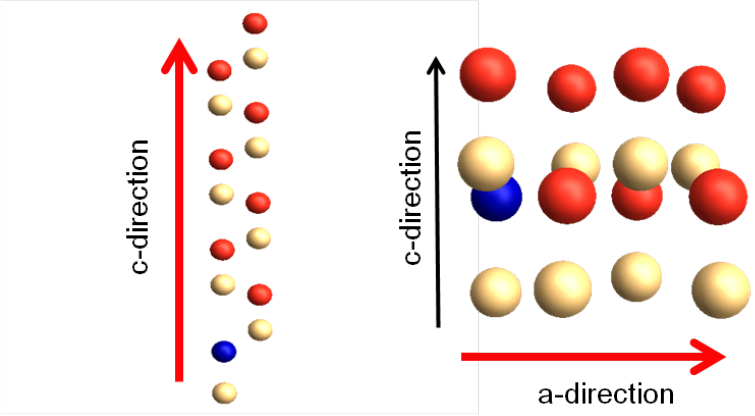


Figure 4.34: Geometries and corresponding supercells under consideration. White spheres represents zinc atoms, red spheres represents oxygen or sulfur atoms and blue spheres represent the impurities. Left: Supercell of 16 atoms in c-direction with one impurity monolayer. Right: Supercell of 16 atoms in a-direction with impurity atom. The red arrow indicates which direction is considered as the transport direction. All cells are in wurtzite structure.

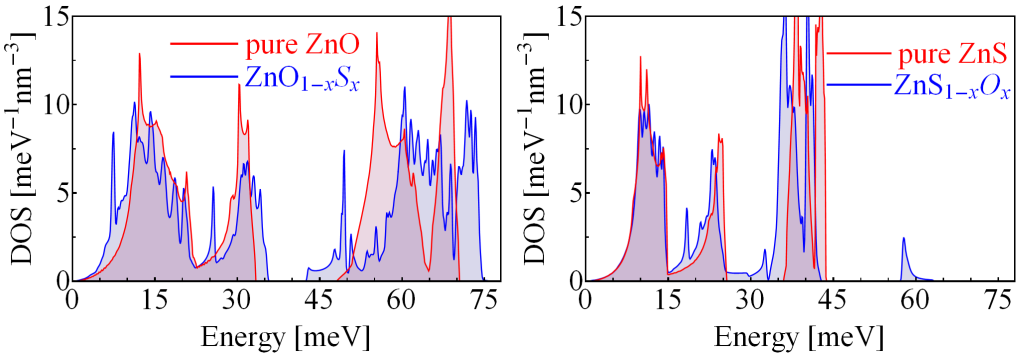


Figure 4.35: Phonon density of states of the supercell shown in the left panel of Fig. 4.34. Left: ZnO with an impurity sulfur monolayer in comparison to bulk ZnO. Right: ZnS with a impurity oxygen monolayer in comparison to bulk ZnS. (reference [E2])

a strong decrease in the transmission function of the high energy phonons. This can be explained with the previous mentioned lack of overlapping of the density of states of ZnO and ZnS at higher energies (see Fig. 4.29). The low energy phonons on the other hand are hardly influenced by the change of the mass of one monolayer. Taking into account also the change in the ifcs the transmission function at low energies is strongly decreased. The explained behavior is qualitative the same for the ZnO and the ZnS system.

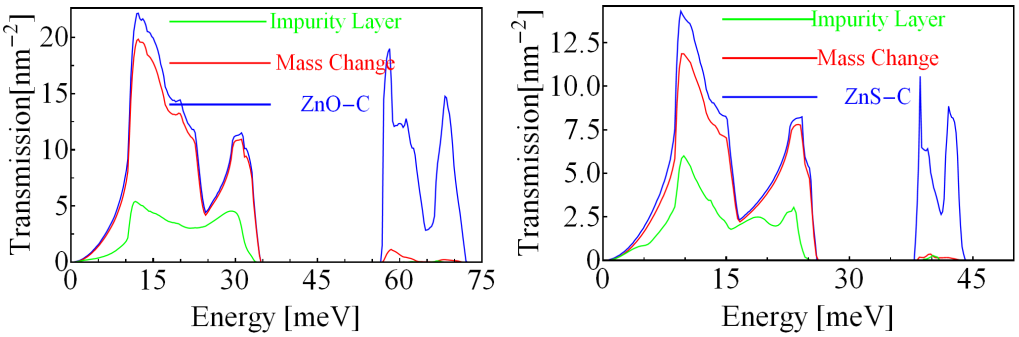


Figure 4.36: Left: Transmission function for pure ZnO in c-direction (blue), with a change of the mass of one oxygen monolayer to the mass of sulfur (red) and with the impurity monolayer of sulfur by considering a change in mass and in the ifcs (green). Right: Transmission function for pure ZnS in c-direction (blue), with a change of the mass of one sulfur monolayer to the mass of oxygen (red) and with the impurity monolayer of oxygen by considering a change in mass and in the ifcs (green). (reference [E2])

**4.1.4.2 Transport in a-direction with impurities** Fig. 4.37 shows the phonon density of states of the supercell shown in Fig. 4.34 right for ZnO with a sulfur impurity (left panel) and ZnS with an oxygen impurity (right panel) in comparison to the corresponding bulk material. Due to the introduction of the impurity layer new phonon states arise in the gaps of ZnO and ZnS. In addition, in ZnS new states exist at higher energies that are connected to a local oxygen mode. This is the same behavior as already observed in the previous section.

In Fig. 4.38 the transmission functions for transport in a-direction are presented. Here also the change in the ifcs and the change in the mass are investigated independently. Compared to the transport calculations in c-direction the effects are similar. A change in the mass reduces the transmission probability of the high energy phonons. The effect on the low energy phonons is very small. Compared to the transport calculation in c-direction the decrease in the transmission function is less. This is not surprising, since in the case of transport in c-direction a whole impurity monolayer was assumed, whereas here only every fourth atom in the monolayer is an impurity. If in addition the

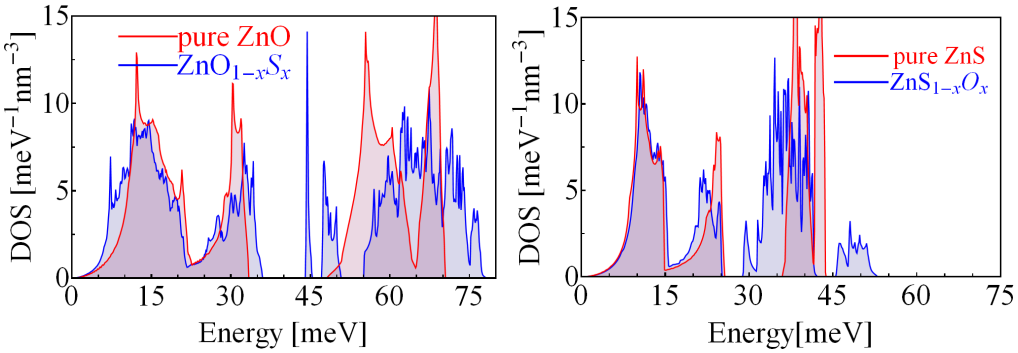


Figure 4.37: Phonon density of states of the supercell shown in the right panel of Fig. 4.34 Left: ZnO with sulfur impurities. Right: ZnS with oxygen impurities. (reference [E2])

change in the ifcs is considered also the low energy phonons are affected. Also here this effect is weaker then in the case of an impurity monolayer. However, the reduction is already quite substantial keeping in mind that only one atomic monolayer is considered where the impurities (every fourth atom) are present. Therefore, it can be expected that the effect is drastically increased by going to thicker impurity layers.

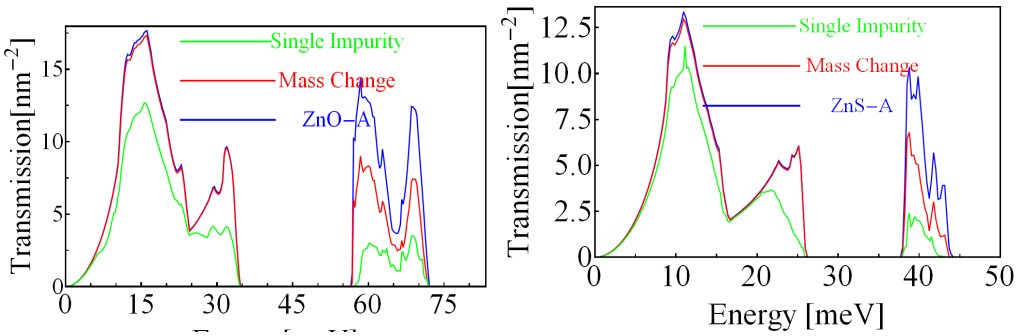


Figure 4.38: Left: Transmission function for pure ZnO in a-direction (blue), with a change of the mass of some oxygen atoms to the mass of sulfur (red) and with impurity atoms of sulfur by considering a change in mass and in the ifcs (green). Right: Transmission function for pure ZnS in a-direction (blue), with a change of the mass of some sulfur atoms to the mass of oxygen (red) and with impurity atoms of oxygen by considering a change in mass and in the ifcs (green). (reference [E2])

### 4.1.5 Discussion of ZnO/ZnS phonon scattering

The latter sections show that ZnO/ZnS based materials exhibits a strong phonon scattering. The main reason for that behavior is that the phonon

density of states of ZnO and ZnS show no overlap at higher energies. Hence, the phonon scattering is stronger for the high energy phonons. The strong phonon scattering is observed at ZnO/ZnS interfaces and in $ZnO_xS_{1-x}$ alloys. For thermoelectrics this behavior can be used to increase the efficiency and therefore the figure of merit ZT.

## 4.2 Electron transport in nanograined structures

The model presented in section 2.5 is used to investigate the electronic part of the thermoelectric properties of nanograined structures. For the 1-dimensional transmission function two different models are considered. A step transmission function and the correct transmission functions for double Schottky barriers are used. The step transmission function has the advantage that this transmission function leads to an analytic expression for the total transmission function.

### 4.2.1 Modeling the grain boundary using a step transmission function

Fig. 4.39 shows that the transmission function of a double Schottky barrier can be roughly approximated by a step like function as long as the transmission barrier height and width is not too small.

In general a double Schottky barrier and therefore the barrier height $U_B$ is a complicated function of the doping concentration $N_D$, the trapping density $N_T$, the length of the grain $l_g$, and the thickness of the interface $l_i$. Since these parameters also influence the chemical potential $\mu$, it is in general not possible to vary the chemical potential $\mu$ and the barrier height $U_B$ independently. Nevertheless, in this section the barrier height and the chemical potential are varied independently to find out under which conditions the thermoelectric parameters are optimized. Subsequently in the next section it is analyzed whether these conditions can be fulfilled in real materials. The model 1D steplike transmission function $t_{1D}$

$$t_{1D}(E) = \begin{cases} 1 & E > U_B \\ 0 & E \leq U_B \end{cases} \tag{4.217}$$

leads to an analytic expression for the total transmission function of the solid $\overline{t_{Solid}}$ (see equation 2.214)

$$\bar{t}_{Solid}(E) = \begin{cases} \frac{m_{eff}}{2\pi\hbar^2} \cdot E \cdot \frac{\lambda(E-U_b)l_g}{El_g+U_b(\lambda-l_g)} & E > U_B \\ 0 & E \leq U_B \end{cases}. \tag{4.218}$$

To make general statements, parameters are used that are typical for a semiconductor. The parameters used in this chapter are listed in table 4.6. First the bulk values are considered which means that $U_b$=0. Fig. 4.40 shows the thermoelectric coefficients without a barrier vs. the chemical potential.

The bulk conductivity shows a nearly linear behavior with the chemical potential. The magnitude of the Seebeck coefficient shows moderate values for low chemical potential and decreases rapidly with increasing the chemical potential. Since an energy independent $\lambda$ is used, the only energy dependence in the transmission function is due to the energy dependence of the number of modes. The bulk power factor shows a maximum at approximately $\mu$=0.015eV.

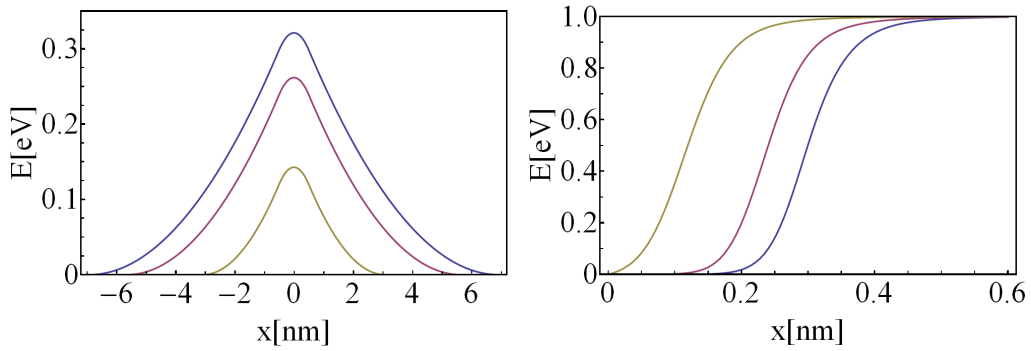


Figure 4.39: Left: double Schottky barriers of different height and width. Right: Corresponding transmission functions.

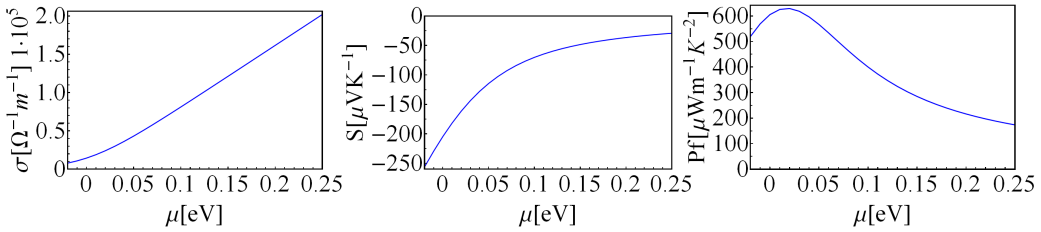


Figure 4.40: Left: electric conductivity vs. chemical potential. Middle: Seebeck coefficient vs. chemical potential. Right: Power factor $\sigma S^2$ vs. chemical potential. All quantities are calculated without a barrier $U_b$=0.

A certain chemical potential corresponds to a certain free charge carrier density at a certain temperature. In Fig. 4.41 the free charge carrier density vs. the chemical potential is shown.

From Fig. 4.41 the charge density at which the bulk power factor has its maximum can be determined. Since the bulk power factor has its maximum at $\mu$=0.015eV, the optimum free charge carrier density is $3 \cdot 10^{18}\text{cm}^{-3}$.

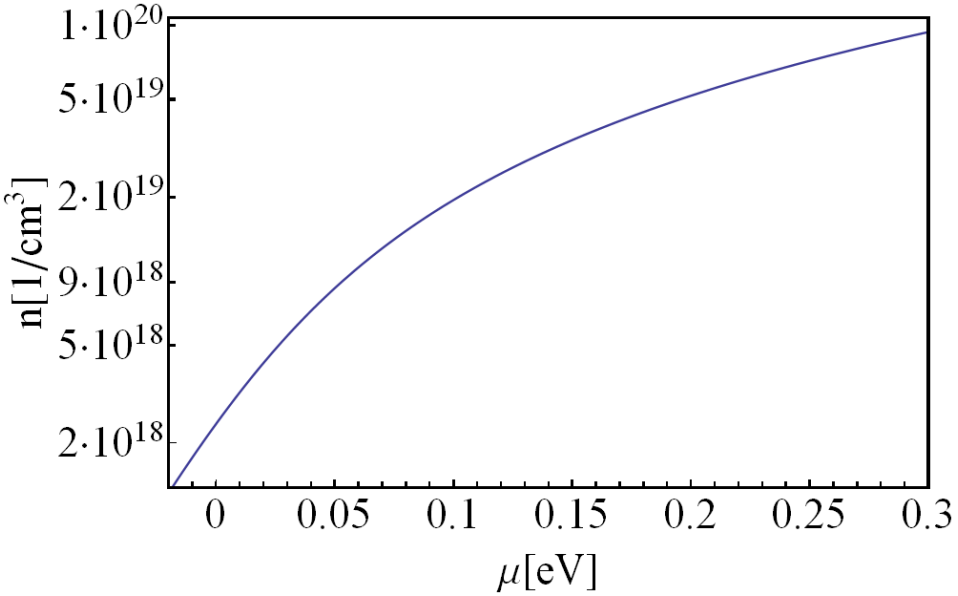


Figure 4.41: Free charge carrier density vs. chemical potential.

Fig. 4.42 shows the thermoelectric coefficients for different barrier heights and chemical potentials and for different grain sizes. A few general trends can be seen. The conductivity increases with increasing the chemical potential and decreases with increasing the barrier height. The Seebeck coefficient shows the opposite behavior. For a given chemical potential the power factor has a maximum if the barrier height is around the chemical potential. The power factor can be increased by increasing the chemical potential and using the optimum barrier height. This shows that it is possible to increase the power factor due to a barrier between the grains. This was also shown in reference [15]. However, it was mentioned before that the barrier height and the chemical potential can not be varied separately. In the next chapter it is investigated if it is possible to tune the physical parameters in such a way that the power factor can be increased.

### 4.2.2 Modeling the grain boundary using a double Schottky barrier

In this section the real transmission function of a double Schottky barrier is used. The transmission function is obtained using equation (2.152). Transmission functions for different barriers are shown in Fig. 4.39. To make quantitative judgments the thermoelectric coefficients for different chemical potentials

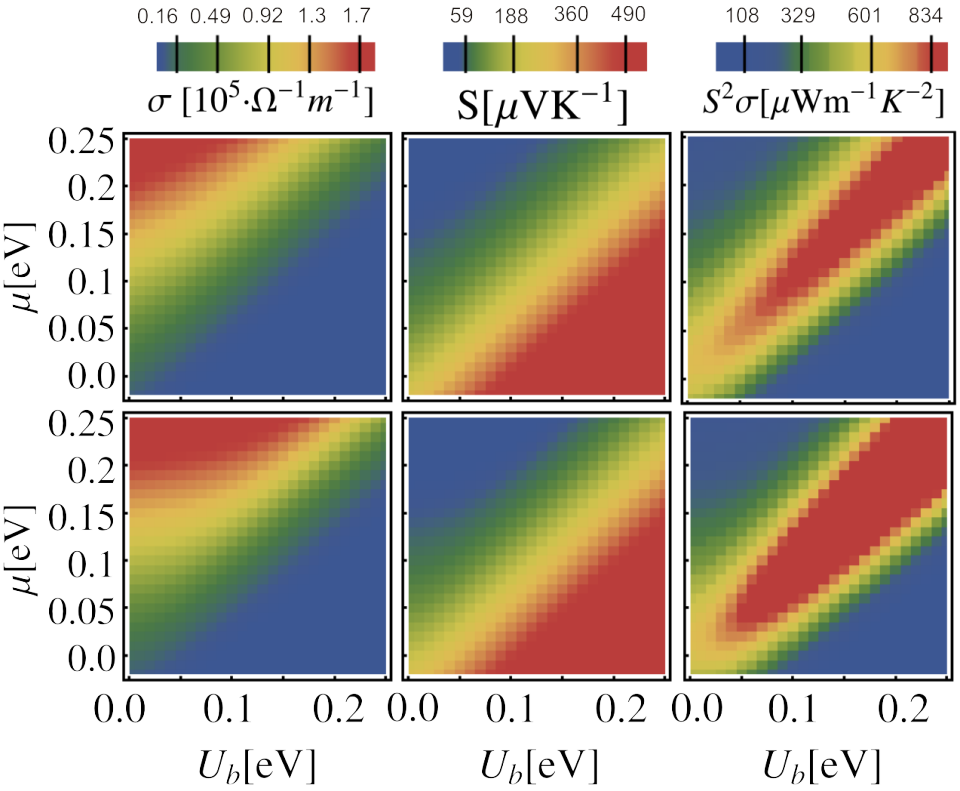


Figure 4.42: Electric conductivity $\sigma$, Seebeck coefficient S, and power factor $S^2\sigma$ vs. chemical potential $\mu$ and barrier height $U_b$ for different grain sizes $l_g$. Top: $l_g$=50nm. Bottom: $l_g$ =200nm. Red indicates high values and blue indicates low values. (reference [E3])

| Parameter | Symbol | Value |
|---|---|---|
| Energy of the donor level | $E_D$ | -0.02eV |
| Energy of the trapping states | $E_T$ | -0.5eV |
| Length of the interface | $l_i$ | 1nm |
| Effective mass | $m_{eff}$ | 0.25 |
| Scattering constant (equation (2.210)) | $\lambda_0$ | 20nm |
| Scattering exponent (equation (2.210)) | $r$ | 0 |
| Temperature | $T$ | 300K |

Table 4.6: Parameters used in this section

and different potentials are calculated by altering the densities of the surface states $N_T$. $N_T$ is altered from 0 to 2 $\cdot 10^{20}\mathrm{cm}^{-3}$. Since the interface thickness is 1nm this corresponds to a total trapped charge density $Q_T$ of 2 $\cdot 10^{13}\mathrm{cm}^{-2}$. Hence, the range of $N_T$ covers typical values for $Q_T$ [45]. All parameters used for these calculations are shown in table 4.6.

In Fig. 4.43 results are shown for the thermoelectric coefficient vs. chemical potential $\mu$ and densities of the surface states $N_T$. Increasing the chemical potential increases the electric conductivity and reduces the Seebeck coefficient. Increasing the densities of the surface states leads to an increase of the barrier height and therefore reduces the electric conductivity and increases the Seebeck coefficient. The latter behavior can only be observed for low chemical potentials, because for larger chemical potentials a higher donor concentration $N_D$ is required. A high donor concentration leads to a high effective screening of the trapped surface charge and therefore reduces the height and the width of the barrier.

In Fig. 4.44 the power factor for different chemical potentials and grain sizes are plotted. This means that these plots are basically cuts through the areas in Fig. 4.43. For low chemical potentials the power factor is reduced with increasing densities of the surface states. For high chemical potentials there is no influence on the power factor of the densities of the surface states. The grain size has only a small effect on the power factor. An appreciable enhancement of the power factor is not observed for any of the considered grain sizes.

As previously mentioned the quantity that links the material parameters with the efficiency is the figure of merit ZT and not the power factor. Nevertheless, if the thermal conductivity is dominated by the lattice contribution the optimization of the power factor also optimizes the figure of merit. To estimate the order of magnitude of the electric thermal conductivity Fig. 4.45 left shows the electric thermal conductivity for different chemical potentials vs. the density of surface states $N_T$. For higher chemical potentials, $\kappa_e$ is hardly influenced since a high chemical potential results in a low barrier. For low chemical potentials $\kappa_e$ rapidly decreases with increasing $N_T$, but even without a barrier the absolute value of $\kappa_e$ is much smaller than the smallest lattice thermal conductivities reported [71].

Fig. 4.45 right shows the Lorenz number for different chemical potentials as a function of $N_T$. The Lorenz number always increases with increasing $N_T$, but for low chemical potentials this effect is stronger. The Lorenz number increases because with increasing $N_T$ the barrier increases as well. An increase of the barrier leads to a blocking of the cold electrons, which means that hot electrons are preferred to cross the barrier. Hence, each charged particle carries on average more heat compared to the case without a barrier.

The figure of merit for three different lattice thermal conductivities $\kappa_l = 0.1, 1, 10\mathrm{W}/(\mathrm{mK})$ is presented in Fig. 4.46. The values of $\kappa_l$ are chosen in a way to cover typical ranges of thermoelectric materials. The figure of merit shows in principle the same behavior as the power factor, except that for low $\kappa_l$

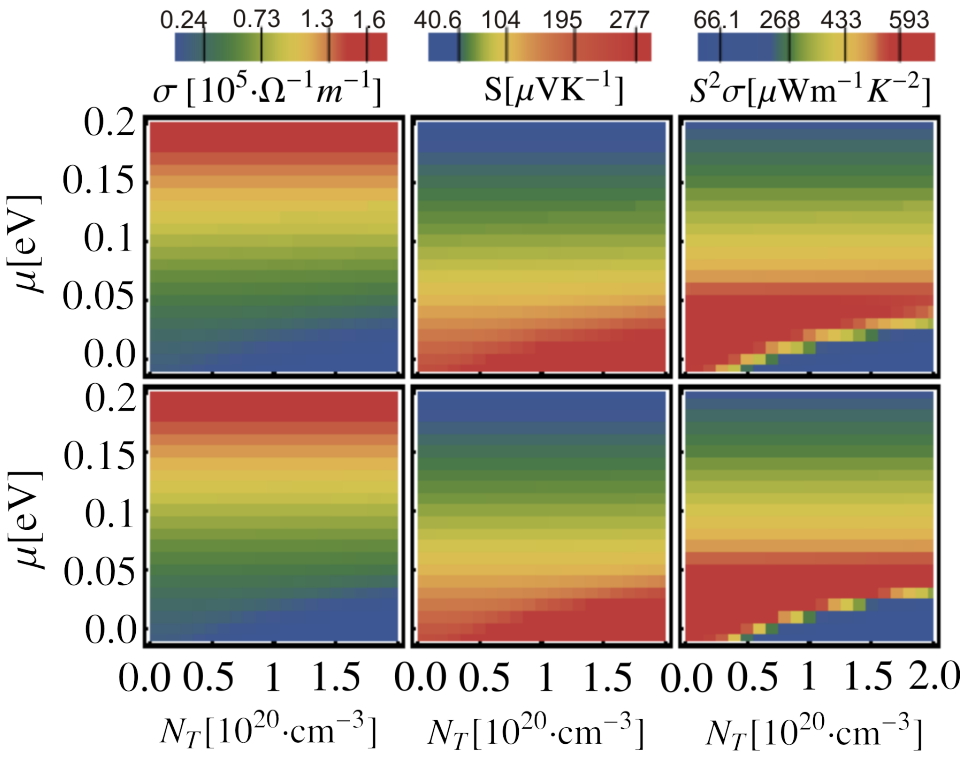


Figure 4.43: Electric conductivity $\sigma$, Seebeck coefficient S, and power factor $S^2\sigma$ vs. chemical potential $\mu$ and densities of the surface states $N_T$ for different grain sizes $l_g$. Top: $l_g$=50nm. Bottom: $l_g$ =200nm. (reference [E3])

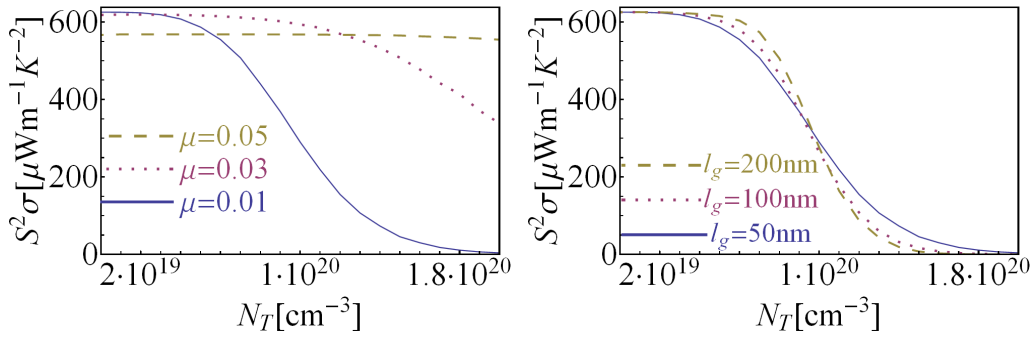


Figure 4.44: Left: Power factor vs. densities of the surface states $N_T$ for different chemical potentials and grain size $l_g$=100nm. Right: Power factor vs. densities of the surface states $N_T$ for different grain sizes and at $\mu$=0.1. (reference [E3])

the figure of merit decreases earlier with increasing chemical potential $\mu$ than the power factor. The reason is that $\kappa_e$ increases and hence reduces the figure of merit with increasing chemical potential. There is no qualitative difference between grain sizes of 50nm and 200nm.

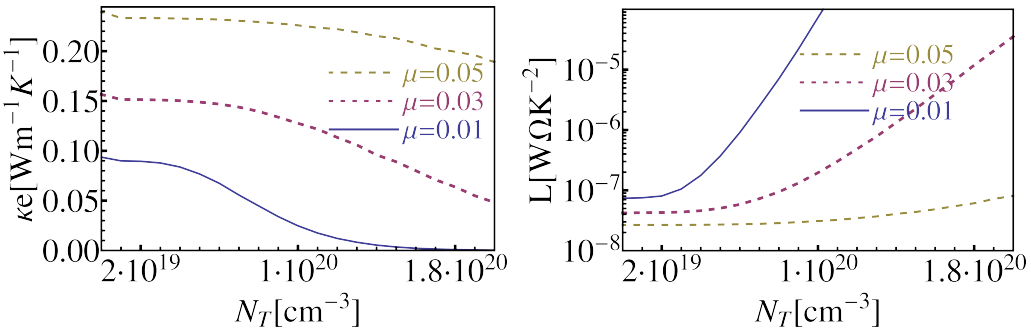


Figure 4.45: Left: Thermal conductivity of the electrons $\kappa_e$ vs. density of surface states $N_T$ for different chemical potentials $\mu$. Right: Lorenz number $L$ vs. density of surface states $N_T$ for different chemical potentials $\mu$. (reference [E3])

### 4.2.3 Discussion electron transport in nanograined structures

In the latter section the thermoelectric parameters of nanograined materials are investigated. In such nanograined materials it is widely believed that an energy dependent filtering effect [72, 73, 74, 13, 14, 12, 15] can increase the Seebeck coefficient and therefore also the figure of merit. Such a filtering effect is reported for indium gallium arsenide superlattice films [75], bulk PbTe with Pb nanoparticles [76], nanocrystalline PbTe [77, 16, 78], nanostructured SiGe [79], and ZnO based materials [19, 23, 24]. In this work an energy dependent filtering could be modeled using a double Schottky barrier and simple step transmission function. In both models the Seebeck coefficient increases with increasing the barrier height whereas the electric conductivity decreases. Using the simple model it could be shown that if the chemical potential is around the barrier height the enhancement of the Seebeck coefficient overcompensates the decrease in the electric conductivity and results in an increase in the power factor. These results are in agreement with Popescu et al.[15]. In their work the authors used a rectangular barrier, which they varied in height and width independently from other parameters. In a more realistic model like the double Schottky barrier the height and width depends on the chemical potential. Hence, the chemical potential, the height, and the width can not be tuned separately. In the last section it was shown that for realistic parameters an increase in the power factor can not be observed due to the barrier. The reason is, that with increasing the chemical potential the height and width of the barrier decreases rapidly. For reasonable chemical potentials the barrier hardly influences the electronic transport. In summary, the energy filtering

effect due to double Schottky barriers does not lead to an enhancement of the efficiency of thermoelectric materials.

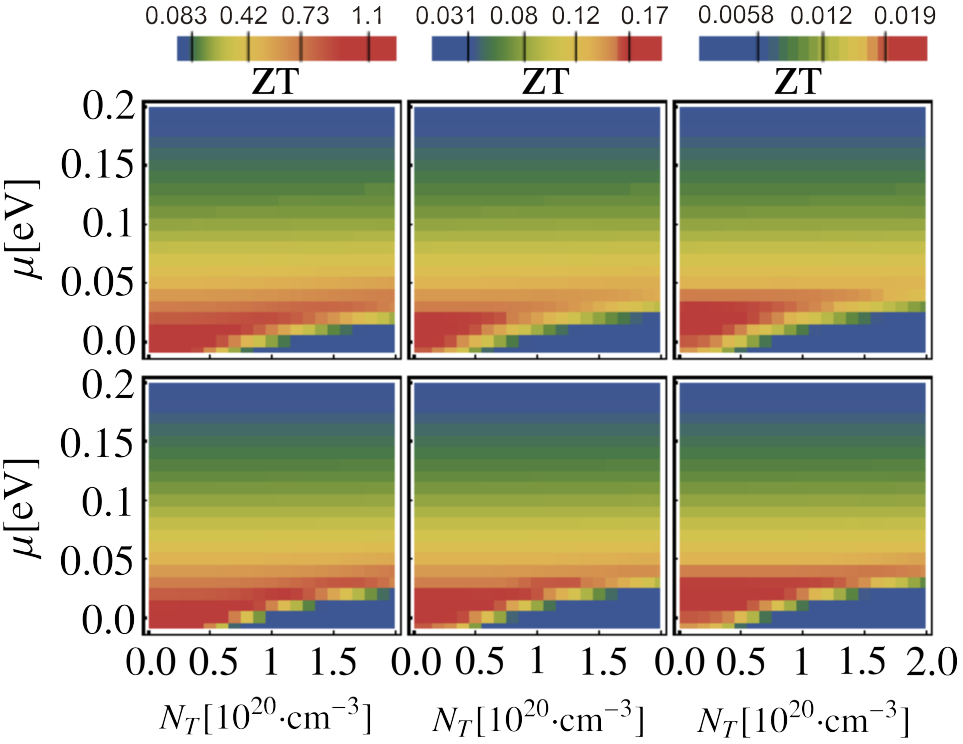


Figure 4.46: ZT vs. chemical potential $\mu$ and density of surface states $N_T$ for $\kappa_l$=0.1W/(mK) (left), $\kappa_l$=1W/(mK) (middle) and $\kappa_l$=10W/(mK) (right) for different grain sizes $l_g$. Top: $l_g$=50nm. Bottom: $l_g$=200nm. (reference [E3])

## 4.3 Coherent phonon scattering in isotope Si superlattices

Besides the material system ZnO/ZnS also Si is investigated in this work. Si especially in combination with Ge is widely used in thermoelectrics. Si inhibits good thermoelectric characteristics like a high electric conductivity and a high Seebeck coefficient. The main drawback of Si as a thermoelectric material is a relatively high thermal conductivity. This is why Si is often used together with Ge. The incorporation of Ge leads to an enhanced phonon scattering which reduces the thermal conductivity and increases the efficiency. Unfortunately, Ge is rare and expensive, this is why Si-Ge thermoelectric generators are only used in spacecraft applications, where the costs are only from minor interest. To establish Si in thermoelectrics for mass market applications it is necessary to find a way to reduce the thermal conductivity without using an expensive and rare material like Ge. To find such materials it is necessary to fully understand the mechanisms that lead to an enhancement of the phonon scattering due to the combination of different materials. There are in principle two reasons that can lead to an enhancement of the phonon scattering, either the phonons get scattered because the inter atomic force constants (ifcs) are different in the combined materials or the ifcs get scattered because the mass of the combined materials differ. Usually both effects occur simultaneously, which makes it difficult to investigate the effects independently. One approach the investigate only the influence of the mass change, is the use of $^{28}$Si/$^{29}$Si or $^{28}$Si/$^{30}$Si superlattices.

The conductivity of $^{28}$Si/$^{30}$Si superlattices are investigated in reference [80]. In this paper the authors employ a model for photons to calculated the transmission probability as a function of the number of interfaces. They showed that within this model the phonon transmission function tend to zero for 70 to 100 interfaces depending on the mass difference between the isotopes. Their results are quite promising but also questionable, since they employ a photon model to calculate phonon transport. Hence, in this section also phonon transmission functions of $^{28}$Si/$^{29}$Si or $^{28}$Si/$^{30}$Si superlattices are calculated but this time the phonon model described in section 2.4.8 is used.

The isotope distribution of Si, found in nature, results in an average mass of 28.085u. To simplify the calculations the isotope distribution, found in nature, is modeled by using just the average mass for each atom. The ifcs for Si are independent of the considered isotope. Hence, the ifcs has to be obtained only once. The ifcs are calculated with a kpoint grid of 10x10x10 and a cutoff-radius of 60 Hartree. The phonon band structure and phonon density of states, based on these ifcs, are shown in Fig. 4.47. Si has two atoms in the unit cell which results in 6 phonon modes. In comparison with ZnO or ZnS there is no gap in the phonon density of states between zero and the maximum energy of 63meV.

The corresponding transmission function in 111 direction for this system is shown in Fig. 4.48 left panel. The transmission functions for the different Si isotopes are shown in Fig. 4.48 right panel. The transmission function is

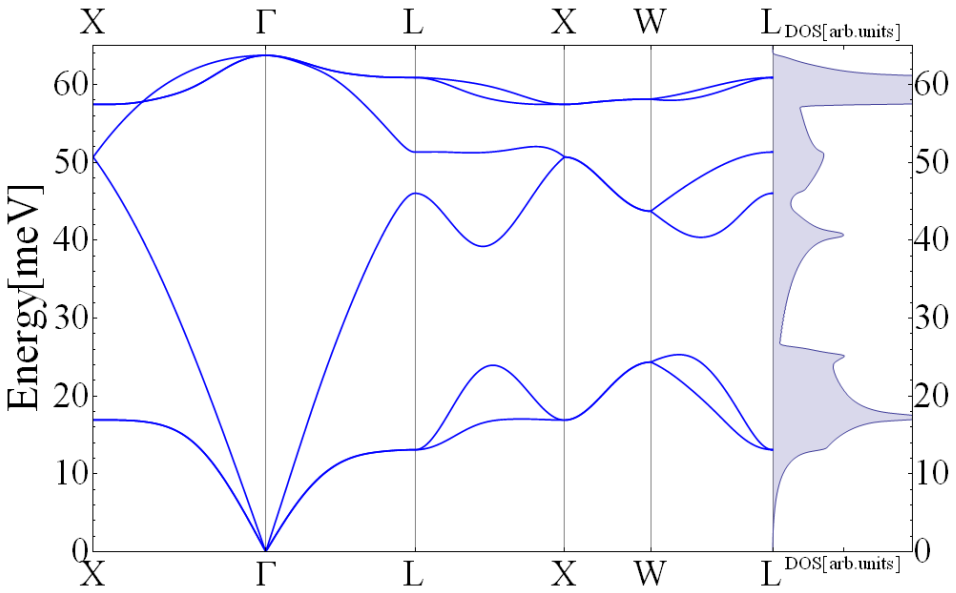


Figure 4.47: Dispersion relation and phonon density of states of natural Si.

shifted down to lower energies with increasing the mass, whereas the higher energies are shifted more strongly than the lower energies. Hence, one can expect that at an interface between two different Si crystals with different isotopes the high energy phonons are stronger affected than the low energy phonons.

To get an idea of the different contributions to the heat conduction of each energy at different temperatures the integrand of equation (2.42) is shown in Fig. 4.49. At around 100K mainly the low energy phonons contribute to the thermal conduction. At 300K nearly all phonons have a significant contribution to the heat conduction. Increasing the temperature further keeps the contribution of the low energy phonons nearly constant but still increases the contribution of the high energy phonons.

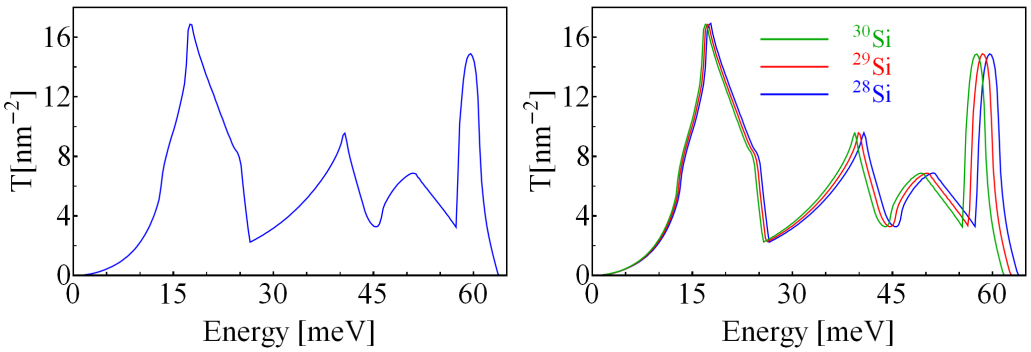


Figure 4.48: Left: Transmission function of natural Si. Right: Transmission functions of the different Si isotopes.

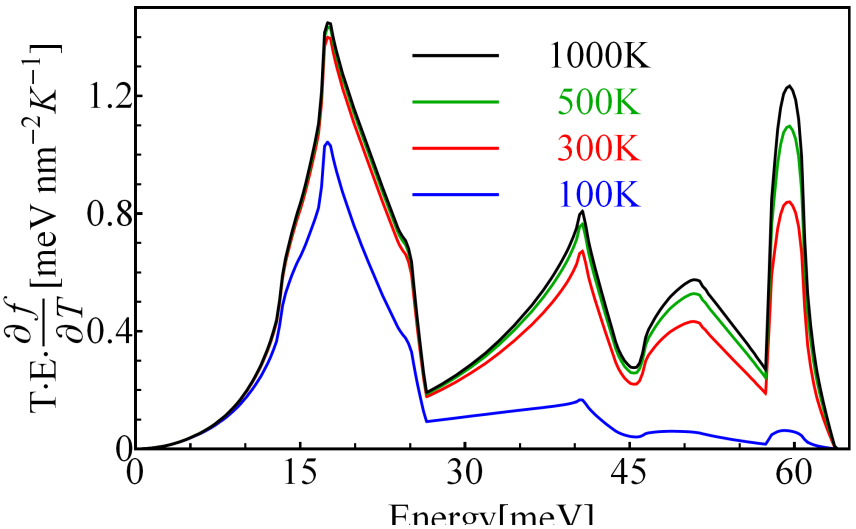


Figure 4.49: Transmission function times phonon energy times distribution function for different temperatures. Note that these curves are the integrand in equation (2.42). Therefore the area under the curves are corresponding thermal conductivities.

### 4.3.1 Isotope Superlattices

In this section the thermal conductance of isotope superlattices are investigated. Fig. 4.50 shows the principle setting. Two natural silicon contacts are connected by an isotope superlattice. In the first setting a periodic arrangement of the layer thickness is considered. One period consists of two layers with different isotopes. Each of theses layers consists of 76 atomic monolayers, which correspond to a thickness of approximately 10nm. Therefore the length of one period is 20nm. In the second setting the length of each layers varies randomly between 5nm and 15nm, which corresponds to 40 atoms and 112 atoms, respectively. Two different combinations of isotopes are investigated $^{28}$Si/$^{29}$Si and $^{28}$Si/$^{30}$Si.

### 4.3.2 $^{28}$Si/$^{29}$Si

Fig. 4.51 shows the transmission functions for different period numbers with a periodic arrangement (left panel) and with a random arrangement (right panel). In both cases the transmission function is reduced due to the superlattice, and the effect is the strongest on the high energy phonons. In the case of the periodic arrangement the effect of the superlattice seems to saturate with 8 periods. Increasing the number of periods further does not have any significant effect on the transmission function.

At this point the transmission functions for the random arrangement shows a different behavior. Increasing the number of periods leads to a reduction of the transmission function without showing a saturation.

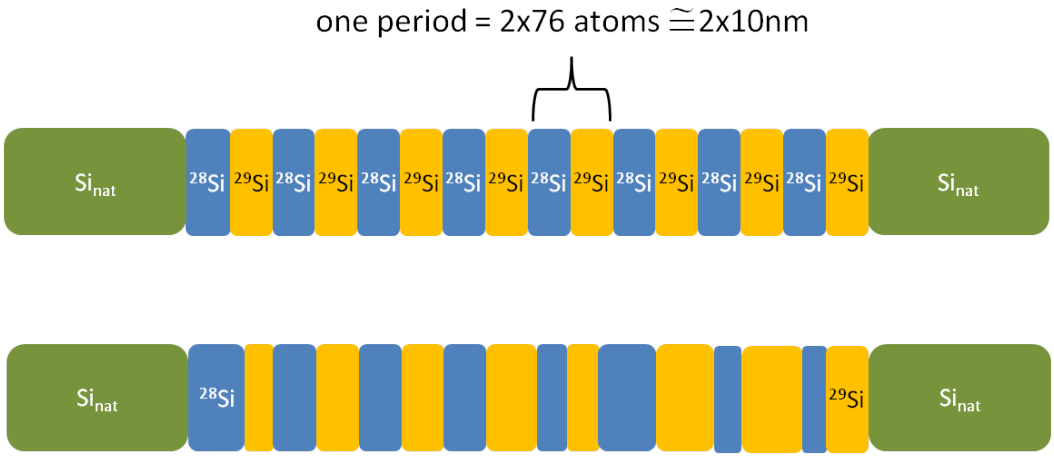


Figure 4.50: Sketch of the systems under consideration. Two silicon contacts with natural Si are connected by a superlattice of $^{28}$Si/$^{29}$Si. Top: Periodic arrangement. Bottom: Random arrangement.

The corresponding resistance for the periodic and random arrangement are shown in Fig. 4.52. The resistance for the periodic arrangement saturates at 8 periods and can not be increased further by increasing the number of periods. The resistance for the random arrangement on the other hand increases further with increasing the number of periods. For comparison the resistance obtained with equation (2.189) is also shown. Equation (2.189) requires that the transmission function at each period is combined completely incoherently. Hence, the resistance obtained with equation (2.189) compared to the coherent resistance in the periodic and random arrangement shows the difference between the completely coherent and completely incoherent case. Therefore the resistance obtained with equation (2.189) is the maximum contribution of the resistance due to the mass difference if other incoherent scattering effects are present.

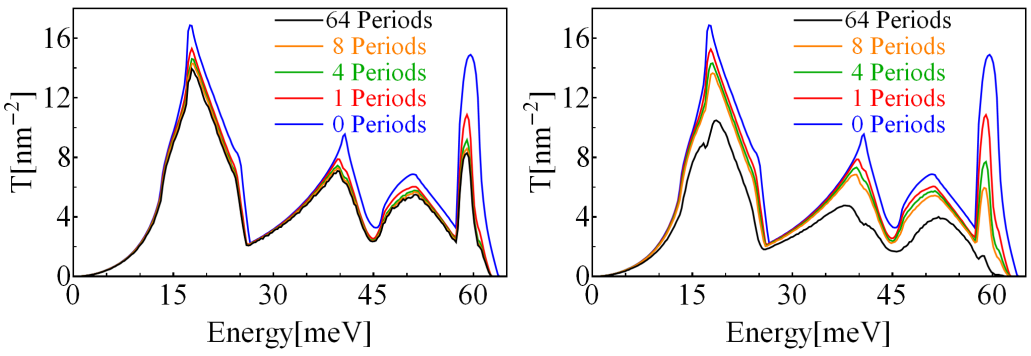


Figure 4.51: Transmission function of $^{28}$Si/$^{29}$Si superlattices for different number of periods. Left: Periodic arrangement. Right: Random arrangement.

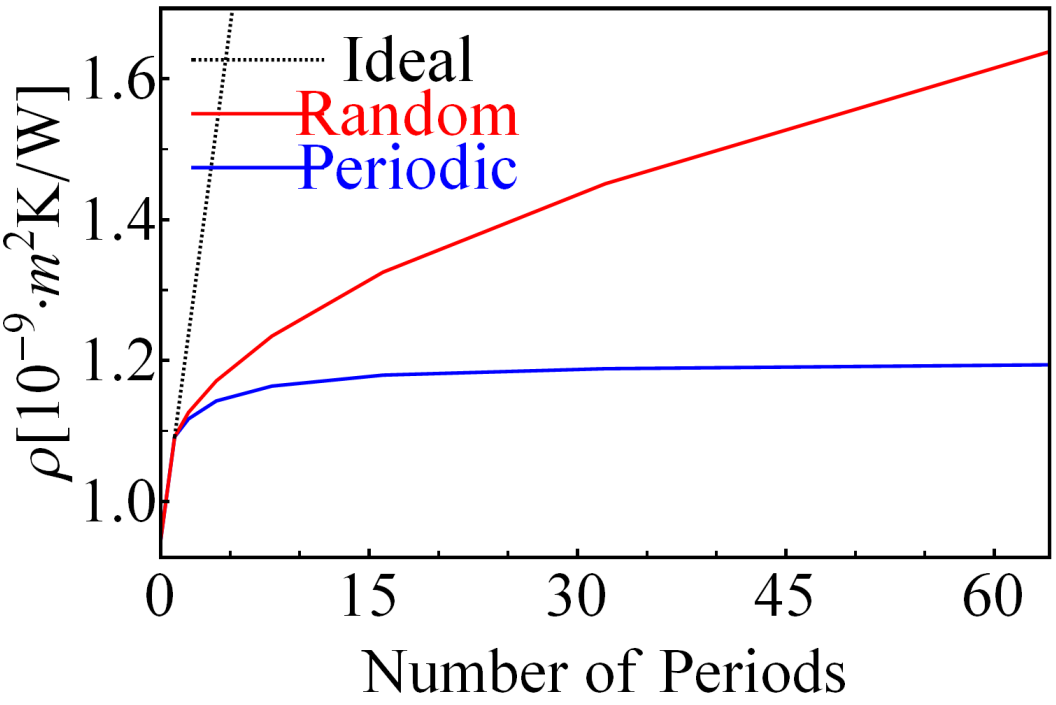


Figure 4.52: Thermal phonon resistance vs. number of periods for the periodic and random arrangement for for $^{28}Si/^{29}Si$ superlattices at 300K.

### 4.3.3 $^{28}Si/^{30}Si$

Fig. 4.53 shows the transmission functions for different period numbers with a periodic arrangement (left panel) and with a random arrangement (right panel). For comparison the resistance obtained with equation (2.189) is also shown. The discussed about the resistance obtained with equation (2.189) is given in the previous section. In general, the behavior is the same like in the case of the $^{28}Si/^{29}Si$ superlattice. The only difference is, that in the case of the $^{28}Si/^{30}Si$ lattice the reduction is stronger compared to the $^{28}Si/^{29}Si$ superlattice. This is not surprising since the mass differences between $^{28}Si/^{30}Si$ is a factor of two higher than the differences in mass between $^{28}Si/^{29}Si$. The resistances for the $^{28}Si/^{30}Si$ superlattices are shown in Fig. 4.54. Also in this case for the periodic arrangement the resistance saturates at 8 periods, whereas in the random arrangement the resistance increases with increasing the number of periods. Compared to the superlattice $^{28}Si/^{29}Si$ the resistance is higher by a factor of approximately 1.3.

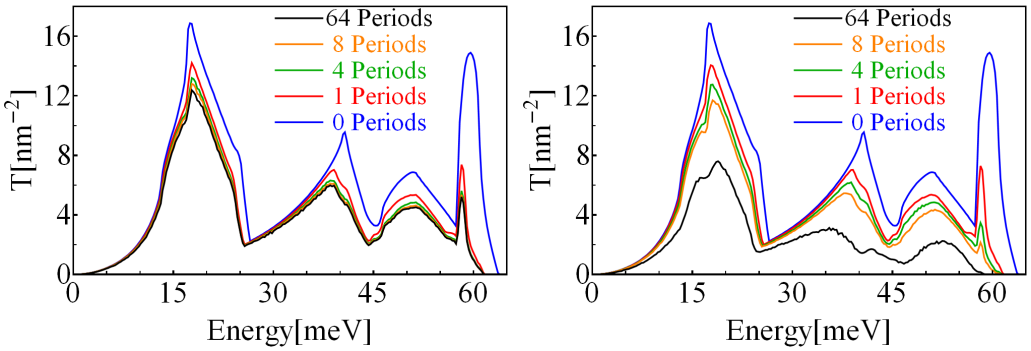


Figure 4.53: Transmission function of $^{28}$Si/$^{30}$Si superlattices for different number of periods. Top: Periodic arrangement. Bottom: Random arrangement.

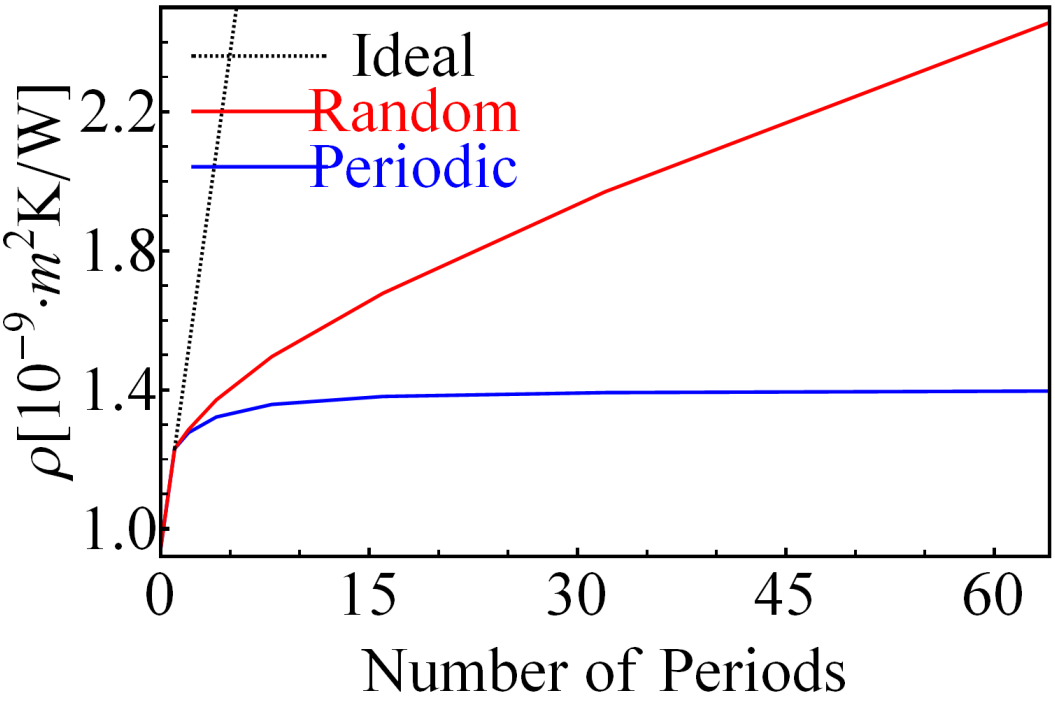


Figure 4.54: Thermal phonon resistance vs. number of periods for the periodic and random arrangement for $^{28}$Si/$^{30}$Si superlattices at 300K.

### 4.3.4 Discussion phonon scattering in isotope Si superlattices

The results obtained here differ from the results presented in reference [80]. For $^{28}Si/^{30}Si$ the reported transmission probability is 5% for 64 periods. A transmission propability of 5% means an increase in the resistance of a factor of 20. The relative increase in the resistance for the random arrangement for the $^{28}Si/^{30}Si$ superlattices calculated with the phonon model is only 2.5 at 64 periods. The resistance obtained in the incoherently combined case is a factor of 20 higher. Hence, the model used in reference [80] describes the effect of completely incoherently combined interfaces and agree well with our results obtained with equation (2.189). The results of the periodic arrangement show a total different behavior compared to the results presented in reference [80]. In reference [80] the transmission probability tend to zero with increasing the number of periods, which means that the resistance could in principle increase to infinity, whereas the results presented in this work for a periodic arrangement show a maximum increase of the resistance of 40%. The saturation of the resistance is quite surprising and can be explained with the existance of blochstates, which are known from electronic systems in a periodic lattices. Blochstates are the eigenstates of these periodic lattices and can therefore pass through the periodic lattice without beeing scattered. Considering again the setting shown in Fig. 4.50 this means that in the periodic arrangement the phonons get only scattered when they enter the superlattice from the contanct and when they leave the superlattice into the other contanct. Hence in the periodic arrangment there are basically only two effective interfaces at which the phonons can scatter. The transmission propability is therefore independent of the number of periods as long as there are enough periods that bloch states arise. In the particular presented case it was found that 8 periods are enough to establish this behavior.

# 5 Summary

To estimate the thermoelectric usability of a material system one has to determine the thermoelectric parameters of the material system. These material parameters can be divided into the electronic parameters, which are the Seebeck coefficient $S$, the electric conductivity $\sigma$, and the thermal conductivity of the electrons $\kappa_e$, and into the lattice parameter, which is the thermal conductivity of the phonons $\kappa_p$.

In this work methods have been developed to calculate the different thermoelectric parameters of nanostructured materials. For the electronic parameters a model has been developed that describes electron transport in nanograined materials, which models the grain boundary by so called double Schottky barriers. For the lattice parameter a model has been developed that can calculate coherent phonon transport across different nanostructures.

In chapter 4.2 the electronic parameters of a typical nanograined semiconductor are investigated. It is widely believed that in such structures the electronic parameters can in principle benefit from an energy filtering effect, which is caused by a so called double Schottky barrier [15, 74]. It is furthermore believed that this effect can enhance the thermoelectric efficiency. In chapter 4.2 it was shown that such an energy filtering effect can indeed increase the thermoelectric efficiency if the barrier height is close to the chemical potential. However, for the double Schottky barrier model it was found that this energy filtering effect does not occur at reasonable chemical potentials, since for reasonable chemical potentials the Schottky barrier becomes too small to have an effect on the electronic parameters. Since the vanishing of the double Schottky barrier with increasing the chemical potential is a fundamental mechanism, one can conclude that in reasonable thermoelectric materials a double Schottky barrier has no effect on the thermoelectric properties. Although a double Schottky barrier can not lead to an energy filtering effect in reasonable thermoelectric materials, this does not exclude that other energy depended scattering mechanisms can occur. One approach to investigate such scattering mechanisms could be to model the grain boundary on an atomistic scale using an *ab initio* method or a parameter based method like a tight-binding model. Based on these models transport calculations can then be performed. The preferred transport model in this case would be the Landauer formalism.

In chapter 4.1 the thermal conductivity of the phonons $\kappa_p$ of ZnO/ZnS-based systems is investigated. It is found that regardless of the specific structure ZnO/ZnS-based systems exhibits a strong phonon scattering. Here two different methods of combing ZnO and ZnS are considered: $ZnO_xS_{1-x}$ alloys and ZnO/ZnS interfaces. It is shown that if the interfaces are combined incoherently the figure of merit increases with increasing the number of interfaces. An incoherent combination of the interfaces is justified if the phonon-phonon scattering between the interfaces is strong enough and if the distance between the interfaces is on the order of the mean free path of the phonons.

To estimate the potential of ZnO/ZnS-based materials for applications Fig. 5.55 shows the thermal conductivity of the phonons for different interface densities for the incoherent case. At an interface density of $50/\mu m$ the thermal conductivity has a value of 4W/mK. Such low thermal conductivities are experimentally observed in ZnAlGaO composites [22], which have a thermal conductivity of 5W/mK and a zT value exceeding 0.65 at 1247K.

Of course in the latter considerations only the lattice part of the thermal conductivity is taken into account, which is correct as long as the electronic part of the thermal conductivity is small against the lattice part. An estimation of the electronic part of the thermal conductivity can be obtained from chapter 4.2. The electronic contribution to the thermal conductivity for moderate chemical potentials is about 0.2W/mK at 300K. Hence, the lattice contribution is indeed much higher than the electronic contribution. The results concerning the thermal conductivity in ZnO/ZnS-based materials are quite promising for thermoelectric applications. In this work it is shown that the thermal conductivity in these structures can be in principle reduced compared to the individual bulk values. The reduction in the thermal conductivity can lead to an increase in the efficiency if the electronic parameters of ZnO/ZnS-based materials have also reasonable values. In this work the diffusive mismatch model is employed to calculate the interface conductance. The diffusive mismatch model gives an approximation of the real interface conductance. The calculation of the real interface conductance is in principle also possible with the methods developed in this work, but requires high computational effort. Because of the high progress in the computer technology, the investigation of real interfaces will be possible within a reasonable framework and therefore an interesting task for the future.

To estimate the differences between a coherent and incoherent treatment of phonon scattering at interfaces a computational easy handleable material system is considered in chapter 4.3. In particular, coherent phonon scattering in an isotope Si superlattice is investigated. The central conclusion of these investigations is that the resistivity obtained in the coherent treatment is smaller than in the incoherent treatment. Furthermore, it was shown that the resistivity in the coherent case depends in the actual arrangement of the interfaces. In the periodic arrangement the resistivity saturates at fairly low numbers of interfaces, whereas in the random arrangement the resistivity shows a linear dependence with the number of interfaces. Nevertheless, the slope in the random arrangement is much smaller than the slope obtained in the incoherently combined interfaces. From the presented results it is not possible to estimate the scattering strength that is necessary to have an incoherent combination of the interfaces. Also interesting would be the impact of the transmission function on the actual arrangement of the interfaces and the search for an optimal arrangement that leads to the highest resistivity. These questions are interesting problems, which are worth to be investigated in the future.

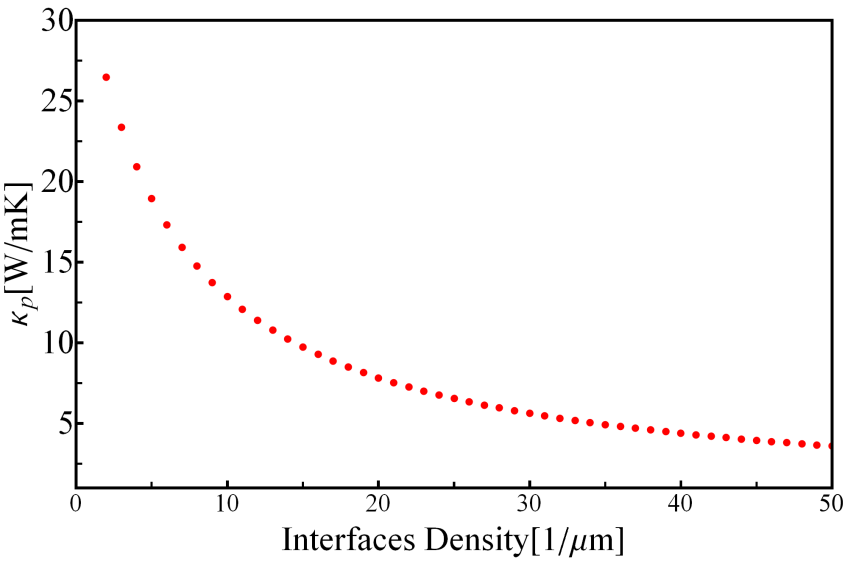


Figure 5.55: Thermal conductivity vs. interface density. The bulk conductivities are taken from chapter 4.1. For the interface conductance the value $0.2 \cdot 10^9$W/mK is used, which is the average interface conductance obtained in chapter 4.1.

# 6 Appendix

## 6.1 Computational effort: quantum mechanical treatment vs. classical treatment of phonons

In section 2.3.1.1 it was mentioned that the classical treatment of the phonons is preferred to the quantum mechanical treatment, because of the higher computational effort that comes along with the quantum mechanical treatment. This statement will be discussed in this section in detail. Considering again the Hamilton operator for phonons for N-Atoms in the harmonic approach. If translation symmetries can not simplify this problem, then the corresponding SGL has $D \cdot N_A$ coupled variables, where $N_A$ is the number of atoms and $D$ is the dimension of the system. In the FDM representation the corresponding matrices have therefore the dimension $N_P^{D \cdot N_A}$, where $N_P$ are the number of points in real space. In the classical treatment no FDM is needed, since Newton's laws define a set of linear equations that can be described by a matrix of dimension $D \cdot N_A$.

As an example for a quantum mechanical solutions a system with two atoms that is connected to a wall is considered. The corresponding Hamiltonian in real space representation is

$$H = \frac{\hbar^2}{2m}\left(\frac{d^2}{dx_1^2} + \frac{d^2}{dx_2^2}\right) + \frac{k_1}{2}(x_1 - d_1)^2 + \frac{k_2}{2}(x_1 - x_2 - d_2)^2. \tag{6.219}$$

Fig. 6.56 shows a sketch of this system and the eigenvalues of the system. In Fig. 6.57 wave function of the ground state and an exited state are shown. The parameter used here are $m = m_0$, $k_1 = 10k_2 = 4 \cdot 2500\frac{eV}{nm^2}$, and $d_1 = d_2 = \frac{1}{3}nm$. The number of grid points in real space $N_P$ is 50. This means that the results shown here are obtained by calculating the eigensystem of a matrix with dimension 2500. The computational effort for this calculation is approximately several minutes on one cpu core.

The classical solution of the problem is given by the eigenvectors of the matrix

$$\begin{pmatrix} m\omega^2 + k_1 + k_2 & -k_2 \\ -k_2 & m\omega^2 + k_2 \end{pmatrix}. \tag{6.220}$$

The eigenvectors and eigenvalues of this matrix can be obtain within milliseconds, which is much fast than in the quantum mechanical case.

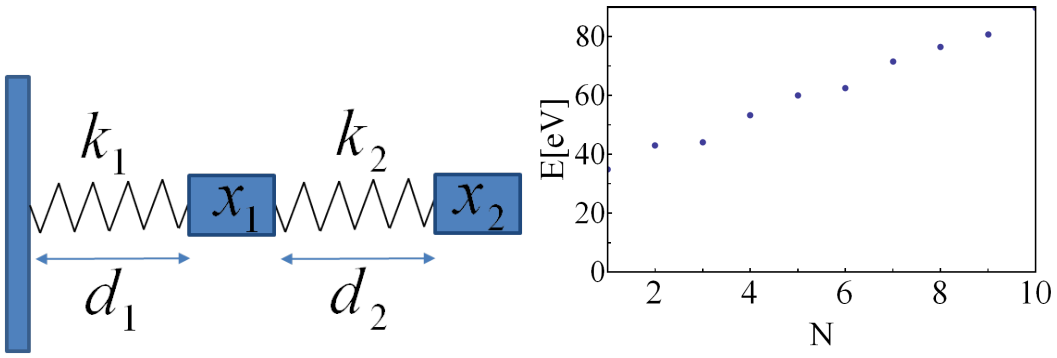


Figure 6.56: Sketch of the system (left) and the first eigenvalues of the system (right).

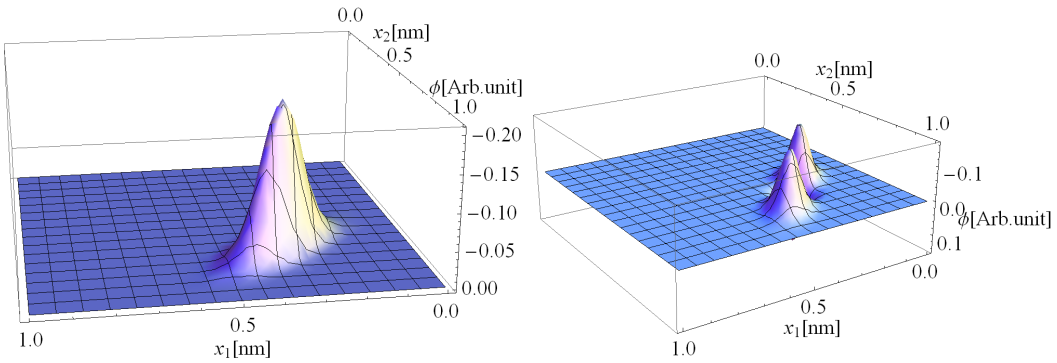


Figure 6.57: Ground state wave function (left) and wave function of an exited state (right).

## 6.2 Derivation of the transmission function in the the DMM

Starting point is equation (1) from reference [21] for the interface conductance,

$$G = \frac{1}{2(2\pi)^3} \sum_i \int_k \frac{1}{k_b T^2} \alpha_{A\to B}(k,i) \cdot (\hbar\omega(k,i))^2 \\ |V(k,i)\cdot n| \frac{\exp\left(\frac{\hbar\omega(k,i))}{k_b T}\right)}{\left(\exp\left(\frac{\hbar\omega(k,i))}{k_b T}\right)-1\right)^2} dk. \tag{6.221}$$

G is the conductance between interface A and B. $\alpha_{A\to B}(k,i)$ is the transmission probability of mode i with vector k from A to B. $\hbar\omega(k,i)$ is the phonon frequency and $V(k,i)\cdot n$ the group velocity in direction of the normal to the interface. According to [21] the transmission probability $\alpha_{A\to B}(k,i)$ in the DMM is

$$\alpha_{A\to B}(\omega') = \\ \frac{\Delta K_B \sum_{j,k} |V(k,j)\cdot n| \, \delta_{\omega(k,j),\omega'}}{\Delta K_B \sum_{j,k} |V(k,j)\cdot n| \, \delta_{\omega(k,j),\omega'} + \Delta K_A \sum_{j,k} |V(k,j)\cdot n| \, \delta_{\omega(k,j),\omega'}}. \tag{6.222}$$

$\Delta K_A$ and $\Delta K_B$ are the volumes of the discretized cells of the corresponding Brillouin zones. In order to link the bulk transmission functions obtained from equation (2.42) to the conductance given in equation (6.221) one can set $\alpha_{A\to B}(k,i) = 1$ and write the conductance as an integral over $\omega$ and we obtain

$$G = \frac{1}{2(2\pi)^3} \int d\omega' \cdot \hbar\omega' \frac{df(\hbar\omega', T)}{dT} \\ \sum_i \int_k |V(k,i)\cdot n| \, \delta_{\omega(k,i),\omega'} dk. \tag{6.223}$$

Comparing the conductance in equation (2.42) with the conductance in equation (6.223) one can identify

$$\frac{1}{2(2\pi)^2} \sum_j \int_k |V(k,j)\cdot n| \, \delta_{\omega(k,j),\omega'} dk \tag{6.224}$$

as the bulk transmission function $t(\omega')$ from equation 2.42. Thus equation (6.222) can be expressed in terms of transmission functions

$$\alpha_{A\to B}(\omega) = \frac{t_b(\omega)}{t_a(\omega) + t_b(\omega)}, \tag{6.225}$$

where $t_a(\omega)$ and $t_b(\omega)$ are the bulk transmission functions of material a and b respectively. Using

$$\frac{df(\hbar\omega,T)}{dT} = \frac{\exp\left(\frac{\hbar\omega}{k_bT}\right)}{\left(\exp\left(\frac{\hbar\omega}{k_bT}\right)-1\right)^2}\cdot\frac{\hbar\omega}{k_bT^2} \tag{6.226}$$

equation 6.221 can be rewritten to

$$\begin{aligned} G = \frac{1}{2(2\pi)^3}\sum_i \int_k \alpha_{A\to B}(\omega(k,i))\cdot\hbar\omega(k,i) \\ \frac{df(\hbar\omega(k,i),T)}{dT}\left|V(k,i)\cdot n\right| dk \end{aligned} \tag{6.227}$$

This can be written as an integral over $\omega$

$$\begin{aligned} G = \frac{1}{2(2\pi)^3}\int d\omega' \alpha_{A\to B}(\omega')\cdot\hbar\omega'\frac{df(\hbar\omega',T)}{dT} \\ \sum_i \int_k \left|V(k,i)\cdot n\right| \delta_{\omega(k,i),\omega'} dk. \end{aligned} \tag{6.228}$$

Using again expression (6.224) one obtains for the conductance

$$G = \frac{1}{2\pi}\int d\omega' \alpha_{A\to B}(\omega')\cdot\hbar\omega'\frac{df(\hbar\omega',T)}{dT}t_a(\omega'), \tag{6.229}$$

which can be expressed in the Landauer form

$$G = \frac{1}{2\pi}\int d\omega'\cdot\hbar\omega'\frac{df(\hbar\omega',T)}{dT}t(\omega') \tag{6.230}$$

with

$$t(\omega) = \frac{t_a(\omega)t_b(\omega)}{t_a(\omega)+t_b(\omega)}. \tag{6.231}$$

$t_a(\omega)$ and $t_b(\omega)$ are the bulk transmission functions.

# References


[1] **Werner Heisenberg**. *Physik und Philosophie*. 7 Aufl. Hirzel (2006).

[2] **International Energy Agency**. *Key World Energy Statistics* (2011). URL http://www.iea.org/textbase/nppdf/free/2011/key_world_energy_stats.pdf.

[3] **Kornelius Nielsch**, **Julien Bachmann**, **Johannes Kimling**, **Harald Böttner**. *Thermoelectric Nanostructures: From Physical Model Systems towards Nanograined Composites*. Advanced Energy Materials, 1 (5): 713–731 (2011). ISSN 1614-6840. URL http://dx.doi.org/10.1002/aenm.201100207.

[4] **Len A. Fisk**. *Journey into the Unknown Beyond*. Science, 309 (5743): 2016–2017 (2005). http://www.sciencemag.org/content/309/5743/2016.full.pdf, URL http://www.sciencemag.org/content/309/5743/2016.abstract.

[5] **K Matsubara**. *Development of a high efficient thermoelectric stack for a waste exhaust heat recovery of vehicles*. Thermoelectrics, 2002. Proceedings ICT '02. Twenty-First International Conference on, 25-29: 418–425 (2002).

[6] **D. Champier**, **J.P. Bédécarrats**, **T. Kousksou**, **M. Rivaletto**, **F. Strub**, **P. Pignolet**. *Study of a TE (thermoelectric) generator incorporated in a multifunction wood stove*. Energy, 36 (3): 1518 – 1526 (2011). ISSN 0360-5442. URL http://www.sciencedirect.com/science/article/pii/S0360544211000132.

[7] **David Salerno**. *Ultralow Voltage Energy Harvester Uses Thermoelectric Generator for Battery-Free Wireless Sensors*. Linear Technology Journal of Analog Innovation, 20 (3): 2 (2008).

[8] **G. Jeffrey Snyder**, **Eric S. Toberer**. *Complex thermoelectric materials*. Nature Materials, 7: 105–114 (2008).

[9] **M. Jonson**, **G. D. Mahan**. *Mott's formula for the thermopower and the Wiedemann-Franz law*. Phys. Rev. B, 21: 4223–4229 (May 1980). URL http://link.aps.org/doi/10.1103/PhysRevB.21.4223.

[10] **Cronin B. Vining**. *An inconvenient truth about thermoelectrics*. Nature Materials, 8: 83–85 (2009).

[11] **R. Venkatasubramanian**, **E. Siivola**, **T. Colpitts**, **B. O'Quinn**. *Thin-film thermoelectric devices with high room-temperature figures of merit*. Nature, 413: 597–602 (2001).

[12] **Biplab Paul**, **Ajay Kumar V**, **P. Banerji**. *Embedded Ag-rich nanodots in PbTe: Enhancement of thermoelectric properties through energy filtering of the carriers.* Journal of Applied Physics, 108 (6): 064322 (S. 5) (2010). URL http://link.aip.org/link/?JAP/108/064322/1.

[13] **Sergey V. Faleev**, **Fran çois Léonard**. *Theory of enhancement of thermoelectric properties of materials with nanoinclusions.* Phys. Rev. B, 77: 214 304 (Jun 2008). URL http://link.aps.org/doi/10.1103/PhysRevB.77.214304.

[14] **J. Martin**, **Li Wang**, **Lidong Chen**, **G. S. Nolas**. *Enhanced Seebeck coefficient through energy-barrier scattering in PbTe nanocomposites.* Phys. Rev. B, 79: 115 311 (Mar 2009). URL http://link.aps.org/doi/10.1103/PhysRevB.79.115311.

[15] **A. Popescu**, **L. M. Woods**, **J. Martin**, **G. S. Nolas**. *Model of transport properties of thermoelectric nanocomposite materials.* Phys. Rev. B, 79: 205 302 (May 2009). URL http://link.aps.org/doi/10.1103/PhysRevB.79.205302.

[16] **Kengo Kishimoto**, **Tsuyoshi Koyanagi**. *Preparation of sintered degenerate n-type PbTe with a small grain size and its thermoelectric properties.* Journal of Applied Physics, 92 (5): 2544–2549 (2002). URL http://link.aip.org/link/?JAP/92/2544/1.

[17] **L. D. Hicks**, **M. S. Dresselhaus**. *Effect of quantum-well structures on the thermoelectric figure of merit.* Phys. Rev. B, 47: 12 727–12 731 (May 1993). URL http://link.aps.org/doi/10.1103/PhysRevB.47.12727.

[18] **M.S. Dresselhaus**, **G. Chen**, **M.Y. Tang**, **R.G. Yang**, **H. Lee**, **D.Z. Wang**, **Z.F. Ren**, **J.-P. Fleurial**, **P. Gogna**. *New Directions for Low-Dimensional Thermoelectric Materials.* Advanced Materials, 19 (8): 1043–1053 (2007). ISSN 1521-4095. URL http://dx.doi.org/10.1002/adma.200600527.

[19] **G. Homm**, **P. J. Klar**. *Thermoelectric materials Compromising between high efficiency and materials abundance.* physica status solidi (RRL) Rapid Research Letters, 5 (9): 324–331 (2011). ISSN 1862-6270. URL http://dx.doi.org/10.1002/pssr.201105084.

[20] **Ü. Özgür**, **Ya. I. Alivov**, **C. Liu**, **A. Teke**, **M. A. Reshchikov**, **S. Doğan**, **V. Avrutin**, **S.-J. Cho**, **H. Morkoç**. *A comprehensive review of ZnO materials and devices.* Journal of Applied Physics, 98 (4): 041301 (S. 103) (2005). URL http://link.aip.org/link/?JAP/98/041301/1.

[21] **Pramod Reddy**, **Kenneth Castelino**, **Arun Majumdar**. *Diffuse mismatch model of thermal boundary conductance using exact phonon dispersion.* Applied Physics Letters, 87 (21): 211908 (S. 3) (2005). URL http://link.aip.org/link/?APL/87/211908/1.

[22] **Michitaka Ohtaki**, **Kazuhiko Araki**, **Kiyoshi Yamamoto**. *High Thermoelectric Performance of Dually Doped ZnO Ceramics.* Journal of Electronic Materials, 38: 1234–1238 (2009). ISSN 0361-5235. 10.1007/s11664-009-0816-1, URL http://dx.doi.org/10.1007/s11664-009-0816-1.

[23] **G. Homm**, **J. Teubert**, **T. Henning**, **P. J. Klar**, **B. Szyszka**. *Seebeck effect of as-grown and micro-structured metallic (Zn,Al)O.* physica status solidi (c), 7 (6): 1602–1604 (2010). ISSN 1610-1642. URL http://dx.doi.org/10.1002/pssc.200983169.

[24] **G. Homm**, **M. Piechotka**, **A. Kronenberger**, **A. Laufer**, **F. Gather**, **D. Hartung**, **C. Heiliger**, **B. Meyer**, **P. Klar**, **S. Steinmüller**, **J. Janek**. *Thermoelectric Measurements on Sputtered ZnO/ZnS Multilayers.* Journal of Electronic Materials, 39: 1504–1509 (2010). ISSN 0361-5235. 10.1007/s11664-010-1293-2, URL http://dx.doi.org/10.1007/s11664-010-1293-2.

[25] **G. Homm**, **S. Petznick**, **F. Gather**, **T. Henning**, **C. Heiliger**, **B. Meyer**, **P. Klar**. *Effect of Interface Regions on the Thermoelectric Properties of Alternating ZnO/ZnO:Al Stripe Structures.* Journal of Electronic Materials, 40: 801–806 (2011). ISSN 0361-5235. 10.1007/s11664-011-1574-4, URL http://dx.doi.org/10.1007/s11664-011-1574-4.

[26] **M. Lundstrom**. *Fundamentals of Carrier Transport.* Cambridge University Press (2009). ISBN 9780521637244. URL http://books.google.de/books?id=Vrkd_dSC3zwC.

[27] **S. Datta**. *Electronic Transport in Mesoscopic Systems.* Cambridge Univeristy Press (1995).

[28] **Datta**. *Atom to Transistor.* Cambridge Univeristy Press (2005).

[29] **Libero J. Bartolotti**, **Ken Flurchick**. *An Introduction to Density Functional Theory*, S. 187–216. John Wiley & Sons, Inc. (2007). ISBN 9780470125847. URL http://dx.doi.org/10.1002/9780470125847.ch4.

[30] **N. Mingo**, **Liu Yang**. *Phonon transport in nanowires coated with an amorphous material: An atomistic Green's function approach.* Phys. Rev. B, 68 (24): 245 406 (Dec 2003).

[31] **W. Zhang**, **T.S. Fisher**, **N. Mingo**. *The Atomistic Green's Function Method: An Efficient Simulation Approach for Nanoscale Phonon Transport*. Numerical Heat Transfer, Part B: Fundamentals: An International Journal of Computation and Methodology, 51: 333 (2007).

[32] **W. Zhang**, **T. S. Fisher**, **N. Mingo**. *Simulation of Interfacial Phonon Transport in Si–Ge Heterostructures Using an Atomistic Green's Function Method*. Journal of Heat Transfer, 129 (4): 483–491 (2007). URL `http://link.aip.org/link/?JHR/129/483/1`.

[33] **Christophe Goupil**, **Wolfgang Seifert**, **Knud Zabrocki**, **Eckhart Müller**, **G. Jeffrey Snyder**. *Thermodynamics of Thermoelectric Phenomena and Applications*. Entropy, 13 (8): 1481–1517 (2011). ISSN 1099-4300. URL `http://www.mdpi.com/1099-4300/13/8/1481/`.

[34] **W. Seifert**, **M. Ueltzen**, **E. Müller**. *One-dimensional Modelling of Thermoelectric Cooling*. physica status solidi (a), 194 (1): 277–290 (2002). ISSN 1521-396X. URL `http://dx.doi.org/10.1002/1521-396X(200211)194:1<277::AID-PSSA277>3.0.CO;2-5`.

[35] **Changwook Jeong**, **Raseong Kim**, **Mathieu Luisier**, **Supriyo Datta**, **Mark Lundstrom**. *On Landauer versus Boltzmann and full band versus effective mass evaluation of thermoelectric transport coefficients*. Journal of Applied Physics, 107 (2): 023707 (S. 7) (2010). URL `http://link.aip.org/link/?JAP/107/023707/1`.

[36] **Czycholl**. *Theoretische Festkörper Physik*. Springer (2008).

[37] **Dario Alfè**. *PHON: A program to calculate phonons using the small displacement method*. Computer Physics Communications, 180 (12): 2622–2633 (2009).

[38] **J.Furthmüller G. Kresse**, **J. Hafner**. *Ab initio Force Constant Approach to Phonon Dispersion Relations of Diamond and Graphite*. Euroühys. Lett., 32: 729 (1995).

[39] **Xavier Gonze**, **Changyol Lee**. *Dynamical matrices, Born effective charges, dielectric permittivity tensors, and interatomic force constants from density-functional perturbation theory*. Phys. Rev. B, 55: 10 355–10 368 (Apr 1997). URL `http://link.aps.org/doi/10.1103/PhysRevB.55.10355`.

[40] **S. Baroni**, **P. Giannozzi**. *Thermal Properties of Materials from Ab Initio Quasi-Harmonic Phonons*. Miner. & Geochem., 71 (2009).

[41] **Xavier Gonze**. *Adiabatic density-functional perturbation theory*. Phys. Rev. A, 52: 1096–1114 (Aug 1995). URL `http://link.aps.org/doi/10.1103/PhysRevA.52.1096`.

[42] **Xavier Gonze**. *First-principles responses of solids to atomic displacements and homogeneous electric fields: Implementation of a conjugate-gradient algorithm*. Phys. Rev. B, 55: 10 337–10 354 (Apr 1997). URL http://link.aps.org/doi/10.1103/PhysRevB.55.10337.

[43] **F. Guinea**, **C. Tejedor**, **F. Flores**, **E. Louis**. *Effective two-dimensional Hamiltonian at surfaces*. Phys. Rev. B, 28 (8): 4397–4402 (Oct 1983).

[44] **Yong Xu**, **Jian-Sheng Wang**, **Wenhui Duan**, **Bing-Lin Gu**, **Baowen Li**. *Nonequilibrium Green's function method for phonon-phonon interactions and ballistic-diffusive thermal transport*. Phys. Rev. B, 78: 224 303 (Dec 2008). URL http://link.aps.org/doi/10.1103/PhysRevB.78.224303.

[45] **John Y. W. Seto**. *The electrical properties of polycrystalline silicon films*. Journal of Applied Physics, 46 (12): 5247–5254 (1975). URL http://link.aip.org/link/?JAP/46/5247/1.

[46] **A. K. Sreedhar**, **S. C. Gupta**. *Electronic Effects in Elastic Constants of PbTe*. Phys. Rev. B, 5: 3160–3164 (Apr 1972). URL http://link.aps.org/doi/10.1103/PhysRevB.5.3160.

[47] **A. B. M. Almamun Ashrafi**, **Akio Ueta**, **Adrian Avramescu**, **Hidekazu Kumano**, **Ikuo Suemune**, **Young-Woo Ok**, **Tae-Yeon Seong**. *Growth and characterization of hypothetical zinc-blende ZnO films on GaAs(001) substrates with ZnS buffer layers*. Applied Physics Letters, 76 (5): 550–552 (2000). URL http://link.aip.org/link/?APL/76/550/1.

[48] **H. Karzel**, **W. Potzel**, **M. Köfferlein**, **W. Schiessl**, **M. Steiner**, **U. Hiller**, **G. M. Kalvius**, **D. W. Mitchell**, **T. P. Das**, **P. Blaha**, **K. Schwarz**, **M. P. Pasternak**. *Lattice dynamics and hyperfine interactions in ZnO and ZnSe at high external pressures*. Phys. Rev. B, 53: 11 425–11 438 (May 1996). URL http://link.aps.org/doi/10.1103/PhysRevB.53.11425.

[49] **J. Serrano**, **A. H. Romero**, **F. J. Manjón**, **R. Lauck**, **M. Cardona**, **A. Rubio**. *Pressure dependence of the lattice dynamics of ZnO: An ab initio approach*. Phys. Rev. B, 69 (9): 094 306 (Mar 2004).

[50] **J. E. Jaffe**, **A. C. Hess**. *Hartree-Fock study of phase changes in ZnO at high pressure*. Phys. Rev. B, 48: 7903–7909 (Sep 1993). URL http://link.aps.org/doi/10.1103/PhysRevB.48.7903.

[51] **John E. Jaffe**, **James A. Snyder**, **Zijing Lin**, **Anthony C. Hess**. *LDA and GGA calculations for high-pressure phase transitions in ZnO and MgO*. Phys. Rev. B, 62: 1660–1665 (Jul 2000). URL http://link.aps.org/doi/10.1103/PhysRevB.62.1660.

[52] **Serge Desgreniers**. *High-density phases of ZnO: Structural and compressive parameters.* Phys. Rev. B, 58: 14 102–14 105 (Dec 1998). URL http://link.aps.org/doi/10.1103/PhysRevB.58.14102.

[53] **Mitsutake Oshikiri**, **Ferdi Aryasetiawan**. *Band gaps and quasiparticle energy calculations on ZnO, ZnS, and ZnSe in the zinc-blende structure by the GW approximation.* Phys. Rev. B, 60: 10 754–10 757 (Oct 1999). URL http://link.aps.org/doi/10.1103/PhysRevB.60.10754.

[54] **G. Z. Shen**, **Y. Bando**, **J. Q. Hu**, **D. Golberg**. *High-symmetry ZnS hepta- and tetrapods composed of assembled ZnS nanowire arrays.* Applied Physics Letters, 90 (12): 123101 (S. 3) (2007). URL http://link.aip.org/link/?APL/90/123101/1.

[55] **Tetsuya Yamamoto**, **Seiichi Kishimoto**, **Seishi Iida**. *Control of valence states for ZnS by triple-codoping method.* Physica B: Condensed Matter, 308 (0): 916 (2001). ISSN 0921-4526. International Conference on Defects in Semiconductors, URL http://www.sciencedirect.com/science/article/pii/S0921452601008420.

[56] **A. Mujica**, **Angel Rubio**, **A. Muñoz**, **R. J. Needs**. *High-pressure phases of group-IV, III˘V, and II˘VI compounds.* Rev. Mod. Phys., 75: 863–912 (Jul 2003). URL http://link.aps.org/doi/10.1103/RevModPhys.75.863.

[57] **Y. C. Cheng**, **C. Q. Jin**, **F. Gao**, **X. L. Wu**, **W. Zhong**, **S. H. Li**, **Paul K. Chu**. *Raman scattering study of zinc blende and wurtzite ZnS.* Journal of Applied Physics, 106 (12): 123505 (S. 5) (2009). URL http://link.aip.org/link/?JAP/106/123505/1.

[58] **E. H. Kisi**, **M. M. Elcombe**. *u parameters for the wurtzite structure of ZnS and ZnO using powder neutron diffraction.* Acta Crystallographica Section C, 45 (12): 1867–1870 (Dec 1989). URL http://dx.doi.org/10.1107/S0108270189004269.

[59] **J. T. S. Aswegen**, **H. Verleger**. *Röntgenographische Untersuchung des Systems ZnS FeS.* Naturwissenschaften, 47: 131–131 (1960). ISSN 0028-1042. 10.1007/BF00628510, URL http://dx.doi.org/10.1007/BF00628510.

[60] **C. Jacoboni**, **C. Canali**, **G. Ottaviani**, **A. Alberigi Quaranta**. *A review of some charge transport properties of silicon.* Solid-State Electronics, 20 (2): 77 – 89 (1977). ISSN 0038-1101. URL http://www.sciencedirect.com/science/article/pii/0038110177900545.

[61] **Glen A. Slack**, **Moayyed A. Hussain**. *The maximum possible conversion efficiency of silicon-germanium thermoelectric generators.* Journal of

Applied Physics, 70 (5): 2694–2718 (1991). URL http://link.aip.org/link/?JAP/70/2694/1.

[62] **C. J. Glassbrenner**, **Glen A. Slack**. *Thermal Conductivity of Silicon and Germanium from 3°K to the Melting Point*. Phys. Rev., 134: A1058–A1069 (May 1964). URL http://link.aps.org/doi/10.1103/PhysRev.134.A1058.

[63] **Jamil Tahir-Kheli Jen-Kan Yu William A. Goddard Akram I. Boukai, Yuri Bunimovich**, **James R. Heath**. *Silicon nanowires as efficient thermoelectric materials*. Nature, S. 168–171 (2008).

[64] **C.P. Herrero**. *Dependence of the silicon lattice constant on isotopic mass*. Solid State Communications, 110 (5): 243 – 246 (1999). ISSN 0038-1098. URL http://www.sciencedirect.com/science/article/pii/S0038109899000824.

[65] **Xuejun Zhu**, **S. Fahy**, **Steven G. Louie**. *Ab initio calculation of pressure coefficients of band gaps of silicon: Comparison of the local-density approximation and quasiparticle results*. Phys. Rev. B, 39: 7840–7847 (Apr 1989). URL http://link.aps.org/doi/10.1103/PhysRevB.39.7840.

[66] **J. H. Parker**, **D. W. Feldman**, **M. Ashkin**. *Raman Scattering by Silicon and Germanium*. Phys. Rev., 155: 712–714 (Mar 1967). URL http://link.aps.org/doi/10.1103/PhysRev.155.712.

[67] **E. T. Swartz**, **R. O. Pohl**. *Thermal boundary resistance*. Rev. Mod. Phys., 61 (3): 605–668 (Jul 1989).

[68] **Glen A. Slack**. *Thermal Conductivity of II-VI Compounds and Phonon Scattering by* $Fe^{2+}$ *Impurities*. Phys. Rev. B, 6: 3791–3800 (Nov 1972). URL http://link.aps.org/doi/10.1103/PhysRevB.6.3791.

[69] **Zheng Xing Huang**, **Zhen An Tang**, **Jun Yu**, **Suyuan Bai**. *Thermal conductivity of nanoscale polycrystalline ZnO thin films*. Physica B: Condensed Matter, 406 (4): 818 – 823 (2011). ISSN 0921-4526. URL http://www.sciencedirect.com/science/article/pii/S0921452610011671.

[70] **E. T. Swartz**, **R. O. Pohl**. *Thermal resistance at interfaces*. Applied Physics Letters, 51 (26): 2200–2202 (1987). URL http://link.aip.org/link/?APL/51/2200/1.

[71] **M. N. Touzelbaev**, **P. Zhou**, **R. Venkatasubramanian**, **K. E. Goodson**. *Thermal characterization of Bi2Te3/Sb2Te3 superlattices*. Journal of Applied Physics, 90 (2): 763–767 (2001). URL http://link.aip.org/link/?JAP/90/763/1.

[72] **Yu. I. Ravich**. *CRC Handbook of Thermoelectrics*. CRC Press LLC (1995).

[73] **Daryoosh Vashaee**, **Ali Shakouri**. *Improved Thermoelectric Power Factor in Metal-Based Superlattices*. Phys. Rev. Lett., 92: 106 103 (Mar 2004). URL http://link.aps.org/doi/10.1103/PhysRevLett.92.106103.

[74] **D.L. Medlin**, **G.J. Snyder**. *Interfaces in bulk thermoelectric materials: A review for Current Opinion in Colloid and Interface Science*. Current Opinion in Colloid & Interface Science, 14 (4): 226 – 235 (2009). ISSN 1359-0294. URL http://www.sciencedirect.com/science/article/pii/S1359029409000363.

[75] **J. M. O. Zide**, **D. Vashaee**, **Z. X. Bian**, **G. Zeng**, **J. E. Bowers**, **A. Shakouri**, **A. C. Gossard**. *Demonstration of electron filtering to increase the Seebeck coefficient in* $In_{0.53}Ga_{0.47}As/In_{0.53}Ga_{0.28}Al_{0.19}As$ *superlattices*. Phys. Rev. B, 74: 205 335 (Nov 2006). URL http://link.aps.org/doi/10.1103/PhysRevB.74.205335.

[76] **Joseph P. Heremans**, **Christopher M. Thrush**, **Donald T. Morelli**. *Thermopower enhancement in PbTe with Pb precipitates*. Journal of Applied Physics, 98 (6): 063703 (S. 6) (2005). URL http://link.aip.org/link/?JAP/98/063703/1.

[77] **Joseph P. Heremans**, **Christopher M. Thrush**, **Donald T. Morelli**. *Thermopower enhancement in lead telluride nanostructures*. Phys. Rev. B, 70: 115 334 (Sep 2004). URL http://link.aps.org/doi/10.1103/PhysRevB.70.115334.

[78] **Kengo Kishimoto**, **Kazuo Yamamoto**, **Tsuyoshi Koyanagi**. *Influences of Potential Barrier Scattering on the Thermoelectric Properties of Sintered n-Type PbTe with a Small Grain Size*. Japanese Journal of Applied Physics, 42 (Part 1, No. 2A): 501–508 (2003). URL http://jjap.jsap.jp/link?JJAP/42/501/.

[79] **Giri Joshi**, **Hohyun Lee**, **Yucheng Lan**, **Xiaowei Wang**, **Gaohua Zhu**, **Dezhi Wang**, **Ryan W. Gould**, **Diana C. Cuff**, **Ming Y. Tang**, **Mildred S. Dresselhaus**, **Gang Chen**, **Zhifeng Ren**. *Enhanced Thermoelectric Figure-of-Merit in Nanostructured p-type Silicon Germanium Bulk Alloys*. Nano Letters, 8 (12): 4670–4674 (2008). http://pubs.acs.org/doi/pdf/10.1021/nl8026795, URL http://pubs.acs.org/doi/abs/10.1021/nl8026795.

[80] **G. Bastian**, **A. Vogelsang**, **C. Schiffmann**. *Isotopic Superlattices for Perfect Phonon Reflection*. Journal of Electronic Materials, 39: 1769–

1771 (2010). ISSN 0361-5235. 10.1007/s11664-010-1160-1, URL http://dx.doi.org/10.1007/s11664-010-1160-1.

# List of publications

[E1] **M.Bachmann, M. Czerner, S. Edalati-Boostan, and C.Heiliger**. *Ab initio calculations of phonon transport in ZnO and ZnS*. Eur. Phys. J. B 85: 146 (2012).
URL http://www.springerlink.com/content/j6r30k0q2022081x/.

[E2] **M.Bachmann, M.Czerner, and C.Heiliger**. *Coherent Phonon Scattering in ZnO and ZnS at sulfite and oxygen impurities* Phys. Status Solidi A, (accepted) (2012).

[E3] **M.Bachmann, M.Czerner, and C.Heiliger**. *Ineffectiveness of energy filtering at grain boundaries for thermoelectric materials* Phys. Rev. B, 86, 115320 (2012).
URL http://prb.aps.org/abstract/PRB/v86/i11/e115320/.

[E4] **M.Bachmann, M. Czerner, and C.Heiliger**. *Calculation of Thermoelectric Transport Properties in Heterostructures*. J Electron Mater. 40: 577 (2010).
URL http://www.springerlink.com/content/l1u67k7724h2t325/.

[E5] **M. Czerner, M.Bachmann, and C.Heiliger**. *Spin caloritronics in magnetic tunnel junctions: Ab initio studies*. Phys. Rev. B 83: 132405 (2011) .
URL http://link.aps.org/doi/10.1103/PhysRevB.83.132405/.

[E6] **M.Walter, J. Walowski, V. Zbarsky, M. Münzenberg, M. Schäfers, D. Ebke, G. Reiss, A. Thomas, P. Peretzki, M. Seibt, J. S. Moodera, M. Czerner, M. Bachmann and C. Heiliger**. *Seebeck effect in magnetic tunnel junctions*. Nat. Mater. 10: 742 (2011).
URL http://www.nature.com/nmat/journal/v10/n10/abs/nmat3076.html .

# Acknowledgements

An dieser Stelle möchte ich allen danken die zum Gelingen dieser Arbeit beigetragen haben.
Mein Dank gilt vor allem:

Prof. Dr. Christian Heiliger für die Möglichkeit in seiner Arbeitsgruppe promovieren zu dürfen, sowie für das Vertrauen und die Geduld, welche er mir immer wieder während der durchgehend tolle Betreuung, entgegen gebracht hat.

Prof. Dr. Peter J. Klar für die Begutachtung dieser Arbeit.

Dr. Michael Czerner für die wertvollen fachlichen Gespräche, die zahlreichen Hilfen im Umgang mit Linux und Rechenclustern, sowie für die gute Zusammenarbeit an Phoni.

Bianca Eifert, Marcel Giar und Christian Franz für die vielen nützlichen Tipps in Mathematica.

Saeideh Edalati-Boostan for the good team work.

Markus Heinemann und Robert Henrich für die zahlreichen Diskussionen und aufmunternden Worte, wenn es mal nicht so geklappt hat wie gewünscht.

Gert Homm für die Einblicke in die experimentelle Seite der Materie.

der gesamten AG Heiliger sowie den Mitgliedern des 1.Physikalischen Instituts für eine tolle Zeit.

allen Korrekturlesern.

meiner Familie für die Geduld und Unterstützung während meines Studiums und der Zeit der Promotion.

meiner Frau Xenia dafür, dass Sie in der gesamten Zeit zu mir stand und immer noch bei mir ist.

# Erklärung

Ich erkläre:

Ich habe die vorgelegte Dissertation selbständig und ohne unerlaubte fremde Hilfe und nur mit den Hilfen angefertigt, die ich in der Dissertation angegeben habe. Alle Textstellen, die wörtlich oder sinngemäß aus veröffentlichten Schriften entnommen sind, und alle Angaben, die auf mündlichen Auskünften beruhen, sind als solche kenntlich gemacht. Bei den von mir durchgeführten und in der Dissertation erwähnten Untersuchungen habe ich die Grundsätze guter wissenschaftlicher Praxis, wie sie in der Satzung der Justus-Liebig-Universität Gießen zur Sicherung guter wissenschaftlicher Praxis niedergelegt sind, eingehalten.

Michael Bachmann